University of Pretoria
Faculty of Engineering, Built Environment and Information Technology
Department of Mechanical and Aeronautical Engineering

A real-time hybrid method based on blade tip timing for diagnostics and prognostics of cracks in turbomachine rotor blades

Student:
B Ellis (14221404)

Supervisor:
Prof PH Heyns
Co-supervisor:
Dr DH Diamond

November 2019

Submitted in partial fulfilment of the requirements for the degree
Master of Mechanical Engineering

UNIVERSITEIT VAN PRETORIA
UNIVERSITY OF PRETORIA
YUNIBESITHI YA PRETORIA

Abstract

Title:	A real-time hybrid prognostics method for estimating remaining useful life of turbomachine rotor blades using blade tip timing
Author:	B. Ellis
Student Number:	14221404
Supervisor:	Prof P.S. Heyns
Co-supervisor:	Dr. D.H. Diamond

This dissertation proposes hybrid models for (i) diagnosis and (ii) remaining useful life estimation of a single fatigue crack in a low-pressure turbine blade. The proposed hybrid methods consist of physics-based methods and data-driven methods.

In this dissertation, blade tip timing is used to measure the relative tip displacement of a rotor blade. The natural frequency of the blade is determined by detecting the critical speeds of the blade using a newly derived least squares spectral analysis method. The method shares its origin from the Lomb-Scargle periodogram and can detect resonance frequencies in the blade's displacement while the rotor is in operation. A Campbell diagram is then used to convert the critical speed into a natural frequency. Two kinds of shaft transients are considered, a run-up run-down crossing the same critical speed, is used to test the new method. This dissertation shows that the relative displacement of the blade tip is comparable to those simulated from an analytical single degree of freedom model. It is also shown that the newly proposed resonance detection method estimates the natural frequency of the blade to a high degree of accuracy when compared to the measurements from a modal impact hammer test.

The natural frequency obtained from the real time measurement is then used in a pre-constructed hybrid diagnostics model. The diagnostics model provides a probability density function estimation of the surface crack length given the measured natural frequency. A Gaussian Process Regression model is trained on data collected during experiments and finite element simulations of a fatigue crack in the blade.

The final part of this dissertation is a sequential inference model for improving the estimation of the crack length and the prediction of the crack growth. The suggested model uses an unscented Kalman filter that improves estimations of the crack length and the rate of crack growth from Paris' Law coefficients. The model is updated each time a diagnosis is performed on the blade. The RUL of the blade is then determined from an integration of Paris's Law given the uncertainty estimates of the

current damage in the blade. The result of the algorithm is an estimation of the remaining number of cycles to failure. The algorithm is shown to improve the overall estimation of the RUL; however, it is suggested that future work looks at the convergence rate of the method.

Keywords: Blade Tip Timing; Diagnostics; Fatigue Crack Growth; Finite Element Method; Least Squares Spectral Analysis; Paris' Law; Probability Density Function; Prognostics; Sequential Inference; State Space Model; Unscented Kalman Filter

Acknowledgements

First and foremost, I would like to thank God Almighty for giving me the strength, knowledge and ability to complete this dissertation. Without his blessings, this work would not have been possible.

Secondly, I would like to acknowledge the contributions, assistance and guidance of the following people that helped to completing this dissertation:

- Prof PS Heyns as my academic supervisor for his guidance, encouragement and advice during the work. I would also like to thank him for the opportunity and resources to pursue post-graduate studies in the C-AIM department. His experience and wisdom are unmeasurable in the field of Vibration based Condition Monitoring and I am in great dept to having the opportunity to learn from such a world class professor.
- Dr DH Diamond for his prompt feedback, guidance and assistance with everything related to blade tip timing and the experimental setup.
- Ms B Mokoka (the heart of C-AIM) for her prompt assistance in any administrative related issues. Her friendliness and unrivalled management skills allowed me to get some sleep at night.
- Mr G Breitenbach for his welcoming assistance in the lab. His practical knowledge and experience helped in all aspects of the experimental setup. His enthusiasm and willingness to assist in difficult tasks during the project provided the motivation to complete the experiments on time.
- Mr H Booysen and Dr AJ Oberholster for their assistance in solving the challenges faced with the experimental equipment.
- Mr P Kruger for his prompt assistance in manufacturing all the components in the turbomachine. I would specifically like to thank him for manufacturing the rotor blades in time to perform the experiments.
- Mr G Jansen Van Vuuren for designing the airfoil shaped turbine blades used in the experiment.
- This project would have not been possible without the financial support of the Eskom Power Plant Engineering Institute (EPPEI)

Table of Contents

List of Abbreviations

AAS	Average Angular Speed
ANN	Artificial Neural Network
BTT	Blade Tip Timing
CBM	Condition-based Maintenance
CFD	Computational Fluid Dynamics
CI	Condition Indicator
CNN	Convolutional Neural Network
DAQ	Data acquisition
DFT	Discrete Fourier Transform
EDS	Electrodynamic Shaker
EO	Engine Order
EOL	End of Life
FEM	Finite Element Model
FRF	Frequency Response Function
GPR	Gaussian Process Regression
HI	Health Indicator
HS	Health State
IAS	Instantaneous Angular Speed
KF	Kalman Filter
LSSA	Least Squares Spectral Analysis
MDOF	Multi Degree of Freedom
MPR	Multiple Pulse Per Revolution
NDT	Non-Destructive Testing
OPR	One Pulse Per Revolution
PF	Particle Filter
PHM	Prognostics and Health Management
RUL	Remaining Useful Life
SDOF	Single Degree of Freedom
SMART	Separating, Morphing and Remeshing
STFT	Short Time Fourier Transform
TOA	Time of Arrival
UKF	Unscented Kalman Filter

List of Symbols

θ_b	Blade Tip Displacement	$[rad]$
Δ	Change in parameter	
$\boldsymbol{\Sigma}$	Covariance Matrix	
a	Crack Length / Crack Depth	$[mm]$
c	Crack Length / Damping Ratio	$[mm]$
$\mathbf{x_k}$	Current state vector	
$\mathcal{D}$	Data	
$\boldsymbol{\Phi}$	Design Matrix	
$\mathbb{E}[x]$	Expected value of x	
$\mathbf{X}, \mathbf{y}$	Features / Training Labels	
K_{1c}, K_1	Fracture Toughness / Stress Intensity Factor	$[MPa\sqrt{mm}]$
f	Frequency	$[Hz]$
$F(a)$	Geometric factor	
κ	Kernel function	
$P_{Lomb}(f)$	Lomb-Scargle periodogram	
$\boldsymbol{\mu}$	Mean Vector	
$\mathbf{g}$	Measurement function	
$\mathbf{z_k}$	Measurement vector	
$\mathcal{M}$	Model	
A_f, B_f, C_f	Model coefficients	
$\mathbf{w}$	Model parameters	
$\boldsymbol{\mathcal{N}}$	Multivariate normal Gaussian distribution	
σ, S	Nominal stress	$[MPa]$
N	Number of samples / Number of cycles	
C, m	Paris Law Coefficients	
$p(x)$	Probability of x	
$\theta_{b/s}$	Blade tip displacement relative to shaft	$[rad]$
θ_s	Shaft Displacement	$[rad]$
$\mathbf{f}$	State Transition Function	
t_n	Time of Arrival	$[s]$

1. Introduction

The use of Condition-based Maintenance (CBM) strategies are now well established. The field has encouraged engineers to treat damage in mechanical components only when they have been diagnosed close to failure. Its purpose is to reduce maintenance costs by repairing or replacing components that require it; contrary to replacing components that could remain in operation for much longer than initially estimated (Mishra, 2018). Vibration-based condition monitoring is used in CBM to identify vibration characteristics. These characteristics are then used to classify or quantify damage in mechanical components. This dissertation focuses on the use of vibration-based condition monitoring to predict failure in turbomachine blades while the blades are in operation.

One of the major interests in CBM is methods for predicting the Remaining Useful Life (RUL) of a component. RUL is the leftover time a component will remain within design specification limits given certain assumed future operating conditions. Naturally, knowing a component's RUL has implications for maintenance decisions and financial investment options. Predicting RUL of a component is challenging, because of (i) its dependence on operating conditions, (ii) accuracy of models for estimating damage in a component and (iii) accuracy of models for predicting damage from a condition monitoring signal, often obtained from accelerometers.

Interest in RUL has led to a new field in mechanical engineering, namely Prognostics and Health Management (PHM). The field attempts to incorporate the understanding of physics of mechanical systems and sensor data to predict when mechanical components are nearing failure. One of the reasons that PHM has not been implemented widely in industry is because of the accumulation of uncertainty when processing noisy sensor data. Furthermore, models that capture the physics of a degradation process are often too complex or numerically expensive to compute. Hence, latest developments in PHM resort to data-driven methods that quantifies failure from historical data (An, Kim and Choi, 2015). Although these data-driven methods provide an easy implementable solution, they often lack reliable estimates of the RUL when limited failure data is available. Thus, a major challenge in PHM is trying to build prediction models that require very little historical degradation data.

Recent work in PHM indicate the use of hybrid methods. These methods combine limited historical failure data and physics models to estimate the RUL of a component. Physics models are developed from understanding (i) how certain features (such as the natural frequency) relate to damage and (ii) the rate at which damage propagates in a component. Hybrid methods augment these physics based methods with data. Liao and Köttig (2014) propose various hybrid methods and identify possible combinations of data-driven and physics-based models. This dissertation primarily investigates a hybrid damage state estimation and hybrid damage state prediction approach.

1.1. Background

Turbomachinery blades experience harsh operating environments where it is difficult to find sensors that can provide appropriate condition monitoring data. This is due to (i) the cost of installing the sensor and (ii) the hash environmental conditions such as humidity, pressure and temperature that limit the lifetime of the sensors (Diamond, 2016). For this reason, nonintrusive methods have been developed for monitoring the vibration of turbomachinery blades. Blade Tip Timing (BTT) is a nonintrusive condition monitoring technique that uses proximity probes (Ye *et al.*, 2019, Diamond, 2016) and a shaft encoder to infer the blade tip displacement with respect to the shaft. Using this information, it is possible to detect vibration amplitudes and resonance frequencies of the blade. One of the most sought-after vibration quantities from BTT data is the natural frequencies of a blade.

Various methods have been proposed for identifying natural frequencies of rotor blades using BTT. These techniques show promise for identifying and tracking damage in turbines and compressors while the system is in operation. However, one of the largest problems with BTT is that every measurement occurs only after a blade has passed a proximity probe. Thus, the sampling frequency of a BTT system is dependent on the angular velocity of the rotor. Since the number of proximity probes encountered in field installations are usually limited to ten or below, the sampling rate of the BTT system is usually lower than some or all blade natural frequencies (Hu *et al.*, 2015). These factors cause traditional processing algorithms, such as the Fourier Transform, to have limited applicability.

1.2. Problem Overview

The general approach to predicting RUL from condition monitoring data starts by converting the time-based sequence of measurements into a feature space (Javed *et al.*, 2012; An, Kim and Choi, 2015). This feature space reduces the dimensionality of the signal. The features are then interpreted with a diagnostics model that identifies and quantifies the damage of the component. A damage propagation model is then applied to the current state and a future damage state is computed from this estimate. The End of Life (EOL) of the component is finally obtained when the future estimated damage state exceeds the failure criteria. RUL is simply interpreted as the time until the failure criteria is exceeded with a certain safety factor.

Liao and Köttig (2014) describe the implementation of prognostics using a similar flowchart as depicted in Figure 1.1. The figure shows each part of the information described above. The arrows represent different models that convert the input information state to the output state. This figure can further be subdivided into two key regions namely diagnostics and prognostics. The top part describes the diagnostics problem and has the objective of quantifying the damage state of the turbomachine blade. Whereas, the bottom row illustrates the prognostics problem and has the objective of propagating the damage by estimating future states until a failure criterion is reached. Both parts of the problem are crucial for estimating the RUL (Worden and Dulieu-Barton, 2004). Errors in the estimation of damage

during the diagnostics part causes errors in the final estimate of the RUL. Likewise, errors in the prognostics propagation model will either cause an early or late estimate of the EOL.

Moreover, each of the methods used in a prognostic algorithm follow from a detailed physics model. Yet, it is sometimes difficult to solve these physics models because of either computational cost and/or model complexity. Data-driven models, however, construct models that overlook some of the information in the flowchart. The only requirement being that enough data must be available. Li, Ding and Sun (2018) emphasise an important risk about estimating RUL. That is, the risk associated with late estimates of the EOL has severe consequences in terms of safety, whereas early estimates only impact cost. Therefore, decision making based on RUL estimates would be easier to perform if the RUL contains confidence intervals. If confidence intervals are available, the decision makers can dynamically adjust the level of risk they are willing to take.

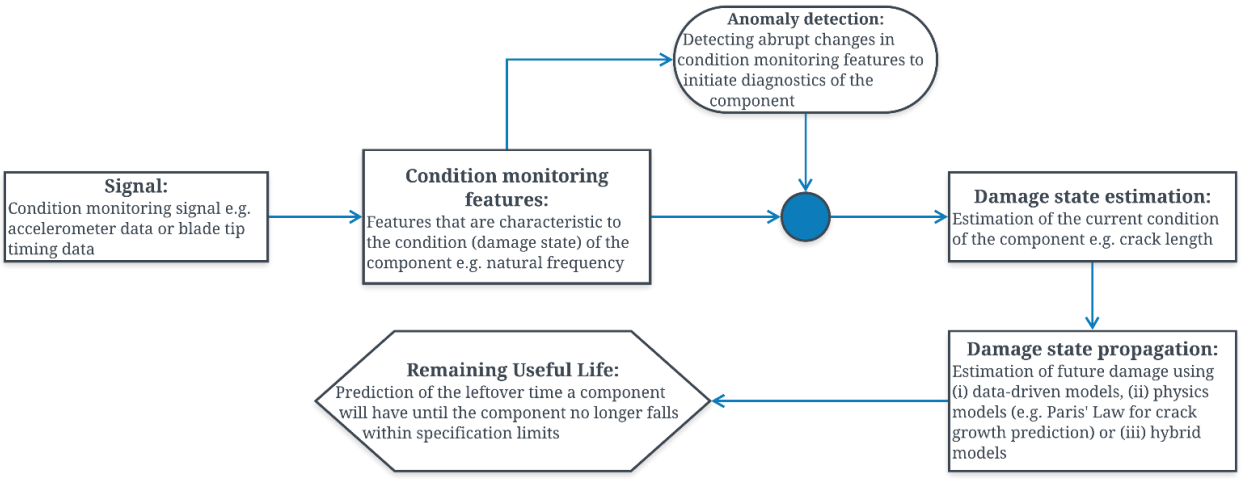

Figure 1.1: Information flowchart of the diagnostics and prognostics framework for obtaining the RUL from a noisy BTT signal

1.3. Objectives

The main objective of this dissertation is to estimate the RUL of a rotating blade given a BTT measurement signal. Therefore, this work is primarily a solution to the prognostics problem. However, as shown in Figure 1.1 prognosis is not a single problem but requires solutions to many smaller problems. This dissertation therefore proposes techniques and algorithms for the following three aspects of a complete real time prognostics approach for a turbomachinery blade. The proposed methodologies are tested and proven using experimental test results.

1. BTT as a condition monitoring method for identifying natural frequencies of rotating blades.
2. Diagnosis of a rotating turbomachinery blade's crack length from measured natural frequencies.
3. Prognosis of typical crack lengths in turbomachine blades using a physics based and data-driven hybrid method.

2. Literature study

Prognostics is the science of prediction and in the context of structural health management it is the estimation of the RUL of components or subsystems in mechanical systems (Saxena, 2010). These estimations/predictions are critical when preforming maintenance decisions. Prognostics follows a two-step process where a diagnosis of damage in a component or system is obtained from a condition monitoring signal and a prognosis is used to estimate the components' RUL (Liao and Köttig, 2014). Prognostics is ideally implemented in a real-time setting where estimates of the RUL are calculated while the condition monitoring data is collected from sensors.

However, many models used to diagnose and estimate future faults may not be constructed with real-time data. Instead, models are often trained with historical data and real-time estimates are made based on these pre-constructed models. These types of models may either be governed by physics or constructed from data. Hybrid or fusion prognostics models have the potential of incorporating both model types to quantify uncertainties in simplified physics models (Lei *et al.*, 2018). This literature study introduces the field of Prognostics and Health Management.

2.1. Overview of Prognostics and Health Management (PHM)

The definition of RUL is the estimated remaining time or number of fatigue cycles for which a component will remain within its specifications for assumed future operating loads and future environmental conditions (Saxena, 2010). The RUL prediction is based on an analysis of failure modes and the assessment of the existing damage in the component. The current damage is compared with a damage propagation model until the component exceeds its specifications (Orchard and Vachtsevanos, 2007). In turbomachines, one of the primary damage mechanism is high cycle fatigue crack propagation (Brits, 2016). Severe cyclic loads are exerted on the blades during operation. These loads are caused by the fluid's interaction with the blades. Fluctuations in the fluid pressure cause varying loads on the rotating blades (Forbes and Randall, 2013). This study seeks a simplified model that reduces the complexity of the physics (fluid interaction with the blade) in these systems, but also utilises vibration data to fine tune these simplified physics models.

Evidently, estimating RUL primarily depends on the framework one wishes to implement it in. This is referred to as the PHM framework. Saxena (2010) identifies two aims in prognostics namely (i) contingency management and (ii) maintenance management. Contingency management has the objective of increasing safety and decreasing collateral damage whereas maintenance management aims at decreasing costs and mitigating unnecessary servicing. Both methods provide different optimum decision criteria and have different views on the optimum RUL. Therefore, the term RUL is relative to the engineer's judgment and goals (Kai Goebel *et al.*, 2011). Subsequently, the end of life (EOL) of a component should be any researcher's first objective before seeking RUL. Since this allows users to

define a failure threshold (i.e. safety factor) of the prognostic horizon that satisfies their objectives. Consequently, run-to-failure data is necessary for any data driven prognostics model. This type of data is hard to come by due to the associated cost and risk when obtaining this data. Since, RUL is also dependent on the maintenance strategy it is important to derive a prognosis from the diagnosis of the component. This step is often neglected by most data-driven prognostics methods.

2.1.1. Prognostics and Health Management (PHM) framework

PHM should be the objective from the start of data acquisition to the end of life if one considers RUL for any maintenance decision. Consequently, one should use the appropriate sensors such that features of the sensor's data correlate strongly with the health state (i.e. damage) in the structure. Lei *et al.* (2018) and Saidi *et al.*, (2018) refer to these features as either health indicators (HIs) or condition indicators (CIs). The health state (HS) of the component is often observable such as the case of fatigue cracks being measured as part of non-destructive testing (NDT). The operation of the component or system is stopped for NDT purposes; thus, there is a limitation on the time intervals between measuring the cracks. Because of this, the damage in the system can rather be estimated from a continuous condition monitoring signal that allow structural health monitoring while the system or component is in operation. This is called a real-time diagnostics and prognostics framework (Chen *et al.*, 2018).

Vibration based condition monitoring is a field which considers detecting faults and tracking degradation in a component using vibration characteristics. Carden and Fanning (2004) identify three domains in which vibration characteristics are analysed namely (i) time domain, (ii) frequency-order domain and (iii) modal domain. Obtaining features from each of these domains require some knowledge about how the system behaves. This means one requires physics-based models such as a finite element model (FEM) that compares all the characteristics in each domain with the current health state. Otherwise, a data-driven model is required for comparing historical vibration characteristics with current observations to estimate the current health.

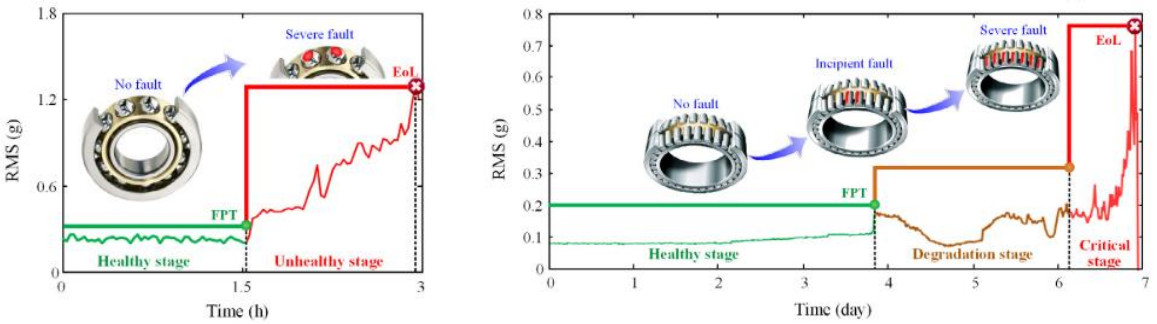

(a) (b)

Figure 2.1: Root mean square (RMS) health indicator over time a two stage (a) and three stage (b) degradation process depicted by Lei *et al.* (2018).

Time-based features may include statistical quantities such as the mean, standard deviation, kurtosis, skewness, rms and crest factor. These potential features might change as the structure degrades as depicted in Figure 2.1. The figure shows the change in RMS as the bearings begin to degrade. These time-based features assume that the condition monitoring signal originates from a stochastic process and can therefore completely be described by features of a probability density function. Nonetheless, prior signal processing of the time-based signal allows the extraction of frequency-based features that align better with physics models. These features also allow for analytical vibration models. The natural frequencies are related to the mass and stiffness of the component and should therefore be indicative of the health state of the structure (Carden and Fanning, 2004). On the other hand, modal domain analysis compares mode shapes to infer the location and extent of damage in the structure. This analysis is only conceivable for sensors that measure the shape of the structure. Corrado *et al.* (2018) showed that the mode shape allows one to detect multiple cracks and determine the location and size of these cracks by performing Gaussian process regression (GPR) on the collected data. Uhl (2004) found that three types of analyses are possible for detecting damage from mode shapes namely (i) modal vector correlation, (ii) modal curvature analysis and (iii) analysis of the deformation energy of the mode shapes. Other features may also originate from application of deep learning with artificial neural networks (ANN) using autoencoders and convolution neural networks (CNN) (Zhang *et al.*, 2018). However, assuming there is limited data for turbomachine blade failure these models may overfit[1] the data and fail to generalise the mapping between condition indicators and the vibration-based condition monitoring signal.

2.1.2. Physics-based, data driven and hybrid models

Carden and Fanning (2004) identified four stages of vibration-based condition monitoring namely (i) damage detection, (ii) damage location estimation, (iii) damage severity quantification and lastly (iv) RUL prediction. The last stage is the most important stage but relies on all other previous stages when using physics-based methods. That is, one cannot estimate the RUL accurately if the damage in the component is not estimated correctly. The models required for estimating damage and estimating RUL are discussed next.

Diagnostics models

First, a model is required for mapping the health indicators to an approximation of the health state of the component (Liao and Köttig, 2014). The model is called the diagnostics model (i.e. stage iii) and depends only on the features extracted from the condition monitoring signal. In this dissertation the natural frequency obtained from BTT data is considered as the health indicator. A lot of studies are dedicated to proving the relationship between natural frequency and damage for blades and cantilever

[1] Overfitting is a modelling error that occurs when overly complex models are selected to represent a limited number of data points. (Bishop, 2006; Will, 2019).

beams. Elshamy, Crosby and Elhadary (2018) showed, using the FEM simulations and experimental data, that the depth of a crack is correlated to a reduction in the natural frequency of a rectangular cantilever beam. These observations are also confirmed by FEM simulations of Khalkar (2018), Chaudhari and Patil (2016).

Roemer and Kacprzynski (2000) studied prognostics and diagnostics of gas turbine engines and mention the significant improvement hybrid diagnostics models have on the overall confidence levels of damage estimations. In their work they showcase the fusion of probabilistic models and pattern recognition models which are both data-driven methods. Despite hybrid methods having such a large potential impact on the confidence of diagnostics. Lei *et al.* (2018) stated that hybrid methods are some of the least published works in diagnostics and prognostics. The development of specialised equipment and flexible manufacturing causes mechanical systems to become more complex and unique. Consequently, less data becomes available for newly commissioned equipment and the components turn out to be too complex to construct all-entailing physics-based diagnostics models. Therefore, these circumstances require a model constructed from all available sources of information. Hence, hybrid methods are preferred until enough data is collected.

Du Toit, Diamond and Heyns (2019) proposed a hybrid diagnostics method that classifies the severity of a fatigue crack at the root of turbomachinery blades using BTT condition monitoring data. The diagnostics model is constructed from a hybrid of finite element models and data collected from experiments. The hybrid model is pre-constructed and can be used to classify the severity of a blade crack in real-time. This method provides a discrete severity classification instead of an estimation of the crack length in the blade. However, a continuous estimate of the size of the crack is required for prognostics. This is because prognosis is concerned with the rate at which damage propagates in a component. The location of the crack considered in their work was induced at leading edge of the blade.

Deterministic estimates are usually obtained from physics-based methods, whereas data-driven methods can provide confidence bounds for the diagnostics. In the latter case a probability distribution is often obtained as an estimation of the current damage in the component.

Prognostics models

Another model is required for approximating future health states based on fault degradation. This model is called the prognostics model and has the primary objective of estimating RUL (stage iv).

To estimate RUL of turbomachine blades from physics-based methods one requires an understanding of the failure mechanism that is being investigated. Modelling cracks in a blade requires knowledge of fatigue and fracture mechanics such that the model describes crack growth rate and when failure occurs in the blade. Other failure mechanisms such as creep and wear may also be present in the blade. Cubillo, Perinpanayagam and Esperon-Miguez (2016) mention that an understanding of the failure mechanism in a component is fundamental to any physics-based prognostics model. Modelling the exact

degradation may require computationally expensive methods such as a fatigue crack growth simulation using FEM. Reduced physics models generalise the failure mechanics to reduce computational cost. However, reduced models may generalise the failure mechanism too much such that correctly modelling the physics becomes problematic.

On the other hand, data-driven methods are only considered once enough data is collected, this is to prevent overfitting the model to the data. The most popular methods for predicting RUL from data are (i) GPR models and (ii) ANNs (Saha *et al.*, 2010; An, Kim and Choi, 2015). Li, Ding and Sun (2018) utilised deep CNNs to map the condition monitoring signal directly to remaining useful life without diagnosis of the damage in component. Models such as these require a large amount of run-to-failure data to predict RUL. The condition monitoring signal that Li, Ding and Sun use originates from run-to-failure simulations of 100 aircraft engines (Goebel and Saxena, 2008). A single failure in a turbomachine cost millions of dollars of damage and potential loss of human life. The associated cost of obtaining a single data point makes these types of data-driven methods extremely unfavourable.

Failure mechanics models are often described in terms of differential equations that relate the damage propagation rate to the current damage in the component (i.e. Paris' Law). Future damage is then determined from integrating these differential equations. It is required that the diagnostics model accurately determines the damage in the component to integrate the failure model correctly. Le, Chatelain and Bérenguer (2015) propose the use of sequential inference models in the form of a hidden Markov model (HMM) to improve the estimations of damage from the diagnostics. These improved estimates allow better estimation of future damage. The justification of this method is that in a real-time setting one obtains information about the damage in the component as the damage propagates. Thus, estimating/predicting damage with the failure mechanics modal and measuring the damage with the diagnostics model allows one to perform statistical inference on the "real" damage state of the component. Further details on the sequential inference model is provided later in this dissertation.

Liao and Köttig (2014) suggest many hybrid models that estimate degradation from an augmentation of reduced physics models with data. The framework that Liao and Köttig suggests is a state space model. Particularly, models that utilise the hidden Markov assumption. It is assumed that the current damage state is only dependent on the previous damage state. These types of models allow for some interesting analyses using Bayesian statistics to improve prior estimates of an unknown hidden ("real") damage state of the component (Candy, 2006).

2.2. Rotor dynamics: Behaviour of rotating structures

Rotor dynamics is the study of the behaviour of rotor blades, shafts, bearings and gears experiencing vibration (Meherwan, 2012). Consider a rotor blade, the blade has multiple natural frequencies and mode shapes that can be found using FEM or experimentally from a modal impact hammer test. Figure 2.2 shows the first three mode shapes for a simplified rotor blade simulated from FEM and Figure 2.3

plots the frequency response function of the same blade from a modal impact hammer test. The first mode shape ('flap mode') occurs at $203\ Hz$, the second mode ('twist mode') occurs at $1049\ Hz$ and the third mode occurs at $1236\ Hz$. The impact hammer test only shows the first resonance frequency.

The first mode shape is characteristic to most single degree of freedom (SDOF) models (Gubran, 2015; Mishra, 2016; Du Toit, Diamond and Heyns, 2019). The second mode shape, a torsional mode shape, has a nodal line over the length of blade. The blade tip rotates but does not have a significant displacement in the turbine's circumferential direction. This has a significant impact on detecting these frequencies with BTT techniques.

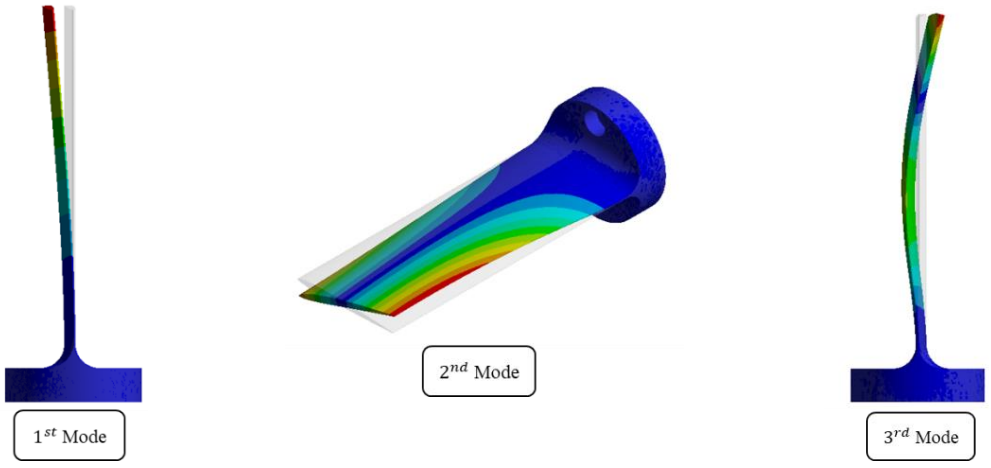

(a) (b) (c)

Figure 2.2: ANSYS simulated first three mode shapes of rotor blade with the 1st (a), 2nd (b) and 3rd (c) natural frequency mode shapes.

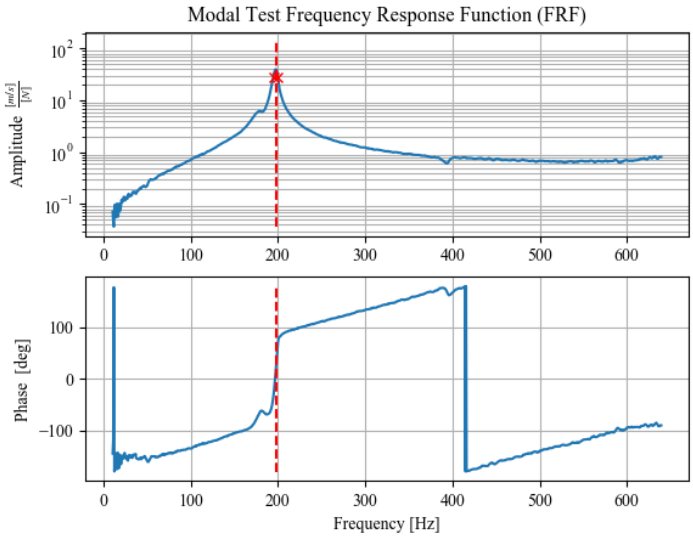

Figure 2.3: Frequency response function (FRF) of a rotor blade from a modal impact hammer test with amplitude and corresponding phase diagrams.

2.2.1. Centrifugal stiffening of turbomachine blades

Rotor blades experience centrifugal forces due to the angular velocity of the shaft. It is found that due to these centrifugal loads an artificial stiffening occurs in the blade and the natural frequencies of the blade increase. This increase in natural frequencies depends on the shaft speed of the rotor. Campbell diagrams plot the change in natural frequencies as a function of angular shaft speed. BTT attempts to find the natural frequency of a blade while the blade is rotating. This means the natural frequency measured from BTT is different than the frequency measured from a modal impact hammer test when the blade is stationary.

An example of a Campbell diagram is shown on the left side of Figure 2.4. In a preliminary investigation before determining the scope of this dissertation the effect of cracks on the overall Campbell diagram was investigated using FEM. This figure shows multiple Campbell lines (blue) to indicate how the "healthy Campbell line" changes as damage is introduced to the blade. This figure shows that the length of the surface crack does not change the shape of the Campbell diagram, instead the entire Campbell diagram is lowered due to the reduced stiffness of the blade. The cracks induced in the FEM simulations are equivalent to the cracks at the leading edge of the blade as investigated by Du Toit, Diamond and Heyns (2019).

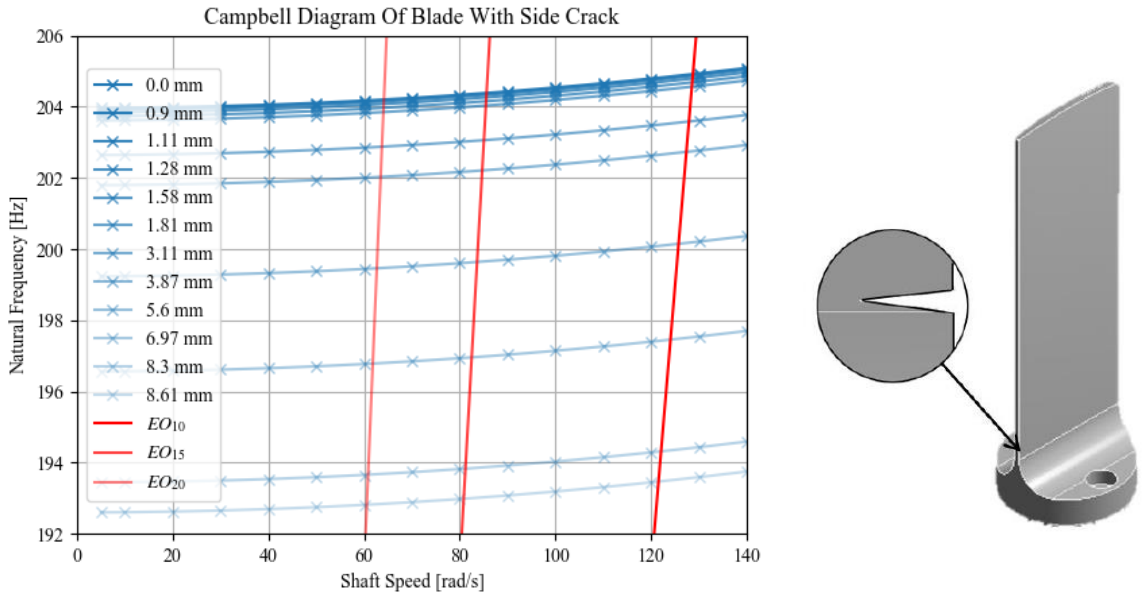

(a) (b)

Figure 2.4: Preliminary ANSYS simulation results for the changes in Campbell diagram (a) with increase in side crack length of a rotor blade (b).

2.2.2. Dynamic loads on rotating blades

Typical loading cases on rotor blades manifest in harmonics of shaft speed. These loads cause large deflections of the blade tip at certain speeds called critical speeds. Forbes and Randall (2013) identify two types of sources of loads that cause vibration in rotor blades namely (i) transmitted forces from

structural components such as bearings and imbalances in the shaft and (ii) unsteady pressure distributions due to the fluid exerting a force on the blade. The latter is considered in this dissertation. The red lines in Figure 2.4 are referred to as engine order (EO) lines and are commonly used in the design of turbomachinery blades (Meherwan, 2012). These lines show potential harmonic excitation frequencies of the shaft and where the blue and red lines meet, resonance will occur since the excitation frequency equals the natural frequency of the blade. The 10^{th}, 15^{th} and 20^{th} EO lines are shown in Figure 2.4.

The schematic in Figure 2.5 shows the wake interaction between stator and rotor rows of blades (Forbes and Randall, 2013). Observe that fluid changes momentum as the fluid moves from left to right and the middle row of blades moves vertically. This momentum change in the fluid has a loading effect on the blades. An equivalent net pressure difference is experienced by the blade that may either be harmonic (i.e. in phase with shaft angle) or non-harmonic. The frequency of the load that blade experiences is equal to the stator blade passing frequency. That is, the blade experiences a load pulse each time the rotor blade passes a stator blade. This load case is not the only loads a blade will experience. Gallego-Garrido *et al.* (2007) determined resonance of the blade tip at twice the shaft speed (2^{nd} engine order) even though 8 engine order blockers (8 stator blades) were used. This occurs because the interaction between the fluid and the blade is far more complex than a single harmonic excitation load at the stator blade passing frequency. A simplified load case is later simulated on a single degree of freedom system model that emulates behaviour of a blade during a run-up and run-down of the shaft. The simulated load case only considers the loads caused by a stream of air exerting a force on the blade. In the experiment, a single stream of air from a pressure source is tested.

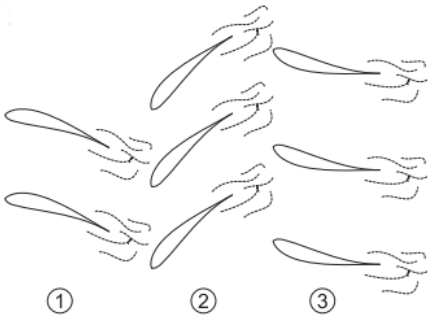

Figure 2.5: The wake interaction between rows of blades in a turbomachine depicted by Forbes and Randall (2013)

2.3. Blade Tip Timing: Measuring natural frequency

BTT is a real-time vibration monitoring method that measures relative displacement of the blade with respect to the shaft. The displacement is inferred from a measurement of the time of arrival (ToA) of each blade at the location of a proximity probe (Zhang *et al.*, 2017). Figure 2.6 depicts a typical BTT setup with a one pulse per revolution (OPR) sensor at the shaft. A multiple pulses per revolution (MPR)

tachometer provides a more detailed representation of the angular velocity than the OPR sensor. The shaft encoder is used to determine the blade's angular location each time a blade passes a proximity sensor. The displacement of the blade tip is then calculated from the difference between the measured angular location and an assumed "zero" angular location of the blade.

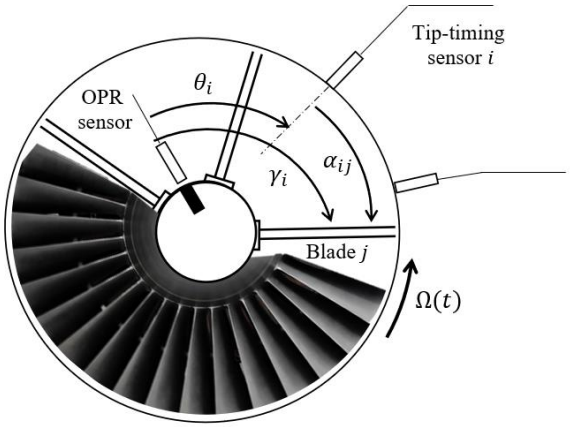

Figure 2.6: Typical BTT setup with rotating blades in a stationary hub adapted from Zhang, Duan and Jiang (2017). Tip-timing sensors are mounted to the hub to measure the time of arrival of the blades and the one pulse per revolution (OPR) sensor is placed near the shaft of the rotor.

2.3.1. Approaches

Equation (2.1) shows how the tip displacement (y) relates to the angular velocity and the position of the tip timing sensor. R denotes the radius from the centre of the shaft to the blade tip, $\Omega(t)$ is the rotational velocity as a function of time. Time of arrival (ToA) is denoted by t_{ij} and α_{ij} is the assumed static angular position of the blade.

$$y(t) = R\left(\int_0^{t_{ij}} \Omega(t)dt - \alpha_{ij}\right) \tag{2.1}$$

The tip deflection signal obtained from a BTT system is an event-based signal with a non-constant sampling frequency. Measurements of the tip displacement only occurs when the ToA is measured. This influences the type of signal processing one can perform on BTT data. For instance, a non-constant sampling frequency violates the assumptions behind most implementations of the Fourier transform and it is therefore not accurate to use this for a frequency analysis (VanderPlas, 2018). Also, adaptations to the standard Fourier transform such as the Non-Uniform Fourier Transform (NUFT) does also not provide accurate results due to the Nyquist frequency limit. This signal can also be resampled in terms of shaft revolutions to perform an analysis called computed order tracking. Computed order tracking identifies occurrences per revolution instead of per second. Yet, both methods have the problem of aliased signals due to the low number of samples per revolution or per second. The Nyquist frequency, which is equal to half the sampling frequency, is the largest frequency at which the Fourier transform will provide accurate results without aliasing. Subsequently, a low sampling frequency does

unfortunately not provide a complete picture of the frequency characteristics of the signal. Therefore, new signal processing methods that allow extraction of these features need to be considered.

2.3.2. Fourier transforms of non-uniformly sampled data

Consider the well-known discrete Fourier transform (DFT) of a signal denoted $G(f_k)$ in equation (2.2). The Fourier transform of equally sampled data allows one to analyse the frequency content of a signal. The inverse of the DFT is also provided in equation (2.3).

$$G(f_k) = \frac{1}{N}\sum_{n=0}^{N-1} g(t_n)e^{-2\pi k(n/N)i} \tag{2.2}$$

$$g(t_k) = \sum_{n=0}^{N-1} G(f_n)e^{2\pi k(n/N)i} \tag{2.3}$$

Since the invention of the DFT, most vibration-based condition monitoring efforts involve the transformation from time-based signals to frequency domain. One of the most limiting assumptions of this Fourier transform is that of constant sampling frequency and Nyquist frequency limits.

One of the methods to overcome these limitations is the Lomb-Scargle periodogram. A periodogram is simply the amplitude of the Fourier transform squared and is computed using equation (2.4).

$$P(f) = |G(f_k)|^2 = \left|\frac{1}{N}\sum_{n=0}^{N-1} g(t_n)e^{-2\pi k(n/N)i}\right|^2 \tag{2.4}$$

Kaloop and Hu (2015) demonstrated the use of the Lomb-Scargle periodogram in vibration-based condition monitoring for detecting damage in a stayed-cable bridge. The Lomb-Scargle algorithm maximises the likelihood of the provided data with respect to the model prescribed in equation (2.5). Thus, the algorithm solves the coefficients by maximising the probability of obtaining the data (denoted $\mathcal{D}$) given the prescribed model in equation (2.5) (denoted $\mathcal{M}$) and all its coefficients for any selected frequency (denoted f). This means the model parameters are determined from equation (2.6). If the data is assumed to be affected by white Gaussian noise distributed over the model, the solution to equation (2.6) collapses to the standard linear least squares regression problem (Bishop, 2006). The periodogram is simply computed by substituting the solution of equation (2.6) into equation (2.7).

$$g(t, f) = A_f \cos(2\pi f t) + B_f \sin(2\pi f t) + C_f \tag{2.5}$$

$$A_f, B_f, C_f = \underset{w.r.t\ A_f, B_f, C_f\ \forall\ \mathcal{D}}{\operatorname{argmax}} p(\mathcal{D}|\mathcal{M}, A_f, B_f, C_f, f) \tag{2.6}$$

$$P_{Lomb}(f) = \left|A_f^2 + B_f^2\right| \tag{2.7}$$

The Lomb-Scargle periodogram is finally determined using equations (2.8) and (2.9). Notice that the periodogram is a function of the frequency and all the data is simply substituted in the summations.

$$P_{Lomb}(f) = \frac{1}{2}\left\{\frac{(\sum_n g(t_n)\cos(2\pi f[t_n-\tau]))^2}{\sum_n \cos^2(2\pi f[t_n-\tau])} + \frac{(\sum_n g(t_n)\sin(2\pi f[t_n-\tau]))^2}{\sum_n sin^2(2\pi f[t_n-\tau])}\right\} \quad (2.8)$$

$$\tau = \frac{1}{4\pi f}\tan^{-1}\left(\frac{\sum_n \sin(4\pi f t_n)}{\sum_n \cos(4\pi f t_n)}\right) \quad (2.9)$$

The Lomb-Scargle periodogram is different from the Fourier transform, since the model in equation (2.5) is only a function of a single frequency. Therefore, this approach is a measure of interrogating the frequency content of the signal. VanderPlas (2018) indicates that the Lomb-Scargle periodogram has an elegant connection with probability density functions. That is, the relationship in equation (2.10). This shows that the probability of the frequency given that data ($\mathcal{D}$) and the model ($\mathcal{M}$) is directly proportional to the exponent of the Lomb-Scargle periodogram. Thus, the global maximum in the periodogram is the maximum likelihood estimate of the frequency.

$$p(f|\mathcal{D},\mathcal{M}) \propto \exp(P_{Lomb}(f)) \quad (2.10)$$

It is therefore tempting to believe that, in terms of BTT the peak of the periodogram is the natural frequency of the blade. This dissertation shows, however, that the model in equation (2.5) does not approximate the data from BTT well. The Lomb-Scargle periodogram is consequently changed to suit BTT data better and the resonating frequency is then found from the data.

2.4. Failure mechanisms: Damage state prediction

Understanding damage and the methods for modelling damage is fundamental to physics-based prognostics according to Cubillo, Perinpanayagam and Esperon-Miguez (2016). This discussion deals with some fundamental ideas of fracture mechanics. The focus is on why components fail in the presence of cracks. More so, the rate at which a small crack will grow in a component due to fatigue loading.

2.4.1. Failure types and models

Fracture mechanics attempts to model the reason for unexpected brittle failure in components. The components fail due to the presence of cracks. Sharp discontinuities in a component causes large stress amplification factors in the component. Sharp cracks have near infinite stresses at the crack tip. However, this does not mean that the component will fail due to these stresses. For certain loads, the material can sustain the presence of the crack. Failure due to cracks are determined from the stress intensity factor of the crack. The idea of the stress intensity factor was initially introduced by Griffith. Griffith derived that failure due to cracks in a structure occurs when it is energetically favourable for a crack to release its stored elastic potential energy due to an acting load exceeding the material's ability

to maintain the energy. Failure will occur when inequality in equation (2.11) is satisfied. Griffith originally derived these equations for an infinite plate with a through thickness crack in the centre of the plate. The value K_{1c} is a property of the material known as the fracture toughness. The stress applied to the plate and the crack length is denoted σ and a respectively. It is important to note that the stress in equation (2.11) is the nominal stress and is calculated for the component without any cracks.

$$a \geq \frac{1}{\pi}\left(\frac{K_{1c}}{\sigma}\right)^2 \tag{2.11}$$

Not all cracks are centre though cracks as Griffith derived and the geometry of the part is often more complex than a flat plate. Therefore, engineers have developed methods to account for the geometry by adding a geometric factor $F(a)$. $F(a)$ is a function of the geometry and the crack length (Hertzberg, Vinci and Hertzberg, 2012). The stress intensity factor K_1 is defined in equation (2.12). Failure occurs when the stress intensity factor is equal to the material fracture toughness.

$$K_1 = \sigma F(a)\sqrt{\pi a} \tag{2.12}$$

This dissertation looks at cracks in rotor blades. Due to the complex shape of these blades the geometric factor is often not available for the geometries of airfoils. The geometric factor can, however, be computed from the finite element method where the stress intensity factor is calculated at the crack front. These simulations require a fine mesh at the crack front to approximate the stress intensity factor well. Most researchers assume that the geometry of a blade is similar to a rectangular cantilever beam, with an applied bending moment, as shown in Figure 2.7. (Newman and Raju, 1981; Witek, 2015; Brits, 2016). This assumption allows for the use of the empirical formulas derived by Raju and Newman (1984). These empirical formulae are derived from finite element simulations of many rectangular cross-sectional beams. The Raju-Newman equations are provided in Appendix A of the dissertation.

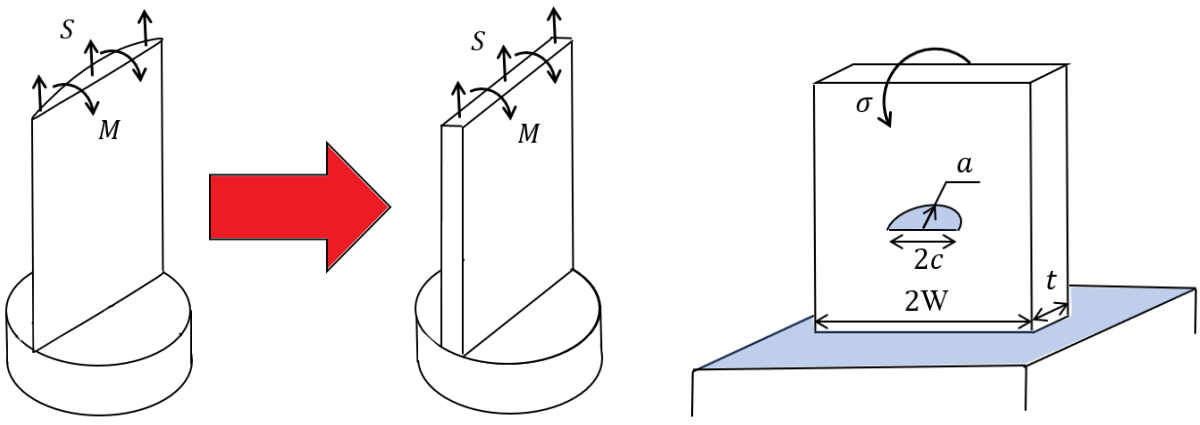

(a) (b)

Figure 2.7: Geometric assumption of a typical surface crack presented adapted from Brits (2016) (a) and the same geometric assumption adapted from Witek (2015) (b).

2.4.2. Crack growth rate

Fatigue is the study of remaining useful life of components under cyclic loadings. Fatigue design utilises SN curves for quantifying the number of cycles to failure for a certain stress amplitude in a material. However, these heuristic models do not account for the number of cycles that already occurred before the remaining useful life is estimated. This section summarises models for quantifying fatigue in terms of crack lengths.

Figure 2.8 shows the rate of crack growth as a function of the stress intensity range on a log-log graph. This graph is shown for a stress ratio equal to zero ($R = \sigma_{min}/\sigma_{max} = 0$). Notice that there are three stages in the lifetime of the crack. The first part is crack initiation, where the crack has started to form but is too small to detect, the second part is steady crack growth and the last stage is unstable crack growth. This dissertation is primarily interested in the second region when the crack experiences steady growth.

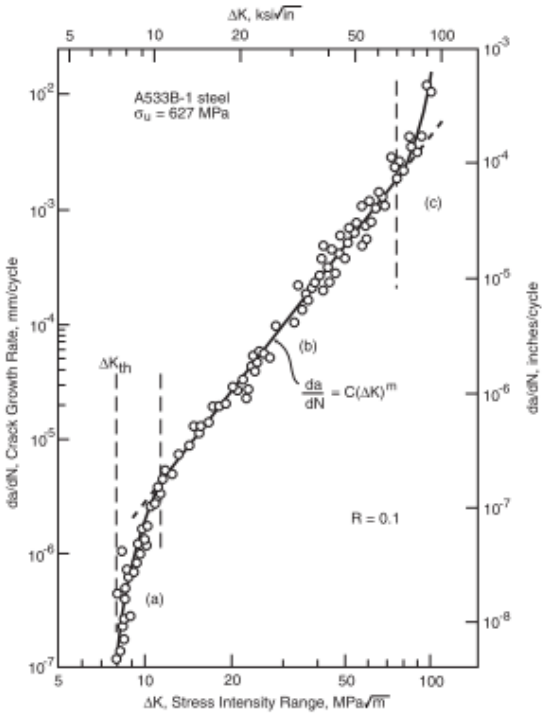

Figure 2.8: Crack growth rate as a function of range of stress intensity factor (Dowling, 2013)

Paris' Law describes the steady crack growth rate of a crack from the stress intensity factor range. Paris' Law is provided in equation (2.13) There are however limitations on the use of Paris' Law namely (i) it is only applicable for stress ratios equal to zero and (ii) it is only applicable after the crack has initiated and before the critical crack length is reached. The value of C and m are material parameters.

$$\frac{da}{dN} = C(\Delta K)^m = C\left(\Delta\sigma\, F(a)\sqrt{\pi a}\right)^m \tag{2.13}$$

Adaptations have been developed for Paris' Law that incorporates other stress ratios when $R \neq 0$. Three of the most popular models that are widely mentioned in literature are the Walker equation, the Foreman equation and the NASGRO equation (Dowling, 2013; Rege and Lemu, 2017). These equations are given in equations (2.14) to (2.16). The values C_0, C_1, C_2, m_0, m_1, m_2, γ, p and q are material parameters, ΔK_{th} is the minimum stress intensity factor range that will cause crack growth and K_{max} is the maximum stress intensity factor during the fatigue cycles.

$$\frac{da}{dN} = \frac{C_0}{(1-R)^{m_0(1-\gamma)}}(\Delta K)^{m_0} \tag{2.14}$$

$$\frac{da}{dN} = \frac{C_1}{(1-R)(K_c - K_{max})}(\Delta K)^{m_1} \tag{2.15}$$

$$\frac{da}{dN} = C_2\left[\frac{(1-f)}{(1-R)}\Delta K\right]^{m_2}\frac{\left(1-\frac{\Delta K_{th}}{\Delta K}\right)^p}{\left(1-\frac{K_{max}}{K_{1c}}\right)^q} \tag{2.16}$$

Notice that equations (2.14) to (2.16) all have a similar shape to equation (2.13). In fact, one could say that when assuming a constant stress intensity factor range the models in the above equations are all equivalent to equation (2.13) with modified Paris' Law coefficients. Coppe *et al.* (2010, 2012) proposed a prognostics method that considers modifying the Paris Law coefficients to better predict RUL. Wang *et al.* (2019) also implemented these changes in an extended Kalman filter to predict RUL.

2.4.3. Plasticity

The crack growth rate and the stress intensity factor are derived using linear elastic fracture mechanics (LEFM). This means that the material behaviour is assumed to be completely elastic. However, thin components such as a blade may experience loads that cause plastic deformation in the blade. In these cases, LEFM is no longer applicable and other fracture mechanics principles are necessary to determine failure in the blade. Adaptations to the standard LEFM models allow for a plastic zone correction that only increases the length of the crack with a value of a_{σ_0}. This correction allows the use of LEFM in situations where small scale plasticity is present. Equation (2.17) shows how the stress intensity factor is determined with the plastic zone correction.

$$K_1 = \sigma F(a + a_{\sigma_0})\sqrt{\pi(a+a_{\sigma_0})} \tag{2.17}$$

This dissertation will factor the effect of plasticity into the uncertainty of the crack length. Therefore, it is assumed that LEFM is applicable for all loads experienced by the blade. Future work should consider non-linear methods for determining the stress intensity factor and validate the use of LEFM to determine the stress intensity factor of a crack.

2.5. Predicting Remaining Useful Life (RUL)

After modelling the damage in the component using physics-based techniques the RUL of the component is determined from a damage propagation model. However, most deterministic estimates of the RUL do not capture the uncertainty in the RUL.

In an article, An, Kim and Choi (2015) describe the methods available for determining RUL of a component using physics-based methods and data-driven methods. In their work they found a common issue with the prediction of RUL for data driven methods. There is often uncertainty around whether enough data has been collected to accurately model the behaviour of the damage mechanism. In their physics-based approach the researchers mention the use a Particle Filter (PF) to improve estimates of the current damage in the blade.

Corbetta *et al.* (2017) also utilised a PF to model the multiple damage mechanisms of matrix cracks and delamination of composite laminates subject to fatigue loading. The failure mechanism of delamination behaves like a growing crack. In their method, the uncertainty in the damage is reduced by performing Bayesian inference on the measurement of (i) the matrix crack density, (ii) delamination and (ii) the normalised remaining stiffness of the component.

Wang *et al.* (2019) proposed the use of an extended Kalman Filter (EKF) for determining fatigue cracks in a component. Again, the EKF was only used to improve the estimation of the current crack length. The RUL is predicted from this improved damage estimate. This chapter will discuss the sequential inference methods such as PFs and EKFs to improve the prediction of RUL. (Candy, 2006)

2.5.1. Stochastic approach and the sequential inference problem

Before the RUL is estimated for a component, the uncertainty in the current damage in the component is reduced by performing Bayesian inference. In this approach, the damage is modelled as a probability density function. At each diagnostic stage evidence is gathered about the current damage in the component. However, the current damage can also be predicted from previous estimates of the damage since the rate at which the damage grows is known from the previous operating conditions and the failure mechanics models. Thus, these two sources of information are combined using Bayes' theorem[2].

Consider a hidden Markov chain model shown in Figure 2.9. The figure shows a hidden state vector $\mathbf{x}_k$ and all its previous states denoted $\mathbf{x}_{k-1}$ and $\mathbf{x}_{k-2}$. The state vector consists of the "true" damage in the component and evolves over time according to a state transition model (green). The "true" damage of the component is always hidden and at each time step a diagnostic estimation is performed to obtain the estimation of the current damage, denoted $\mathbf{z}_k$. These diagnostics measurements relate to the current

[2] Bayes' theorem determines the probability of an event based on prior conditions that are related to the event (Bishop, 2006).

damage state through the sensor model (purple). Initially, a prior probability[3] density function is assumed for the hidden state vector. Typically, a multivariate Gaussian distribution (denoted $\mathcal{N}$) with a prior mean vector, $\boldsymbol{\mu}_0$, and prior covariance matrix, $\boldsymbol{\Sigma}_0$, is defined. This is shown in equation (2.18). The transition function (**f**) and sensor function (**g**) are affected by Gaussian white noise and are influenced by the process and sensor noise covariance matrices denoted $\mathbf{R_w}$ and $\mathbf{R_v}$ respectively. Equations (7.19) and (7.20) are the Gaussian transition and sensor models respectively.

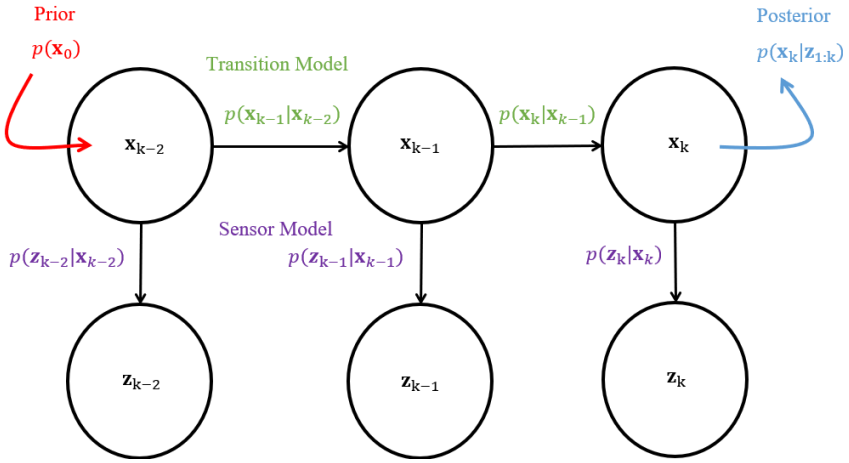

Figure 2.9: Hidden Markov chain model for sequential inference of the state vector **x.**

$$p(\mathbf{x}_0) = \mathcal{N}(\boldsymbol{\mu}_0, \boldsymbol{\Sigma}_0) \tag{2.18}$$

$$p(\mathbf{x}_k|\mathbf{x}_{k-1}) = \mathcal{N}(\mathbf{f}(\mathbf{x}_{k-1}), \mathbf{R}_w) \tag{2.19}$$

$$p(\mathbf{z}_k|\mathbf{x}_{k-1}) = \mathcal{N}(\mathbf{g}(\mathbf{x}_k), \mathbf{R}_v) \tag{2.20}$$

Bayesian sequential inference primarily consists of two steps namely (i) predict and (ii) update. During the prediction step the current damage ($\mathbf{x}_k$) is predicted from the previous estimation of the damage ($\mathbf{x}_{k-1}$). The update step incorporates the information gained when observing the damage in the component from the diagnostics model.

$$p(\mathbf{x}_k|\mathbf{z}_{1:k-1}) = \int p(\mathbf{x}_k|\mathbf{x}_{k-1})p(\mathbf{x}_{k-1})p(\mathbf{z}_{1:k-1})\, d\mathbf{x}_{k-1} \tag{2.21}$$

$$p(\mathbf{x}_k|\mathbf{z}_{1:k}) = \frac{p(\mathbf{z}_k|\mathbf{x}_k)p(\mathbf{x}_k|\mathbf{z}_{1:k-1})}{p(\mathbf{z}_k|\mathbf{z}_{1:k-1})} \tag{2.22}$$

[3] Prior probability is the probability of an event before making reference to certain observations or assumptions related to the event (Kenton, 2018).

Solving the integral in equation (2.18) and determining the updated probability distribution in equation (2.19) can sometimes be a non-trivial task. Especially when either the transition function or the measurement function is non-linear. The Kalman filter is a solution to equations (2.21) and (2.22) where the transition and sensor models are linear and the probability density functions in equations (2.18) to (2.20) are Gaussian distributed. Wang, Hu and Armstrong (2017) demonstrated the use of a Kalman filter for estimating cracks with a simplified Paris' Law equation. Saidi *et al.* (2018) extends the idea by implementing a Kalman smoother to improve these estimations. Each of these methods linearise Paris' Law by numerically integrating the crack growth rate using the forward Euler method to obtain the next crack length given the loading conditions and the previous crack length. These methods are only accurate for short transitions and are erroneous when many loading cycles occur between real-time diagnosis of the machine.

The analytical solution to equations (2.21) to (2.22) are very difficult for systems with nonlinear transition and sensor models. In prognostics, this transition model is the damage propagation model which is almost always nonlinear. Therefore, the most popular methods used by researchers are Monte Carlo methods also known as particle filter methods (An, Kim and Choi, 2015). Many researchers use particle filters for their prognostics models (Sbarufatti *et al.*, 2002; Baraldi, Mangili and Zio, 2012; Baraldi *et al.*, 2013; Jouin *et al.*, 2016; Corbetta *et al.*, 2018). The particle filter estimates the probability distributions with samples from the distribution. Inference is then performed on each individual sample of $\mathbf{x}$ and samples collectively represent the posterior probability[4] distribution. A single note about PFs is that they can become computationally expensive when the state vector ($\mathbf{x}$) has many dimensions and the method is only accurate for numerous samples.

Julier and Jeffrey (1997) proposed a different approximation method for determining the posterior distribution in equation (2.22) called the unscented Kalman filter (UKF). The UKF attempts to approximate the Kalman Filter for non-linear transition functions by substituting the probability density functions with what is called the sigma points of the distribution. These sigma points represent the mean and covariance of the original Gaussian probability density function. After each predict and update step the sigma points are passed through the transition and measurement functions to obtain and approximate the posterior probability density function. Figure 2.10 shows a one-dimensional case where the prior probability distribution is shown in blue. This probability distribution is passed through a non-linear function to obtain the posterior distribution shown in red on the y-axis. The UKF approximates the posterior distribution (red) with a Gaussian distribution (green) using the sigma points shown by the dotted lines. Figure 2.11 shows a two-dimension case and how the sigma points transition during a nonlinear transformation. The result from the UKF is always a Gaussian distribution. Anger, Schrader

[4] Posterior probability is the updated probability after taking new information, observations or assumptions into account (Hayes, 2019).

and Klingauf (2012) used a UKF to improve RUL prediction accuracy of bearings experiencing surface pitting during operation. This dissertation uses a UKF to improve the estimation of the crack length. The proposed model also updates the coefficients of Paris' Law to improve the estimations of future crack lengths. An analytical integration of Paris' Law is proposed instead of a forward Euler method to increase the accuracy of the predict and update step in equation (2.21) and (2.22).

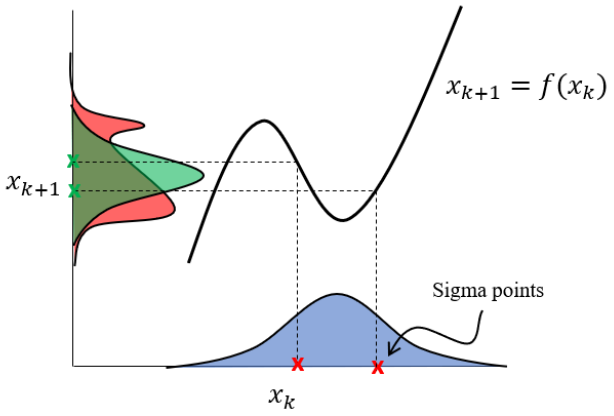

Figure 2.10: A one-dimensional illustration of passing the probability distribution of the state x_k through a non-linear transition function to obtain x_{k+1}. The distribution in red is the resulting non-Gaussian distribution and the distribution in green is the Gaussian approximation that the UKF solves.

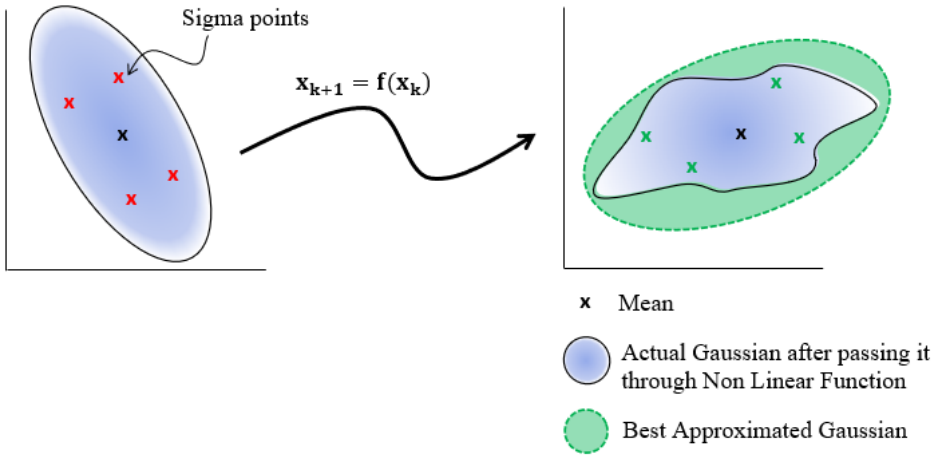

Figure 2.11: 2D-Multivariate Gaussian approximation after the transition of a non-linear function and the use of sigma points to show the new distribution after a non-linear transformation (adapted from Julier and Jeffrey, 1997 and Singh, 2018).

3. Research methodology

Relevant factors that affect the prognostics of turbomachine blades have been considered in the literature study. This section summarises the scope and contributions that this dissertation offers in the field of RUL prediction and diagnostics of turbomachine blades. It is understood that diagnostics form an important part in RUL prediction. Uncertainty management from noisy condition monitoring data also affects the final RUL result. Therefore, the scope of this dissertation is an all-inclusive prognostics-diagnostics methodology and an experimental validation there-of.

3.1. Research question

This dissertation provides solutions to the following three problems found in the literature. These areas form the basis for a complete real time prognostics methodology to be implemented on a general turbomachine.

3.1.1. Determine the natural frequency of a rotor blade during a transient operation

Many researchers provide methods for characterising the vibration of turbomachine blades using BTT data (Gallego-Garrido *et al.*, 2007; Diamond, 2016; Mohamed, Bonello and Russhard, 2019). A novel method is proposed for identifying the natural frequency of a turbine blade from multiple proximity probes measurements. This method utilises a least squares spectral analysis (LSSA) method and finds its origin in the Lomb-Scargle periodogram (VanderPlas, 2018). The method attempts to approximate a Fourier Transform on data that is unequally sampled in time. The blade resonating speed is determined from this method and the natural frequency is calculated. However, modifications to the standard Lomb Scargle method are required to suit the data from multiple proximity probes. The method is only validated for transient shaft speeds, specifically a run-up and run-down.

3.1.2. Estimate fatigue crack length from natural frequency

A lot of vibration-based condition monitoring efforts are focused towards estimating damage from vibration characteristics (Mishra, 2016). This dissertation suggests a hybrid method for estimating crack sizes from both physics-based models and data driven models. The method utilises a Bayesian approach to construct the hybrid models. The Bayesian approach provides uncertainty estimates of the damage in the rotor blade given all prior data collected. The method is a Gaussian Process Regression (GPR) model that constructs a relationship between the natural frequency and crack length by modelling the points as samples from a multivariate Gaussian distribution. Finite Element Models (FEM) augment the data collected from experimentally damaged blades to improve the model performance. The method, as derived and tested in this dissertation, is restricted to cracks that initiate at the maximum bending stress location when the blade tip is displaced in the tangential direction. This dissertation therefore assumes the location of the crack and the size of the crack is determined through both experimental

results and FEM fracture simulations. Extensions to other crack locations can be performed in future research and will follow the same process.

3.1.3. Predict future crack lengths and estimate RUL

The final part of this dissertation utilises the estimations of the crack length to predict the number of fatigue cycles until failure of the blade. It is assumed that the stress range of the blade during operation is known and future stress ranges are approximated from the normal operating conditions. In the standard physics-based approach, the number of fatigue cycles to failure is determined from integrating Paris' Law. However, the method is deterministic and only provides a single estimation of the RUL. In recent works, a Bayesian inference method is proposed for improving the estimate of the current crack length (Wang *et al.*, 2019).

The method proposed here is different from the deterministic approach and the Bayesian standard inference approach and considers performing inference on both (i) the current crack length and (ii) the degradation mechanics model (i.e. Paris' Law) to improve the estimation of future crack lengths. Coppe *et al.* (2010, 2012) first suggested adjusting Paris' Law coefficients to estimate RUL. However, the suggested method uses a Markov-Chain-Monte-Carlo (MCMC) model and is computationally expensive to evaluate. Coppe *et al.* also disregard the geometric factor and factors its uncertainty into the uncertainty of the Paris' Law coeficients. This dissertation improves the suggested model with an unscented Kalman filter (UKF) to improve the computational efficiency of method. This method also includes the previously neglected geometric factor to reduce the uncertainty of Paris' Law.

3.2. Experimental proposal

Experimental tests are conducted and used to evaluate the proposed algorithms derived in this work. Consider the following experimental proposal and the experimental setup.

3.2.1. Methodology

A flowchart is presented in Figure 3.1 to assist in explaining the experimental methodology used to test the proposed methods. Initially, the blades' first natural frequency is measured from a frequency response function (FRF) obtained by performing a modal impact hammer test on the blade. This test is conducted while the blade is stationary and attached to the shaft of the rotor. The first peak in the FRF is taken as the natural frequency of the blade. This measurement is seen as the "true" natural frequency of the blade at rest. Next, the blade is rigidly attached to the surface of a slip table that is actuated at the natural frequency of the blade to initiate a crack in the blade. After damage is induced in the blade, the surface crack length is measured using a non-destructive testing (NDT) liquid dye penetrant to highlight cracks in the blade. The blade is then remounted to the rotor and the new natural frequency is recorded from an impact modal hammer test.

BTT data is used to perform the diagnosis of the blades' crack length. To do this, the blade is subjected to loads from a transient run-up and run-down of the rotor after every crack increment. The run-up and run-down excites the first natural frequency of the blade. The recorded tip deflections are then used to measure the blades' first natural frequency while the blade is spinning. This measurement is compared to the measurement from the modal impact hammer test by accounting for the stiffening of the blade during rotation. The process is repeated and the crack in the blade is further grown by, again, resonating the blade on the slip table. The new crack length is measured. Thereafter, the procedure is repeated until the crack length is close to the critical crack length. Safety restrictions are placed on the relative change in natural frequency between crack growth increments.

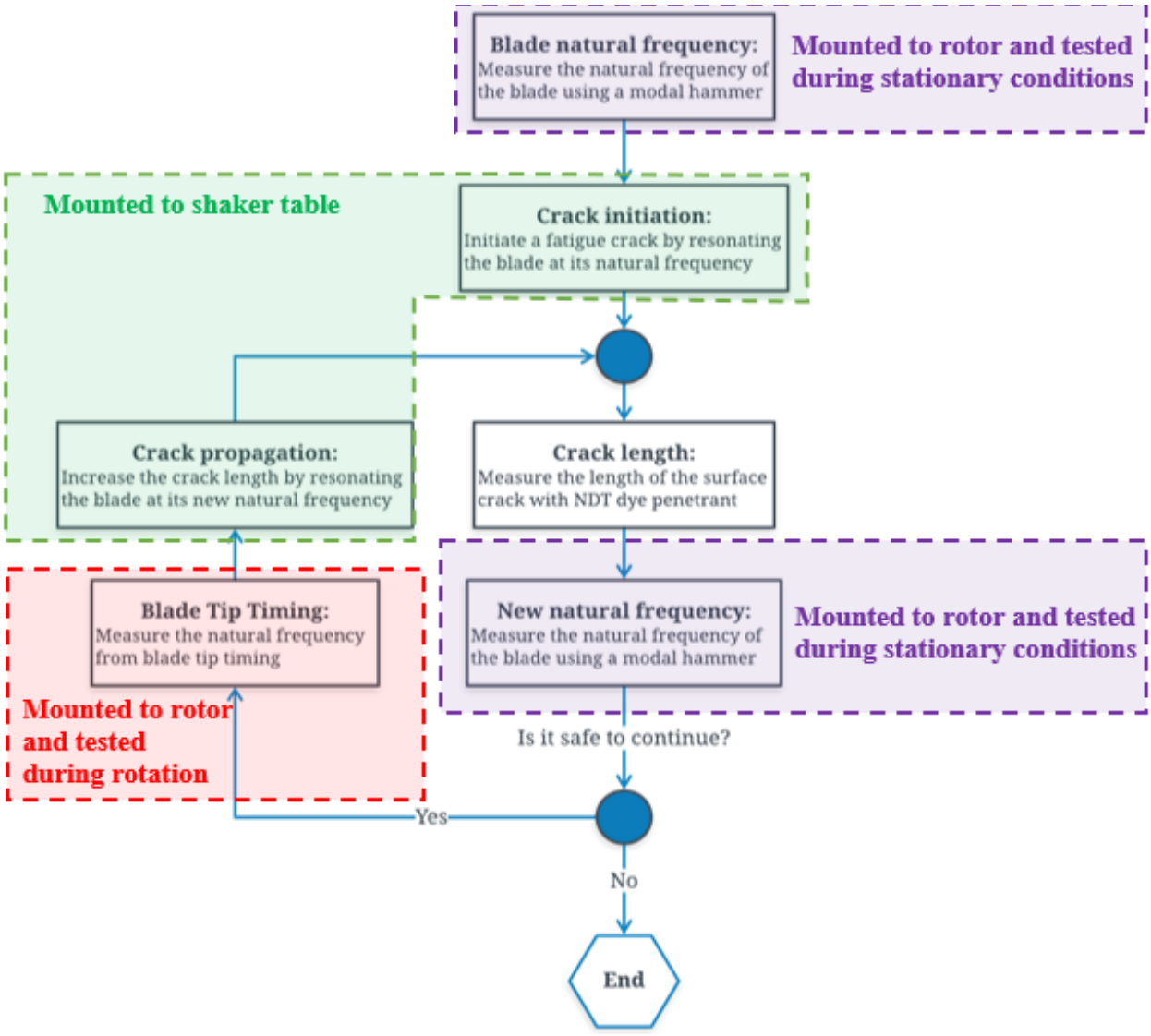

Figure 3.1: Experimental procedure flowchart that explains the experiments used to test the proposed method.

The idea of this experiment is to predict the RUL of a rotor blade using only BTT data. To do this, the natural frequency and crack length of the blade needs to be measured intermediately after periods of

fatigue-based damage have been induced. Also, since the cracked blade rotates at large angular velocities, careful consideration is required for maintaining safety, since this blade is prone to brittle failure. Table 3.1 summarises the measured parameters and the apparatus mentioned in this experiment.

Table 3.1: Measurement parameters and the associated apparatus used during experimental work.

Parameters	Apparatus
Crack Length	Liquid dye penetrant
Stationary Mounted Natural Frequency	Modal hammer impact hammer and laser vibrometer
Rotating Natural Frequency	BTT
Number of Cycles	Electrodynamic shaker and laser vibrometer

3.2.2. Blade geometry and material properties

The rotor blade considered in the experimental work attempts to emulate the geometry of blades typically found in turbomachinery. The geometry shown in Figure 3.2 is a $40\ mm$ cord NACA 4506 airfoil designed by Jansen van Vuuren (2019). The blade is designed to mimic the loads non-symmetric airfoils experience due to the fluid exerting a load on the blade. However, for this experiment the loads induced on the blade will only originate from a single high velocity stream of air. The blade is mounted to the rotor with two bolts and can be positioned at different angles in the rotor setup. This experiment will only look at $22.5°$ orientation of the blade with respect to the axial direction. The length of the blade is approximately $116\ mm$ and it is made of Aluminium T6-6082. The material properties of the blade are given in Table 3.2.

Table 3.2: Material properties of Aluminium T6-6082 recorded in literature (Mrowka-Nowotnik, Sieniawski and Nowotnik, 2006; Correia *et al.*, 2016; Du Toit, Diamond and Heyns, 2019)

Material Property	Value	Unit
Density	$2700 - 2810$	kg/m^3
Elastic Modulus	$67 - 71$	GPa
Poisson Ratio	0.33	%
Fracture Toughness	$33 - 41$	$MPa\sqrt{m}$
0.2% Proof Stress	$255 - 390$	MPa
Paris Law Exponent	2.7845	-
Paris Law Coefficient	1.1551×10^{-11}	$(mm/cycle)/\left(MPa\sqrt{mm}\right)^m$

As far as BTT research goes, not many researchers use airfoil shapes in their experimental work. Commonly, rectangular cross-sectional blades are used to test BTT algorithms (Hu *et al.*, 2015; Rigosi, 2015; Du Toit, Diamond and Heyns, 2019; Ye *et al.*, 2019). Since the blade geometry is custom-built,

limited failure data is readily available to construct diagnostics and prognostics models from. This work is unique in the sense that BTT and fatigue failure tests are performed on the complex airfoil shape. In real turbine blades, the shape of the airfoil could contain a twist along the length of the blade as well, however this dissertation will not consider such a twist.

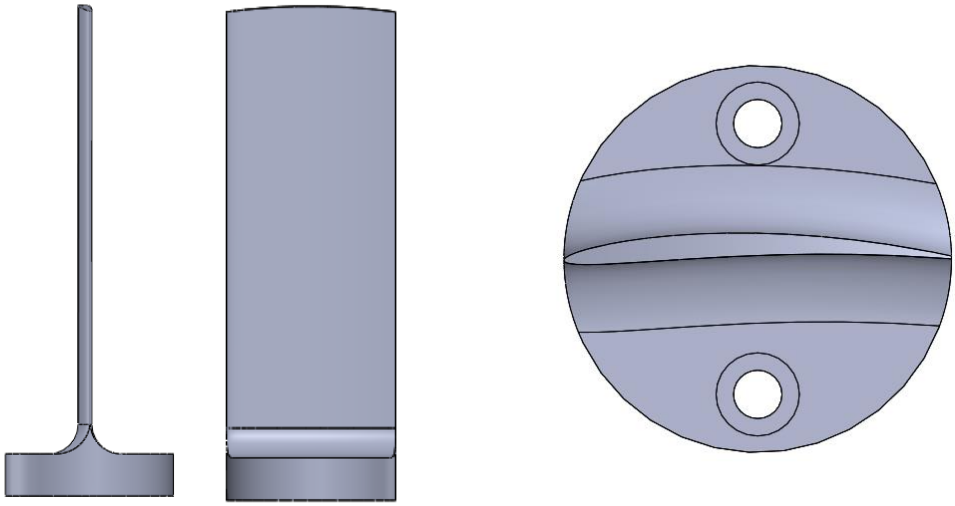

Figure 3.2: Geometry of the 40 mm cord NACA 4506 Airfoil with side views (left) and top view (right)

3.2.3. Experimental setup and procedure

The experimental setup has four main components namely (i) BTT, (ii) fatigue crack growth with an electrodynamic shaker (EDS), (iii) modal impact hammer test and (vi) NDT liquid dye penetrant crack measurement. Each component in the experimental setup is detailed here.

Blade Tip Timing

The rotor test bench is illustrated in Figure 3.3. The three-phase motor is controlled by a 10 V voltage source and can rotate at a maximum angular velocity of 1400 RPM.

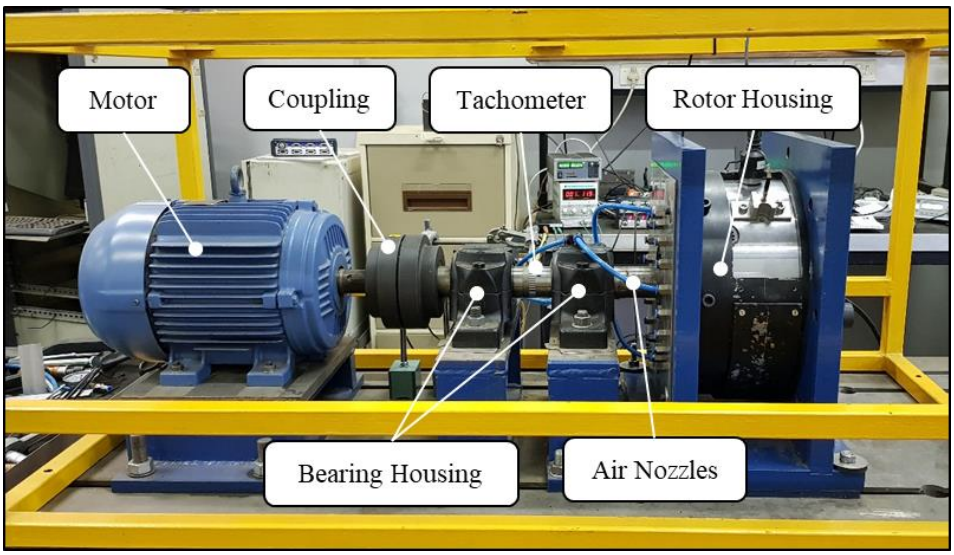

Figure 3.3: Side view of total BTT test bench.

Figure 3.4 shows the inside of the rotor housing with only a single blade mounted to the rotor. The other rotor blades and all the stator blades are removed from the setup. The reason for this change is to ensure safety, since the blade has a crack and could fail while the rotor is spinning. Counterweights are added to ensure that the rotor is balanced due to the removal of the other rotor blades. A single air nozzle is also extended and connected to a 3 bar pressure source to excite the blade during rotation. A single stream of air impacts the blade per blade rotation. The stream of air is by no means equivalent to the natural flow from the stator blades. Instead, this experiment attempts to measure the response of the blade using BTT and finds the first natural frequency from the measured response. Future work shall consider the effect of multiple air nozzles and stator blades on the response of the blade to imitate the loads in real turbomachinery. The blade is angled at 22.5° with respect to the axial direction to impose the momentum change of the fluid as the shaft spins, thus causing the fluid to exert a force onto the blades.

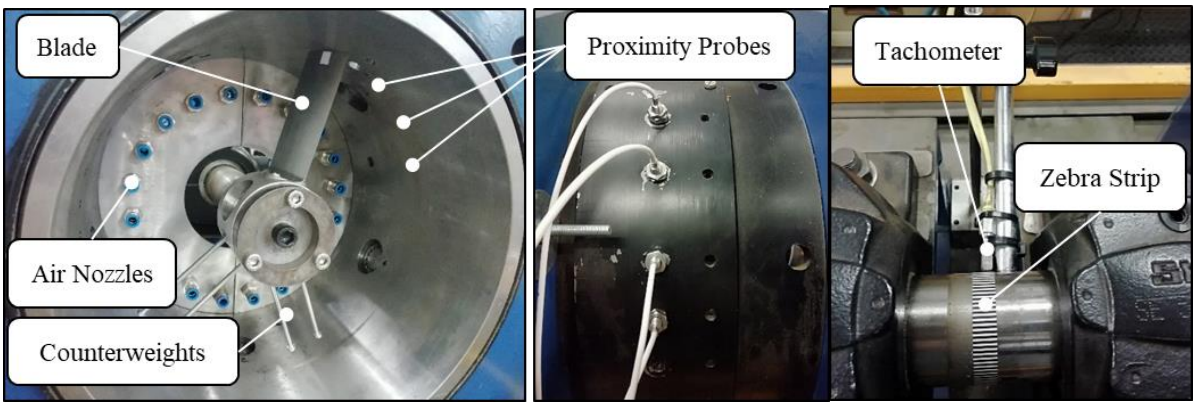

Figure 3.4: Single blade in rotor housing with counterweights (left), proximity probes fastened onto the outside of the rotor housing (middle) and the optical shaft encoder with zebra strip wrapped around the shaft (right).

The optical shaft encoder and the eddy current proximity probes are shown in Figure 3.4 (middle and right respectively). The shaft encoder measures angular velocity of the shaft from voltage pulses as the zebra strip rotates. A total of 79 pulses are generated per single shaft revolution. A gap distance of approximately 0.5 mm is left between the encoder and the shaft.

The eddy current proximity probes detect when the blades pass the probes. These probes generate a voltage when a conductive material enters the sensors' measuring region. Three eddy current proximity probes are installed on the outer rotor housing with a clearance gap of 0.2 mm between the probe head and the blade. The time of arrival (ToA) is measured from the voltage pulse generated by the proximity probe using the rising edge of 30% total voltage range as a trigger criterion. The probes are connected to an external 24 V battery source to minimise the electrical noise present in the laboratory.

A data acquisition (DAQ) device, an HBM Quantum MX410, synchronously records both the shaft encoder and proximity probes' voltages at a sampling rate of 192 kHz. In this work data is processed off-line after the experiments have been conducted. In a real-time diagnostic setting the ToAs will be determined instantaneously instead of the entire voltage signal being stored.

This experiment considers a linear 50 seconds run-up and 50 seconds run-down of the shaft with a maximum shaft speed of 1400 RPM and an amplitude of 100 RPM. A triangular voltage signal at a frequency of 0.01 Hz with variable amplitude and offset is used to control the motor.

Crack growth using electrodynamic shaker

The crack in the blade is initiated and propagated with an electrodynamic shaker (EDS). Figure 3.5 shows part of the EDS (left) that vibrates the slip table (right). The vibration is tuned such that the table vibrates at the first natural frequency of the blade. The amplitude of the slip table's vibration is between $5g$ and $2g$ and depends on the blade tip response measured from a laser vibrometer. The amplitude of the slip table's vibration is controlled such that the voltage output of the laser vibrometer does not overload the control of the slip table. The maximum displacement of the blade tip during this experiment is less than 5 mm. The blade in Figure 3.5 is mounted rigidly to the table though a mounting plate that is fastened with 7 bolts. This is to ensure a rigid connection between the table and the blade.

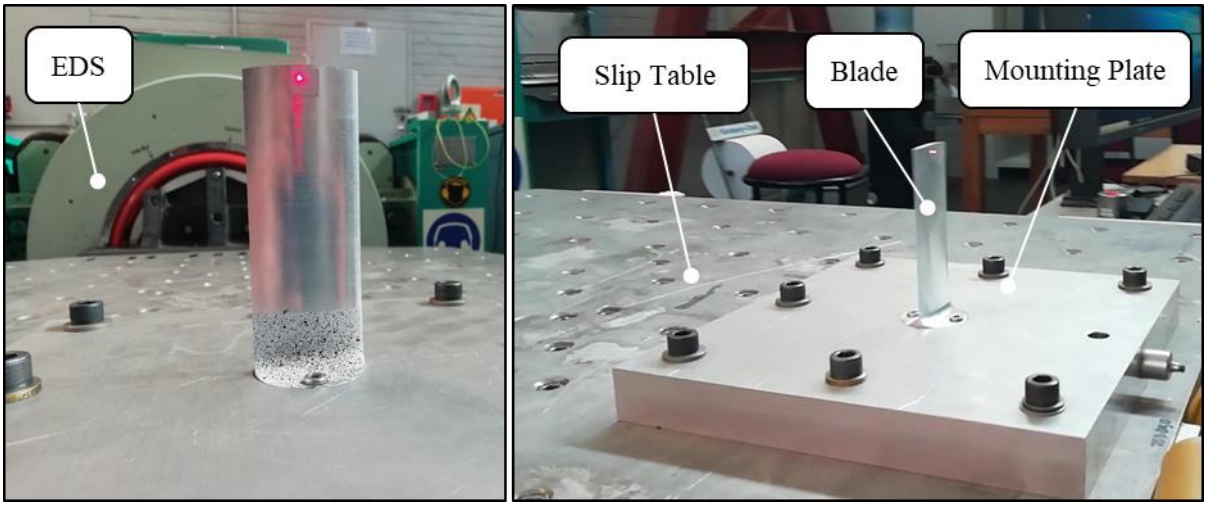

Figure 3.5: Electrodynamic shaker (EDS) oriented to shake the slip table (left) with a blade mounted to the table (right).

Observe the red laser light at the blade tip in Figure 3.5 (left). This is the location where a PSV 400 laser vibrometer measures the blade tip vibration. The EDS is controlled with a closed loop feedback system. The system measures the acceleration of the slip table and the velocity of the blade tip; and an FRF is then constructed from both signals. The EDS is set to maintain the FRF at the first resonance frequency. The run-up procedure therefore sweeps through a range of frequencies to construct a rough FRF. Thereafter, the EDS excites the blade at the first resonant frequency, while performing small

oscillations in frequency to detect changes in the FRF. Changes in the natural frequency will cause the EDS to search for the new resonant frequency. The test is concluded when the resonant frequency changes more than 5 Hz. The control system brings the table to rest when the test is concluded.

Modal Analysis

After a crack is generated in the blade, the new first natural frequency needs to be measured in order to compare it to the BTT-derived value. An impact hammer modal test is conducted on the blade after each crack growth increment. The blade is rigidly attached to the rotor for these tests, as shown in Figure 3.4. A PDV 100 laser vibrometer is set up to measure the velocity response at the tip of the blade. The blade is then impacted by a modal hammer and the FRF curve is recorded for the blade. The average FRF curve is constructed from 3 impact hammer tests.

NDT Liquid Dye Penetrant

The crack length in the blade is measured by preforming an NDT liquid dye penetrant test. The blade is first thoroughly cleaned with penetrant remover. Thereafter, the blade is sprayed with liquid dye penetrant (Figure 3.6 left) and left for 20 minutes so that the penetrant reaches deep into the cracks. Next, the blade is cleaned, and all the penetrant is removed from the surface with a towel sprayed with penetrant remover. Finally, a thin layer of developer is sprayed on top of the surface and the result is shown in Figure 3.6 (right). The crack length is then measured using a Vernier Calliper.

Figure 3.6: Blade sprayed with red liquid dye penetrant (left) and a developed NDT result for measuring crack length (right)

3.2.4. Limitations and exclusions

The scope of research only includes a methodology for predicting RUL for a single crack at the root of the NACA 4506 blade. Other blade geometries and crack locations are not considered here. Also, due

to safety concerns only a single blade in the rotor is tested and the interaction between blades are not modelled nor included in this scope. The effect of orientation angle in the rotor hub is also excluded, however preliminary studies have shown that the angle of attack of the rotor blade has a large impact on the amplitude of blade tip response. The loading on the blade mainly originates from the momentum change of the high velocity streams of air. The effect of different pressure changes across the blade is therefore not part of in this study. These limitations are potential topics for future research.

3.2.5. Experiments summary

Figure 3.7 is a summarised procedure for the experiments conducted in this dissertation. The figure shows the experiment cycle that starts with a blade mounted to the rotor (shown in greed) the blade's natural frequency is measured using BTT and confirmed using a modal impact hammer test. Next, the same blade is mounted to the EDS and the crack in the blade is initiate/ grow the crack in the blade. A single experiment is conducted in this dissertation. However, two outcomes are obtained from the single experiment namely (i) the natural frequency estimated from BTT is validated to the measurements of a modal impact hammer test and (ii) the fatigue lifecycle of the blade is used to validate the RUL prediction methodology. The cycle in Figure 3.7 is repeated for 10 blades until each blade is considered unsafe to perform the BTT test.

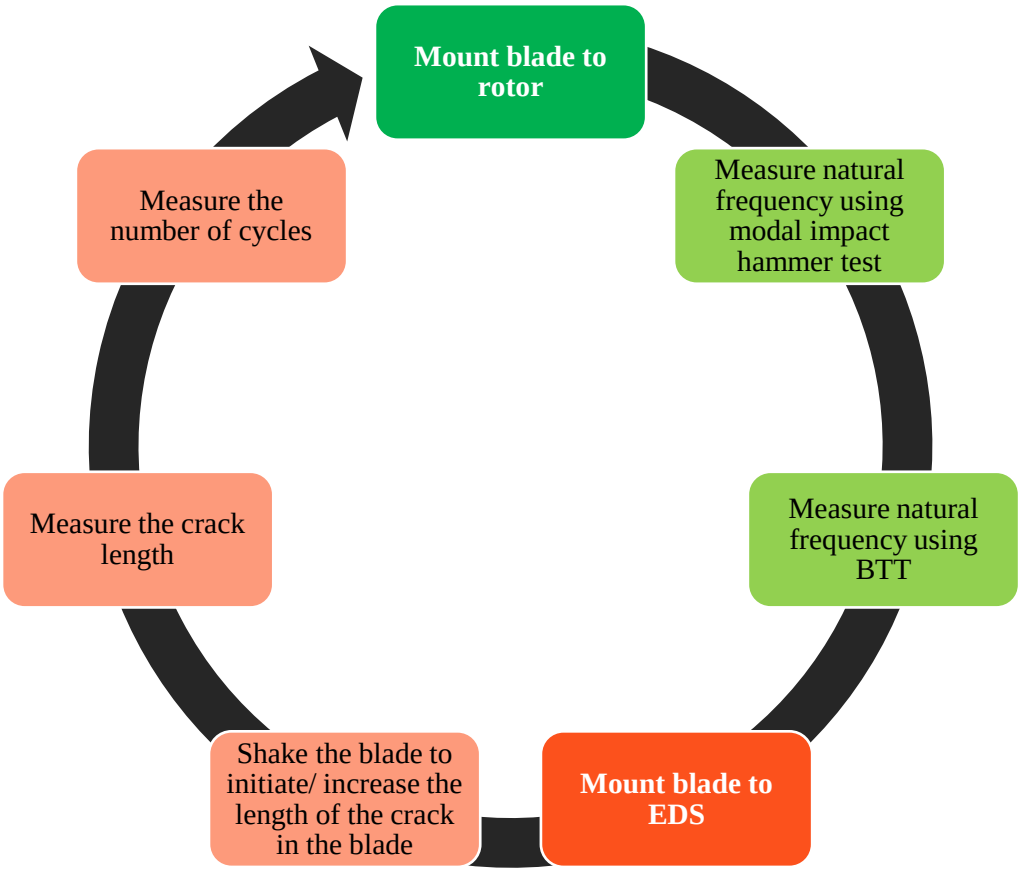

Figure 3.7: Experimental procedure repeated multiple times for all ten rotor blades.

3.2.6. Dissertation structure

The answers to the research questions proposed in Section 3.1 are contained in the following chapters. Results of the experiments conducted in Section 3.2.3 provide validation of the methodologies derived in this dissertation. The following chapters are presented in this dissertation:

- *Chapter 4: Measuring angular tip displacement*. In this section the time of arrival signal is interpreted to determine the response of the blade.
- *Chapter 5: Features of damaged blades*. A novel method for determining the resonating frequencies of a blade is proposed. The results of this section show that BTT can be used to determine the natural frequency of the blade in real time.
- *Chapter 6: Measure damage from the natural frequency*. Here a diagnostics model is constructed using data collected during the experiments and finite element simulations. The hybrid method uses estimates of the natural frequency to provide an approximation of the current crack length in the blade.
- *Chapter 7: Estimate RUL*. This section concludes the comprehensive workflow in this dissertation by providing a method for estimating the RUL of a rotor blade after a couple of diagnostic estimates have been performed on the blade.

4. BTT: Measuring relative angular tip displacement

This section addresses the method of determining time of arrival and angular tip displacement of a rotor blade from sensor readings.

4.1. Time of arrival pulses of proximity probes

BTT requires two types of measured signals namely (i) a shaft encoder signal and (ii) a proximity probe signal. Typical measurements of a proximity probe are shown in Figure 4.1. The figure also shows a zoomed graph of the single pulse highlighted in red on the graph on the left. The pulse is generated due to the blade tip passing the eddy current proximity probe.

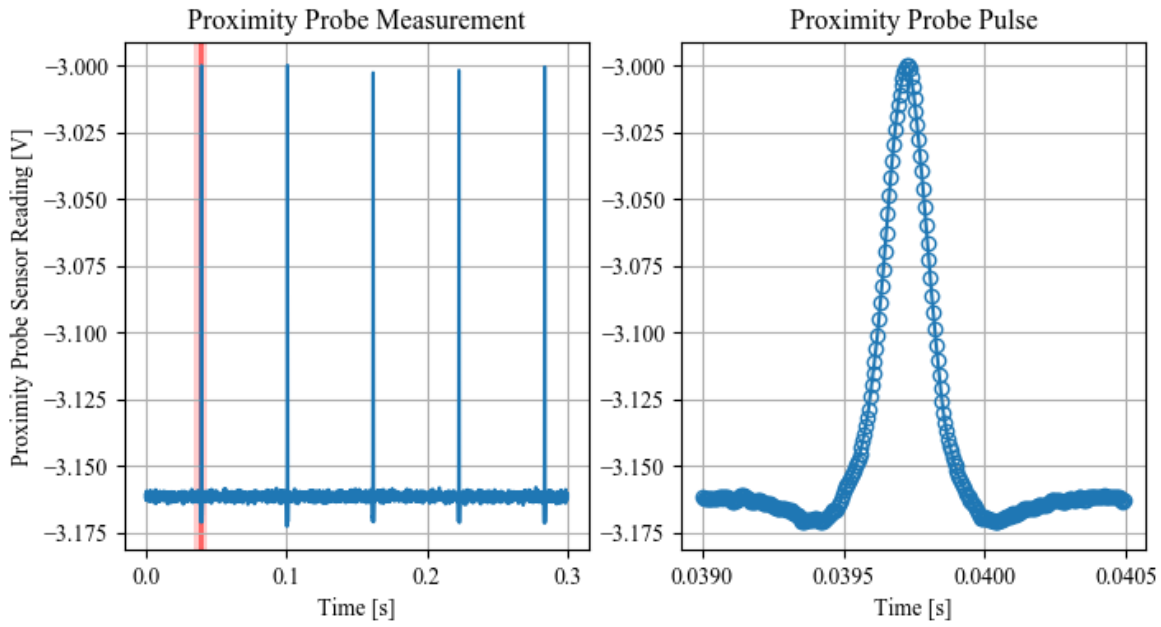

Figure 4.1: Typical proximity probe signal of a single blade rotating at a constant angular velocity (left) with a zoomed graph on a single pulse (right).

Notice, that due to the sampling frequency ($195\ kHz$) a complete shape of the pulse is easily shown. This is sometimes not the case, since the pulse width is dependent on the velocity of the rotor. If the rotor is spinning at maximum speed, fewer samples will be captured along the width of the pulse. Consequently, the triggering criteria used to determine the ToA of the blade has a notable effect. Furthermore, since most of the signal does not contain valuable information it is computationally efficient to specify a trigger level to detect the times at which pulses occur.

This dissertation considers four types of criteria for determining the time of arrival (ToA) of the blade. These criteria are (i) the local maximum time of the pulse, (ii) the positive slope trigger, (iii) the negative slope trigger and (iv) the average between the positive and negative slope trigger. Figure 4.2 shows the first three of the possible choices for the ToA. The fourth trigger criterion is an average between the

positive slope (left ToA trigger) and the negative slope (right ToA trigger). The figure on the right shows a pulse measured at a lower sampling rate (15 kHz). Observe that at a lower sampling rate the local maximum ToA trigger criterion has an error of approximately 36 μs when compared to the higher sampling rate signal. Compare this to the error of the positive slope triggering criterion of approximately 5 μs. The negative slope triggering criterion has no error in this case. Therefore, the positive and negative slope trigger times are used as the ToA for the blade.

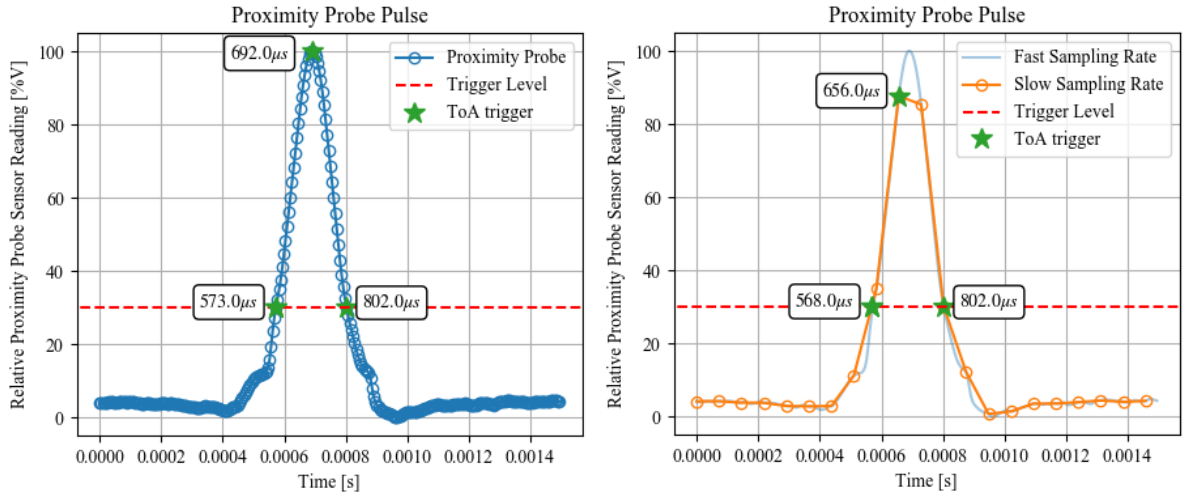

Figure 4.2: Time of Arrival (ToA) triggers on a single proximity probe pulse measured at 195 kHz with a trigger level set to 30% of the normalised pulse signal (left). The same pulse measured at a lower sampling rate (15 kHz) with the ToA triggers computed from the new signal (right).

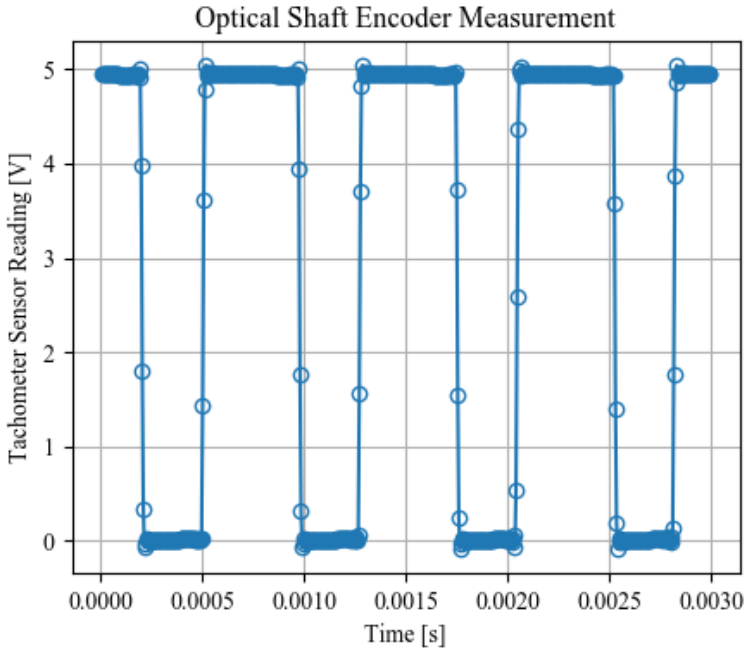

Figure 4.3: Measured voltage signal of a 79 pulses per revolution optical shaft encoder for a shaft rotating at an arbitrary angular velocity.

Figure 4.3 shows a typical tachometer signal of an optical shaft encoder with 79 pulses per revolution. The Instantaneous Angular Speed (Ω_{IAS}) or the Average Angular Speed (Ω_{AAS}) of the shaft is determined from the positive or negative trigger slope zero crossing times using equation (4.1) and (4.2) respectively. The values $\Delta\theta_{encoder}$, t_n, and ppr denote the encoder spacing, the n^{th} zero-crossing time and the number of pulses per revolution respectively.

$$\Omega_{IAS}(t_n) = \frac{\Delta\theta_{encoder}}{(t_n - t_{n-1})} \cong \frac{2\pi}{ppr(t_n - t_{n-1})} \tag{4.1}$$

$$\Omega_{AAS}(t_n) = \frac{2\pi}{(t_n - t_{n-ppr})} \tag{4.2}$$

Equation (4.1) assumes a constant angular spacing between pulses. This assumption is problematic for irregularly spaced encoders. Zebra encoder strips, used by optical shaft encoders, are prone to irregular encoder spacings due to the methods used to prepare these encoders and attach them to shafts. Diamond, Heyns and Oberholster (2019) proposed an improved method for determining angular velocities from multiple pulses per revolution (MPR) sensors that are prone to this irregular spacing. This method uses Bayesian inference to learn the geometry of the shaft encoder by making assumptions on the acceleration of the shaft. These improved methods allow one to measure the angular velocity more precisely than the approximation in equation (4.1). The results from the inference method determines approximations of the values of $\Delta\theta_{encoder}$ over the entire circumference of the shaft encoder strip such that a smoother curve is obtained when using equation (4.1).

Figure 4.4 shows the rotor shaft speed as determined by equation (4.1) and (4.2). The Bayesian geometry compensation method recommended by Diamond, Heyns and Oberholster (2019) is performed on the shaft encoder signal and the resulting angular velocity is shown in orange in Figure 4.4. Figure 4.4 shows that equation (4.2) provides the least variation in determining the angular shaft speed of the rotor. However, in this method the MPR sensor is interpreted as an OPR sensor and there is a loss of information when using this method. Notice that geometry compensated signal reduced the variation in the shaft speed compared to the results of equation (4.1) shown in blue.

The shaft encoder section distances ($\Delta\theta_{encoder}$) computed from the geometry compensation method is shown in Figure 4.5 for the 79 pulses per revolution shaft encoder. The blue line shows the approximation used to determine the angular velocity in equation (4.1) and the orange line shows the results from the inference method for each section of the encoder strip.

This dissertation, therefore, uses the geometry compensated relative angular velocity to determine the rotor shaft speed from the zero crossing times of the MPR shaft encoder signal.

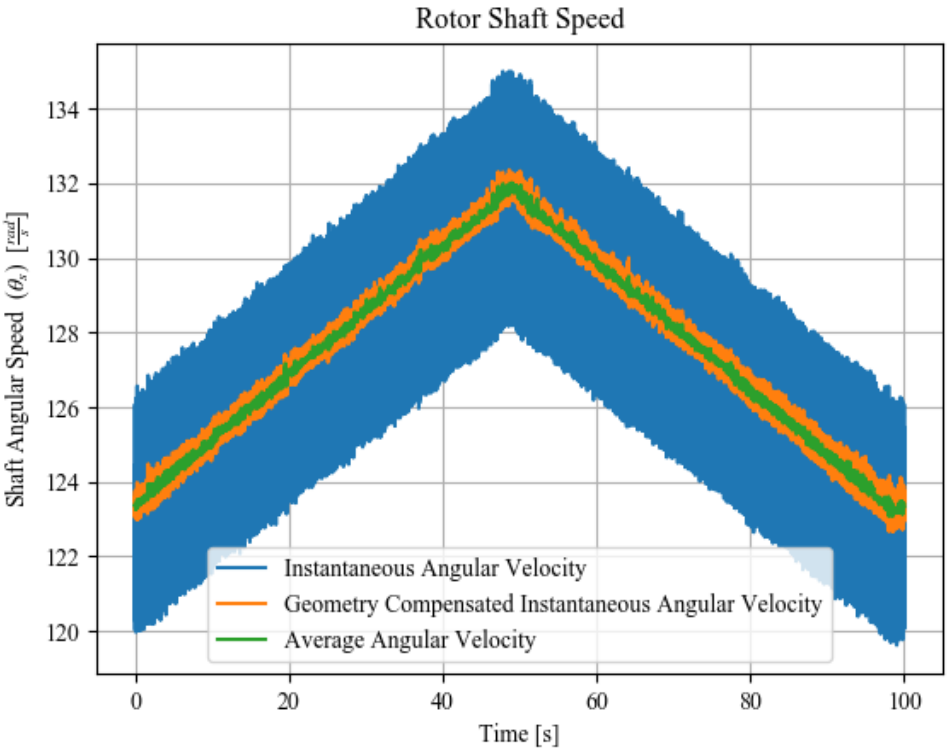

Figure 4.4: Instantaneous angular velocity, geometry compensated angular velocity and the average angular velocity calculated from the zero-crossing times of the shaft encoder signal.

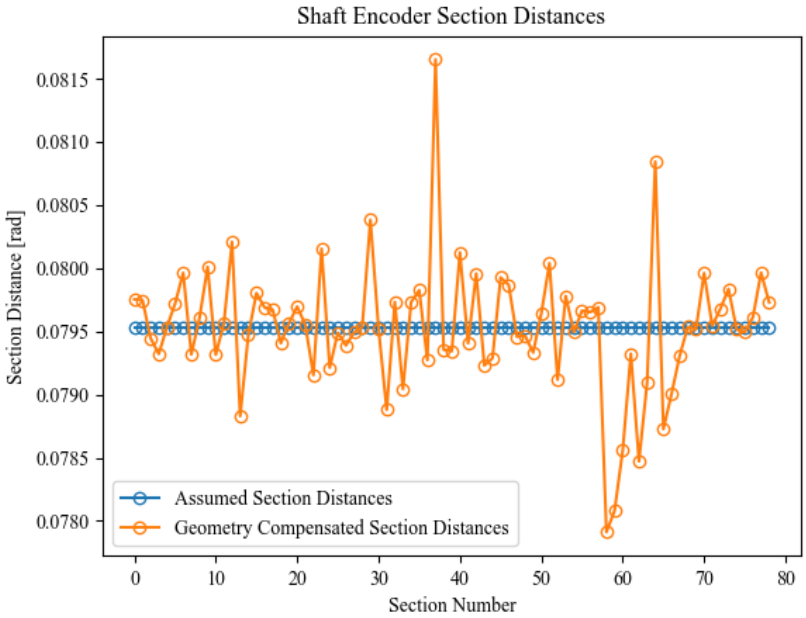

Figure 4.5: Geometry compensated shaft encoder section distances compared to the assumed section distances of the instantaneous angular velocity in equation (4.1)

4.2. Angular tip displacement relative to shaft

The relative angular displacement of the blade tip with respect to the rotor shaft is denoted $\theta_{b/s}$. Equation (4.3) relates the first derivative of the relative angular tip displacement to the absolute angular velocity of the tip ($\dot{\theta}_b$) and the shaft ($\dot{\theta}_s$). Note that these velocities are approximated from the measurements of the proximity probe and shaft encoder respectively.

$$\dot{\theta}_{b/s}(t) = \dot{\theta}_b(t) - \dot{\theta}_s(t) \tag{4.3}$$

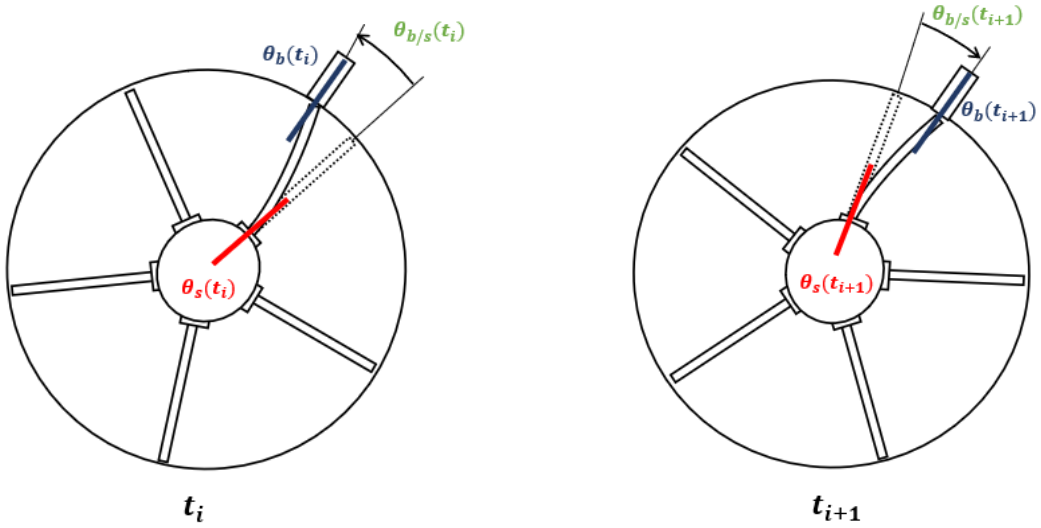

(a) (b)

Figure 4.6: Two potential sequential time of arrival configurations at ToA pulse t_i (a) and at ToA pulse t_{i+1} (b)

Consider two sequential ToA pulse measurements denoted as t_i and t_{i+1} shown in Figure 4.6. It is important to distinguish between the displacement (θ_b) of the blade and the relative displacement of blade with respect to the shaft ($\theta_{b/s}$). After two sequential ToA pulses, for a single blade, the total displacement of the blade tip is equal to one full revolution (2π radians). This is because the proximity probe remains in place and simply detects when the blade tip passes the probe. It is assumed that the rotor only has positive angular velocity. After two associated pulses the tip of the blade has reached the same point. Thus, integrating equation (4.3) and using the net change theorem in equation (4.4) the difference in relative angular displacement is calculated using equation (4.5). This equation is also shown in Figure 4.7. The resulting calculation now describes the relative angular displacement as a function of the tachometer signal integrated between the two ToAs.

$$\int_{t_i}^{t_{i+1}} \dot{\theta}_{b/s}(\tau)d\tau = \left[\Delta\theta_{b/s}\right]_{t_i}^{t_{i+1}} = \theta_{b/s}(t_{i+1}) - \theta_{b/s}(t_i) \tag{4.4}$$

$$\left[\Delta\theta_{b/s}\right]_{t_i}^{t_{i+1}} = \int_{t_i}^{t_{i+1}} \dot{\theta}_b\,(\tau)d\tau - \int_{t_i}^{t_{i+1}} \dot{\theta}_s(\tau)d\tau = 2\pi - \int_{t_i}^{t_{i+1}} \dot{\theta}_s\,(\tau)\,d\tau \tag{4.5}$$

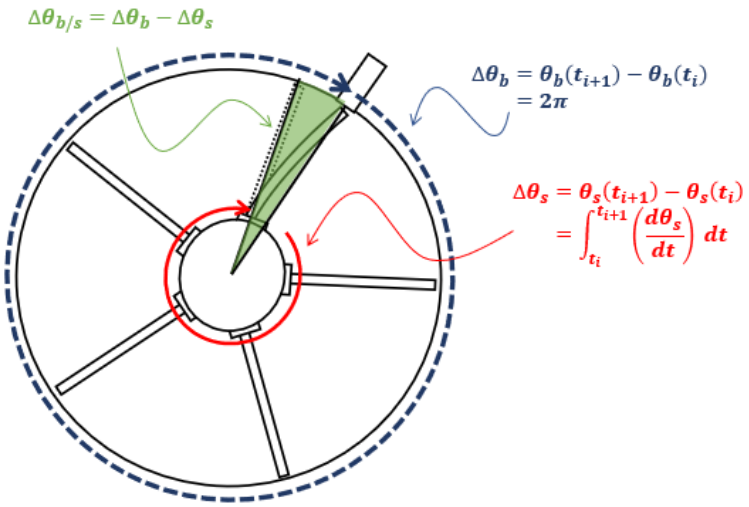

Figure 4.7: The angular displacement of the blade tip relative to the shaft between two ToA measurements.

The relative angular displacement at each ToA is determined from the cumulative summation of equation (4.5). Therefore, the measured value of the relative angular displacement is computed using equation (4.6) at every ToA (t_n). Note however, that due to the formulation of this problem an initial boundary condition is required. That is, the relative angular displacement needs to be known for at least one of the ToA pulses. This is unfortunately very difficult to compute exactly from the measured data since this requires knowledge of the deflection of the blade tip relative to the shaft at the first ToA. Nevertheless, the simplifying assumption of setting $\theta_{b/s}(t_0)$ to zero is made. The resulting signal $\theta_{b/s}(t_n)$ will therefore have a bias offset associated with it. The raw displacement values from different proximity probe sensors must therefore be zeroed before they are used in a BTT algorithm.

$$\theta_{b/s}(t_n) = \theta_{b/s}(t_0) + \sum_{i=0}^{n-1} \left[\Delta\theta_{b/s}\right]_{t_i}^{t_{i+1}} \tag{4.6}$$

Figure 4.8 illustrates an implementation of these computational steps on data from the BTT test setup with a single blade mounted to the rotor. The shaft is driven according to the profile shown in Figure 4.8 (a) and the blade response is shown for the three proximity probes in Figure 4.8 (b). Recall, the displacement values may not represent the signal exactly. Thus, the relative angular displacement of each proximity probe may change in the vertical axis.

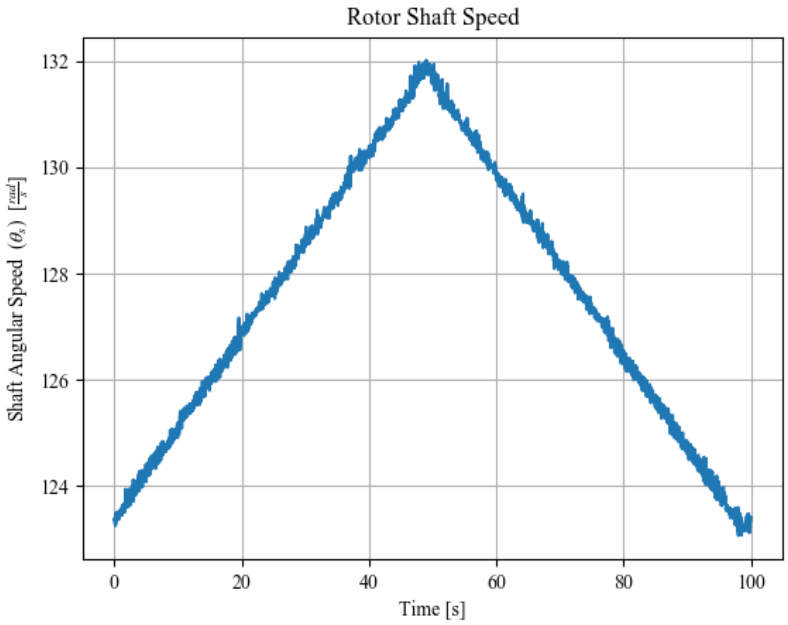

(a)

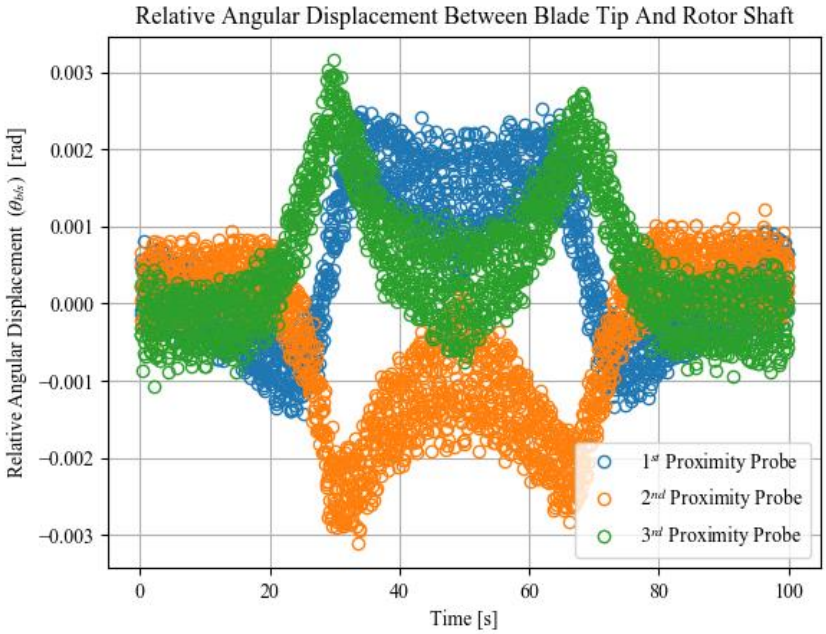

(b)

Figure 4.8: Average angular velocity of the rotor shaft (a) and the associated relative angular tip displacement (b) of a single blade passing three different proximity probes.

The relative angular displacement response of the blade shows large changes in the amplitude at approximately 30s and 70s. These amplitudes are consistent with the same rotor shaft speed namely 128 rad/s. These peaks indicate a resonance in the response of the blade and are called the critical speeds of the rotor blade. The following chapter considers using these critical speeds to estimate he natural frequency of the blade.

5. Signal processing: Features of damaged blades

The first natural frequency of a blade is an important quantity to be extracted from BTT signals, since it is used extensively for structural health monitoring (Elshamy, Crosby and Elhadary, 2018; Khalkar, 2018). This chapter proposes a method for determining the natural frequency of a rotor blade from the relative angular displacement of the blade. The proposed method determines the shaft speeds (critical speeds) that cause resonance of the blade tip with respect to the shaft. The natural frequency is then determined by compensating for the artificial stiffening of the blade during rotation using a Campbell diagram. The method is applied to the blade tip response measured from the experiments.

In this section, a model is also presented that simulates the complete analytical response of the blade tip. The model is a SDOF model and experiences loads that emulate the loading conditions of the blade during the experiment. The purpose of the model is to approximate the response of the blade as a continuous signal, contrary to a discrete signal obtained from processing ToA signals (using the method discussed in Chapter 4). During the BTT experiments only event-based data is collected. The entire response of the blade is simulated and studied to understand the frequency content of the response of the blade during the experiment. The method for determining the natural frequency is then applied to the simulated analytical model and the results are compared to the data obtained from the experiments. The model confirms that the natural frequency is obtained from the newly proposed method. The limitations and shortcomings of the method are also discussed.

This chapter concludes by comparing the natural frequency estimations obtained from the BTT data to measurements of the impact modal hammer test. The comparison is made for all the data collected from the damaged blades in the experiment.

5.1. Determining natural frequency from blade response

Ideally, a Fourier analysis such as the DFT or the STFT is applied to BTT data. However, as discussed in Section 2.3.2, these methods have two types of limitations namely (i) irregular sampling frequency and (ii) the Nyquist frequency limit. This section considers an alternative means of analysing BTT data to determine the frequency response of the blade tip due to the rotor shaft speed. This alternative method shares its origins with the Lomb-Scargle periodogram (VanderPlas, 2018).

Consider a blade response to have the functional form in equation (5.1). The model in equation (5.1) is a linear model in terms of A, B and C. This form has significant implications for determining the natural frequency of the rotor blade. Since the model is approximated as a single degree of freedom system, the blade response is simply described as a function of the excitation frequency and its associated amplitude ($\mathcal{A}$) and phase (ϕ). The amplitude and phase are calculated using equation (5.2) and equation (5.3) respectively.

$$\theta_{b/s}(t) = A\cos(2\pi f t) + B\sin(2\pi f t) + C \tag{5.1}$$

$$\mathcal{A} = \sqrt{A^2 + B^2} \tag{5.2}$$

$$\phi = \tan^{-1}\left(\frac{B}{A}\right) \tag{5.3}$$

The power spectral density of the signal (P_{LSSA}) is the square of the amplitude in equation (5.2). The Lomb-Scargle periodogram determines the power spectral density using a least squares fit

$$P_{LSSA} = |\mathcal{A}|^2 = |A^2 + B^2| \tag{5.4}$$

As discussed in Section 4.2, the data collected from a single proximity probe depends on the initial relative angular displacement at the first time of arrival for each proximity probe. This value is constant for each proximity probe. This means each probe has its own bias offset. Therefore equation (5.5) proposes a model for determining the relative tip displacement as a function of time from three proximity probes. This equation can easily be expanded for more proximity probes by introducing more constant C parameters. The value n represents the number of revolutions that occurred during the collection of the blade displacement data ($n \in \mathbb{Z}$).

$$\theta_{b/s}(t_k) = \begin{cases} A\cos(2\pi f t_k) + B\sin(2\pi f t_k) + C_{probe\,1} & if\ k \in \{0,3,6,\dots,3n\} \\ A\cos(2\pi f t_k) + B\sin(2\pi f t_k) + C_{probe\,2} & if\ k \in \{1,4,7,\dots,3n+1\} \\ A\cos(2\pi f t_k) + B\sin(2\pi f t_k) + C_{probe\,3} & if\ k \in \{2,5,8,\dots 3n+2\} \end{cases} \tag{5.5}$$

This equation is better understood in the form of equation (5.6) where the data collected for each BTT measurement is substituted in equation (5.5) to provide a linear model between the unknown coefficients (A, B, $C_{probe\,1}$, $C_{probe\,2}$ and $C_{probe\,3}$). Notice that the offset coefficients are only added to the relative angular displacement associated with the probe that detected the time of arrival pulse.

$$\begin{Bmatrix} \theta_{b/s}(t_0) \\ \theta_{b/s}(t_1) \\ \theta_{b/s}(t_2) \\ \theta_{b/s}(t_3) \\ \vdots \\ \theta_{b/s}(t_n) \end{Bmatrix} = \begin{bmatrix} \cos(2\pi f t_0) & \sin(2\pi f t_0) & 1 & 0 & 0 \\ \cos(2\pi f t_1) & \sin(2\pi f t_1) & 0 & 1 & 0 \\ \cos(2\pi f t_2) & \sin(2\pi f t_2) & 0 & 0 & 1 \\ \cos(2\pi f t_3) & \sin(2\pi f t_3) & 1 & 0 & 0 \\ \vdots & \vdots & \vdots & \vdots & \vdots \\ \cos(2\pi f t_n) & \sin(2\pi f t_n) & 0 & 0 & 1 \end{bmatrix} \begin{Bmatrix} A \\ B \\ C_{probe\,1} \\ C_{probe\,2} \\ C_{probe\,3} \end{Bmatrix} \tag{5.6}$$

Provided enough BTT data $\theta_{b/s}(t_k)$ is collected for each proximity probe; the maximum likelihood estimation or least squares regression estimate of the parameters A, B, $C_{probe\,1}$, $C_{probe\,2}$ and $C_{probe\,3}$ can be determined. The maximum likelihood solution is the coefficients that maximise the probability of the data given the model in equation (5.5). However, the model requires the frequency (f) to compute this estimate. The Lomb-Scargle periodogram assumes values for f. The method then solves the least squares regression problem for the model for all the interrogated frequencies. The model that produces

the highest power spectral density in equation (5.4) is the maximum likelihood estimate to the probability of the frequency given the model and the data, that is $\underset{w.r.t\ f}{\operatorname{argmax}}\, \mathcal{P}(f|\mathcal{D}, M)$.

Solving the coefficients in equation (5.6) provides a likelihood value for the resonating frequency as a function of excitation frequency. The solution is therefore similar to a frequency response function (FRF). The Lomb-Scargle periodogram have a lot of similarities to the proposed method, however, the proposed method is particularly adapted for BTT data. The results from the Lomb-Scargle periodogram yields inconsistent results for BTT data. Also, the frequency range to interrogate is primarily determined from the excitation frequency.

To illustrate the proposed method, least squares regression is performed on the data from Figure 4.8. A window size of 100 datapoints is selected and a frequency range equal to the shaft speed range is interrogated. This interrogation window is moved from the start of the recorded data to the end and the measurement and the power spectral density is recorded for all interrogated frequencies. Figure 5.1 shows a contour plot of the power spectral density at the average time of the 100 datapoints for the entire spectrum of time. One could think of the diagram as a combination of modified Lomb-Scargle periodograms stacked next to one another in the time domain. The actual excitation frequency is plotted over the entire contour plot. It is shown in Figure 5.1 that the method detects the critical speeds of the rotor. The peak amplitude for each second in the time domain corresponds with the shaft excitation frequency.

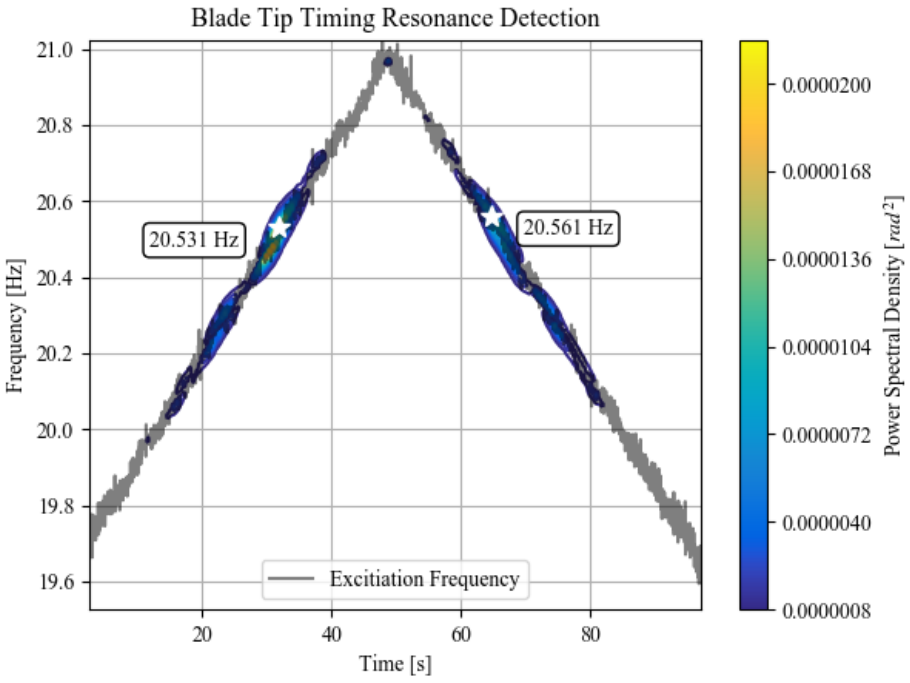

Figure 5.1: Contour plot of the BTT resonance detection algorithm compared with the shaft excitation frequency.

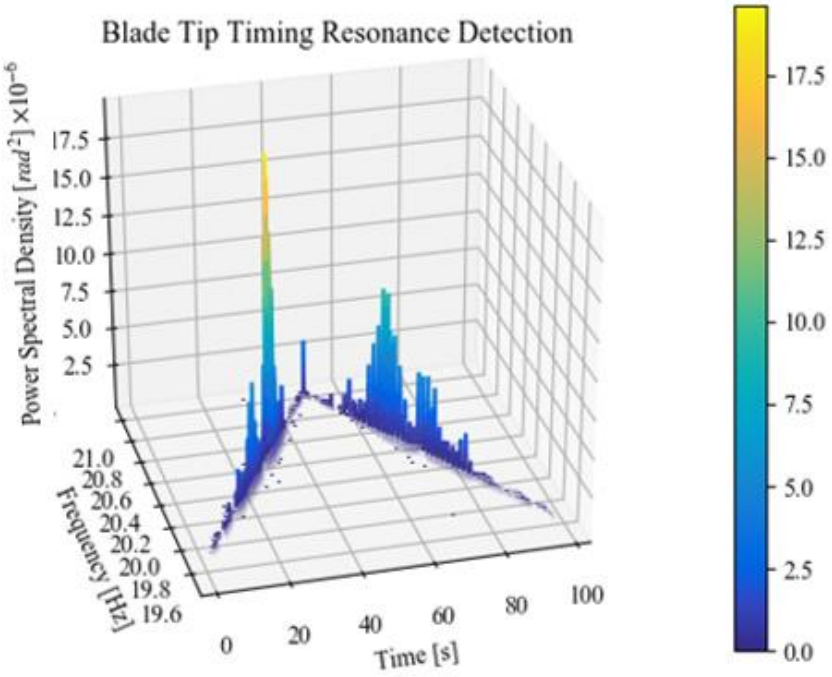

Figure 5.2: Waterfall plot of the BTT resonance detection algorithm.

Notice that along the excitation frequency curve, the amplitude changes. At a certain speed the amplitude becomes large and this seems to correspond with the locations of the peaks in Figure 4.8. These resonance peaks are marked with white stars and the corresponding frequencies are annotated on the graph. This result is better shown in Figure 5.3 where amplitude is plotted over time for the run-up and run-down of the rotor. The same resonance peaks are shown with red crosses.

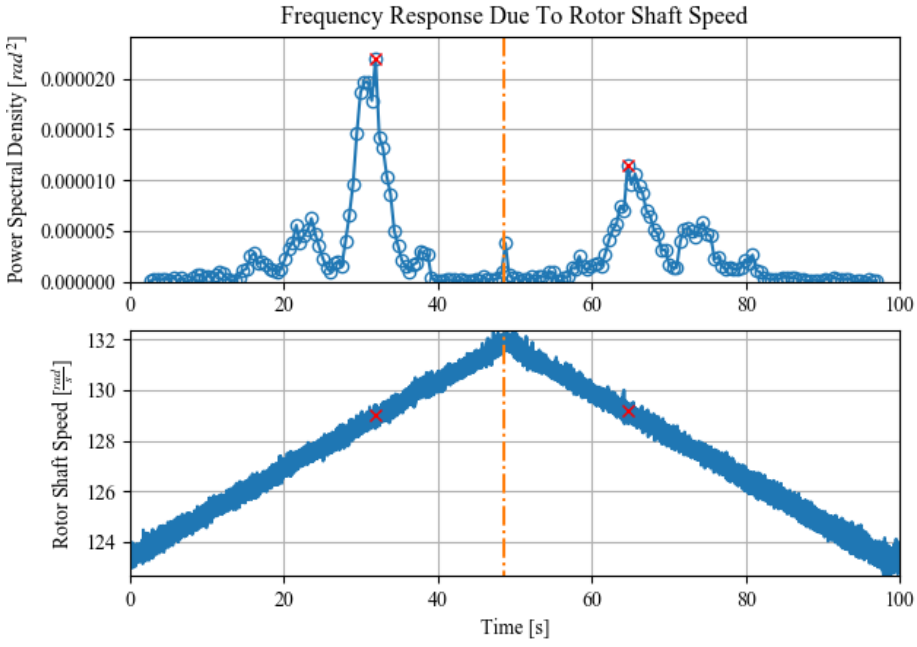

Figure 5.3: Frequency response function from interrogated resonating frequencies over time (top) and the corresponding angular shaft speed (bottom).

Note that the peaks from Figure 5.1 and Figure 5.3 are only the resonating frequencies of the blade and not the natural frequency of the blade. Due to centrifugal stiffening of the blade at large angular velocities the first natural frequency does not remain constant (Meherwan, 2012). A Campbell diagram is constructed in Figure 5.4 from ANSYS finite element modal analysis results. The only boundary conditions for the modal analysis is the fixed boundary condition at the base of the rotor blade and an imposed rotational velocity at the location of centre of the shaft.

The blue curve in Figure 5.4 is approximated using equation (5.7). The function relates the new natural frequency (f_n) to the natural frequency when the blade is stationary (f_{n0}). The angular shaft speed is denoted f_s.

$$f_n = 0.0022(f_s)^2 + 0.0002\,(f_s) + f_{n_0} \tag{5.7}$$

Since, the methods derived in this section find the critical shaft speeds of the blade, the natural frequency of the blade is equal to the engine order (EO) times the shaft speed (f_s). This frequency at which resonance occurs is equal to the natural frequency when the blade is resonating. Equation (5.8) is the final step required to find the natural frequency of the blade at the stationary angular velocity reference frame. Equation (5.8) is only valid for shaft speeds that cause the blade tip to resonate.

$$f_{n_0} = EO(f_s) - 0.0022(f_s)^2 - 0.0002(f_s) \tag{5.8}$$

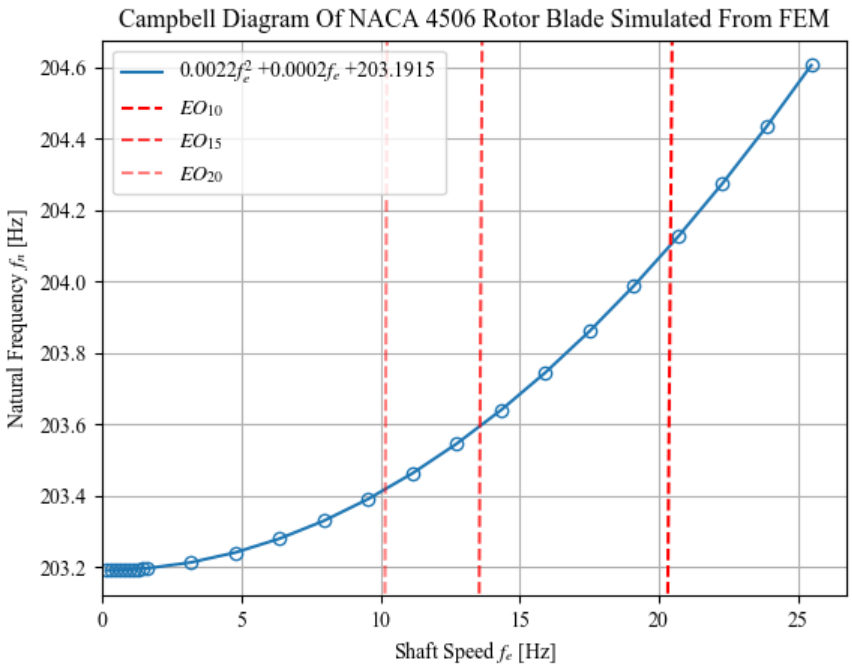

Figure 5.4: Campbell diagram of NACA 4506 rotor blade simulated from finite element model.

5.2. Modelling blade tip response and BTT measurements

This section proposes a single degree of freedom model to analytically approximate the response of a blade during the experiment. Ideally, the response of the relative tip displacement should be characterized by the blade's natural frequency. This mainly occurs when the blade experiences resonance at a critical speed. At critical speeds harmonics of the excitation frequency due to the fluid exerting a pressure on the blade is equal to the natural frequency of the blade. In the BTT experiment a single blow off air nozzle is used to excite the blade during rotation.

The purpose of the analytical model is to determine the frequency response of the blade tip due to the nozzle and the speed at which the shaft is spinning. The reason for this model is to obtain a continuous blade response time history instead of discrete points. Analysing the frequency content of the analytical response of the model allows a complete understanding of what to expect from the proposed method, in Section 5.1, for determining the natural frequency.

Consider the free body diagram in Figure 5.5 and the associated equation of motion for a single blade shown in equation (5.11). This model only approximates the first mode (flap mode) of the rotor blade as a single degree of freedom (SDOF) model. The relative tip displacement is denoted $\theta_{b/s}$ and the displacement of the shaft is θ_s. The displacement of the blade (θ_b) follows the displacement of the shaft. The blade experiences dynamic loading expressed by a forcing function added to the SDOF model.

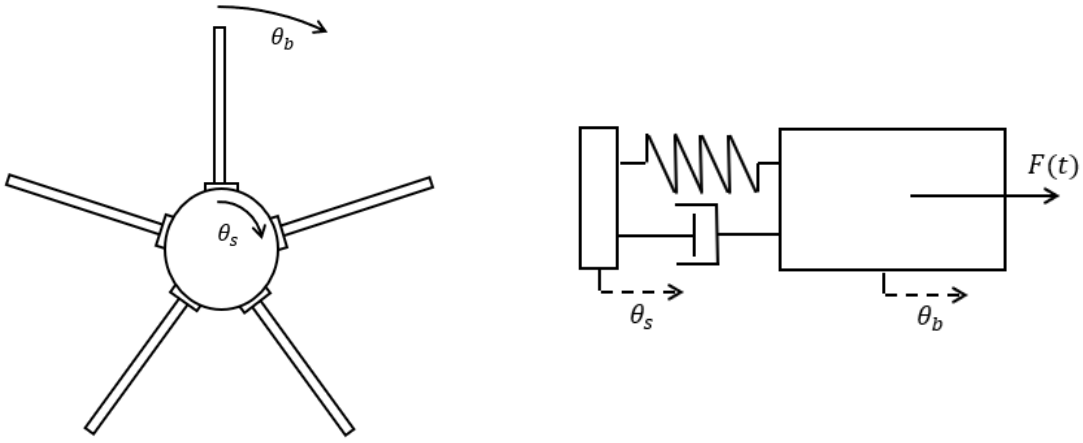

(a) (b)

Figure 5.5: Rotor blade setup (a) and a single degree of freedom approximation model for blade tip displacement relative to the shaft (b)

$$J_b\ddot{\theta}_b + c\dot{\theta}_b + k\theta_b = c\dot{\theta}_s + k\theta_s + T(t) \tag{5.9}$$

$$\theta_{b/s} = \theta_b - \theta_s \tag{5.10}$$

$$J_b\ddot{\theta}_{b/s} + c\dot{\theta}_{b/s} + k\theta_{b/s} = -J_b\ddot{\theta}_s + \mathrm{T}(t) \tag{5.11}$$

It is assumed that the rotor is balanced, and structurally transmitted vibrations are negligible. This is an important assumption since Gubran (2015) showed that rotor imbalance could cause excitation in the blades. Gravitational forces are also neglected in this model. The loads experienced by the blade are summarised in Section 2.2.2.

In the experiment, the moment on the blade originates from the momentum change of the air. Since the blade only experiences a load when the blade is positioned close to the nozzle, the moment applied to the blade is rather a function of the shaft displacement than a function of time ($T(\theta_s)$). A discrete impulse equation is used in this simulation to emulate the load from a single blow-off nozzle. Equation (5.12) describes an approximation of the aerodynamic load that the blade experiences during rotation. Figure 5.6 (a) shows the rotor and the location of the high velocity stream of air. The approximated load in equation (5.12) is shown in Figure 5.6 (b).

$$T(\theta_s) = \begin{cases} T_0, & \theta_s \text{ in a high velocity zone} \\ 0, & \theta_s \text{ in a low velocity zone} \end{cases} \tag{5.12}$$

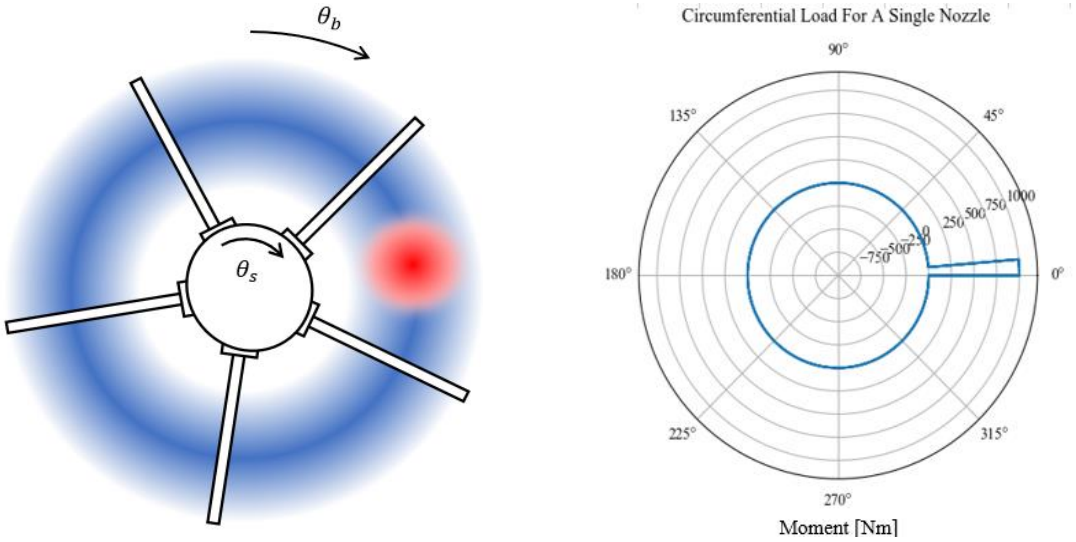

(a) (b)

Figure 5.6: Equivalent pressure load of a turbomachine blade for a single high velocity stream (a) and the associated moment applied to the blade tip during the simulation (b).

The response of the blade is solved by integrating the equation of motion using a 4th order Runge Kutta numerical integration method. However, the equation is first rewritten in the form of equation (5.13) and the relative velocity and displacement are solved simultaneously.

$$\begin{Bmatrix} \dot{\theta}_{b/s} \\ \ddot{\theta}_{b/s} \end{Bmatrix} = \begin{bmatrix} 0 & 1 \\ -\frac{k}{J_b} & -\frac{c}{J_b} \end{bmatrix} \begin{Bmatrix} \theta_{b/s} \\ \dot{\theta}_{b/s} \end{Bmatrix} + \frac{1}{J_b} \begin{Bmatrix} 0 \\ T(\theta_s) - J_b \ddot{\theta}_s \end{Bmatrix} \tag{5.13}$$

The shaft speed for this numerical simulation is a linear run up and run down of the shaft. This is depicted in Figure 5.7. The selected velocity profile is comparable to the speed of the rotor shaft during one of the experiments (shown in Figure 4.8). Additionally, all the parameters for this simulation are given in Table 5.1. These parameters are selected to model the response of a healthy rotor blade under loading conditions such as the experimental setup.

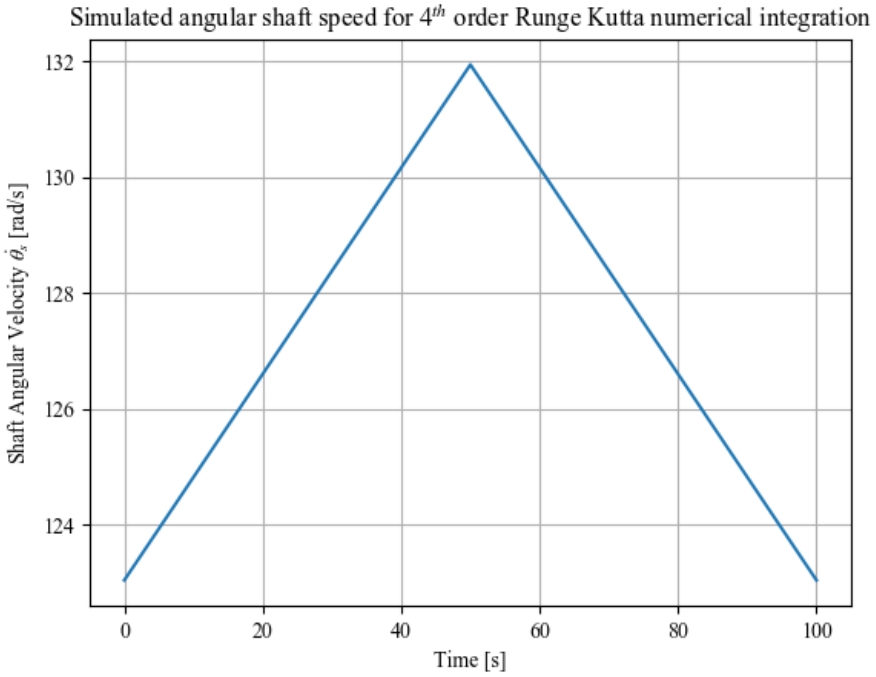

Figure 5.7: Simulated angular shaft speed for single high velocity stream of air.

Table 5.1: Parameters used in Runge Kutta numerical simulations of blade response.

Parameter	**Value**	**Units**
Minimum Shaft Speed	1175	RPM
Maximum Shaft Speed	1260	RPM
Stiffness (k)	8350	N/rad
Natural Frequency (f_n)	205	Hz
Damping Ratio (ζ)	0.01	$-$
Approximated Equivalent Force (F_0)	1	kN
High velocity pulse width	5	degrees
Runge Kutta integration step size	2×10^{-4}	s

The integrated response of the blade tip displacement is shown in Figure 5.8. The initial condition of the blade is selected at zero angular displacement and zero angular velocity. Notice that response of the amplitude of the blade increases at certain times. The peak of these amplitudes coincides with 10th engine order critical speed of the rotor.

The Discrete Fourier Transform (DFT) and Short Time Fourier Transform (STFT) of the response are shown in Figure 5.9 and Figure 5.10 respectively. The DFT indicates that the blade vibrates at its natural frequency. However, the STFT shows that the response is a superposition of integer harmonics of the rotor shaft speed. The amplitude of the response is large when any integer multiple of the shaft speed is equal to the natural frequency of the blade (green line in Figure 5.10). To show that the response of the blade happens in harmonics of shaft speed, a computed order tracking of the simulated blade response is shown in Figure 5.11. From Figure 5.11 it is shown that the rotor shaft speed excites the all synchronous engine orders. Resonance occurs when the 10^{th} engine order of the shaft speed is equal to the natural frequency of the blade.

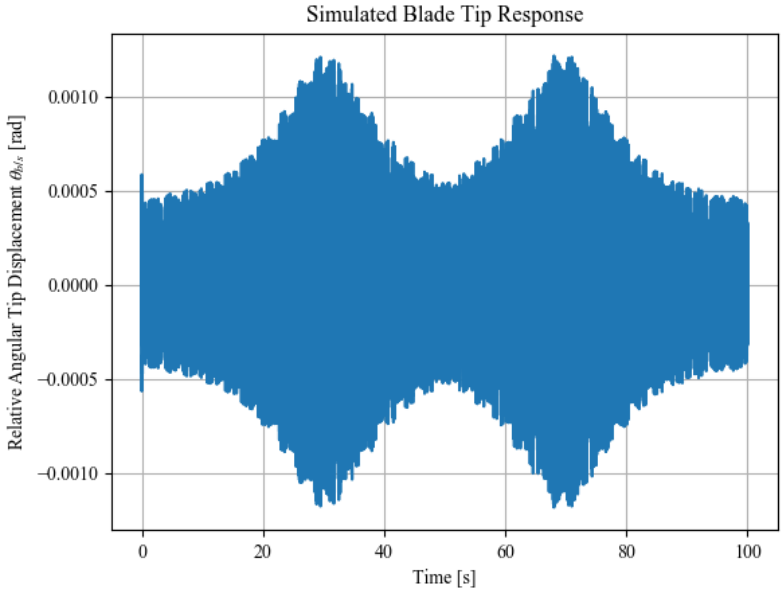

Figure 5.8: Simulated relative angular tip displacement results from Runge Kutta integration.

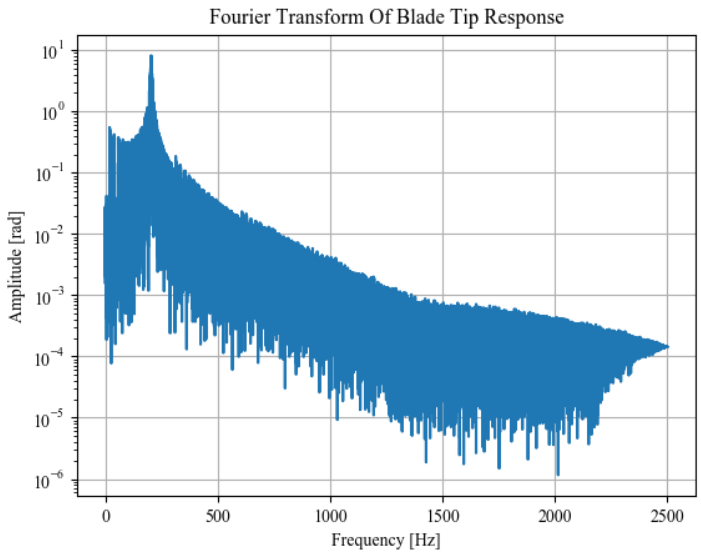

Figure 5.9: Fourier transform of simulated relative angular displacement of blade tip.

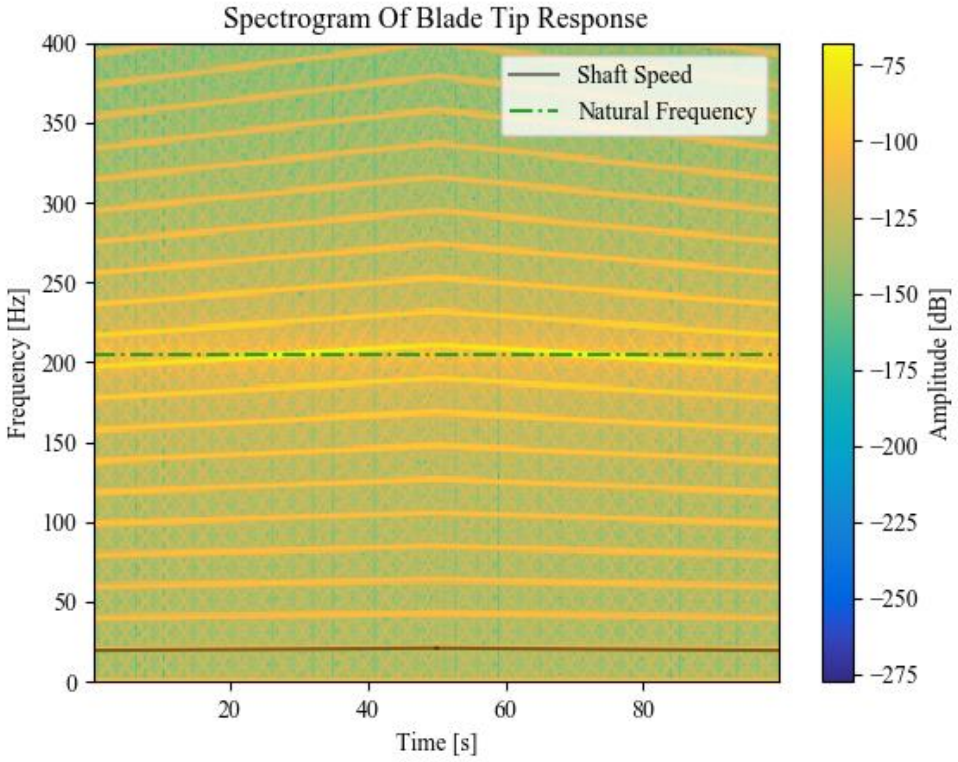

Figure 5.10: Short time Fourier Transform of simulated relative angular tip displacement of the blade.

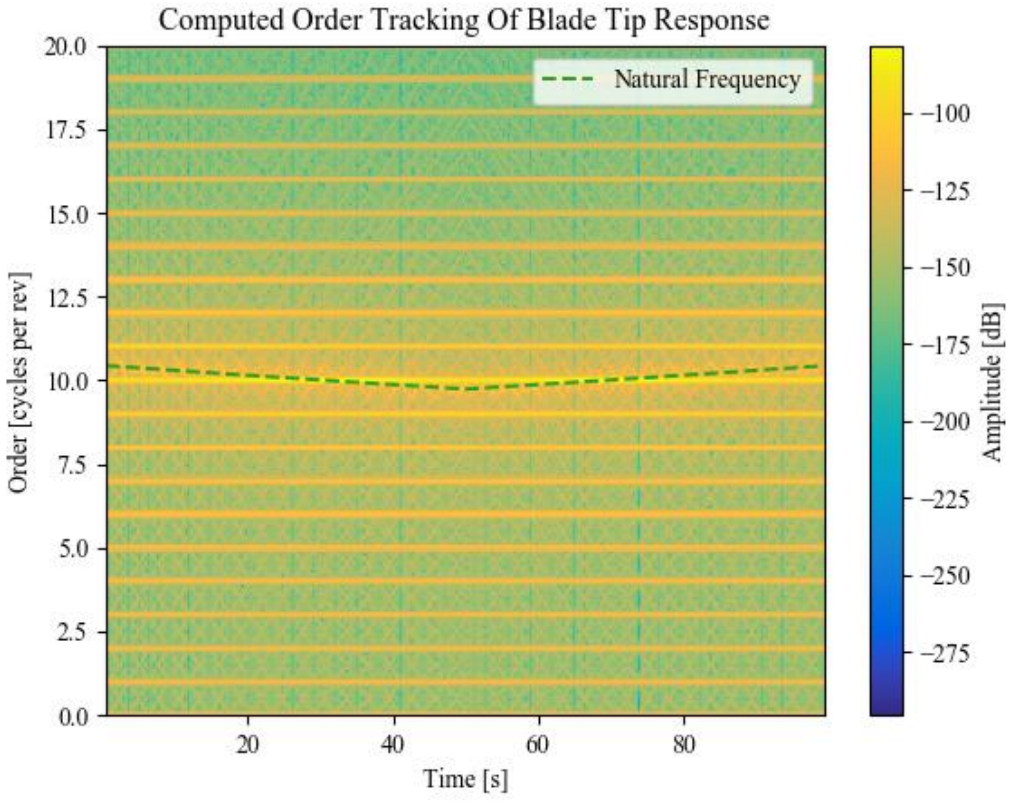

Figure 5.11: Computed order tracking of simulated relative angular tip displacement of the blade tip

BTT data is simulated from the analytical response of the SDOF model by resampling the blade tip deflection per revolution of the blade tip. Three arbitrary locations on the circumference of the rotor hub are selected for the placement of the proximity probes. The simulated "measurements" of relative angular tip displacement for the three proximity probes are shown in Figure 5.12. These data points are comparable to the blade tip response measured in Figure 4.8. The proposed resonance detection method is applied to the simulated BTT data to obtain Figure 5.13. The associated frequency response function is shown in Figure 5.14. The resonance detection method calculates a natural frequency equal to 205.15 Hz, which is 0.15 Hz larger than initially specified in Table 5.1.

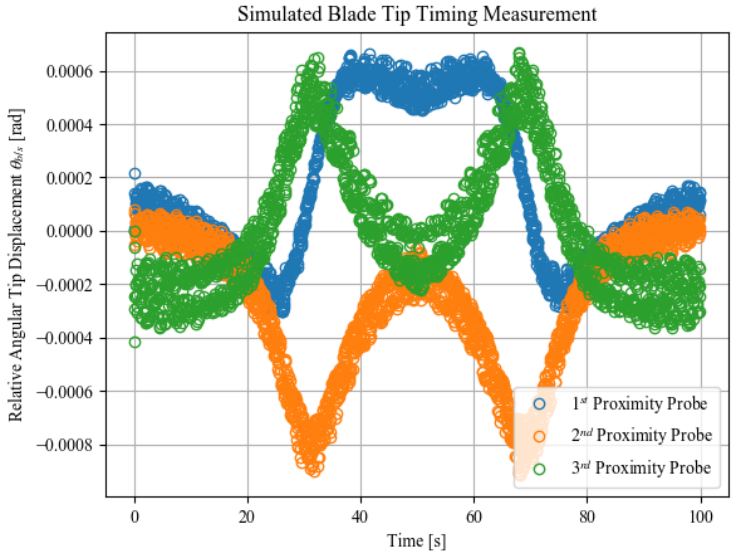

Figure 5.12: Simulated BTT data for three proximity probes sampled from the response in Figure 5.8

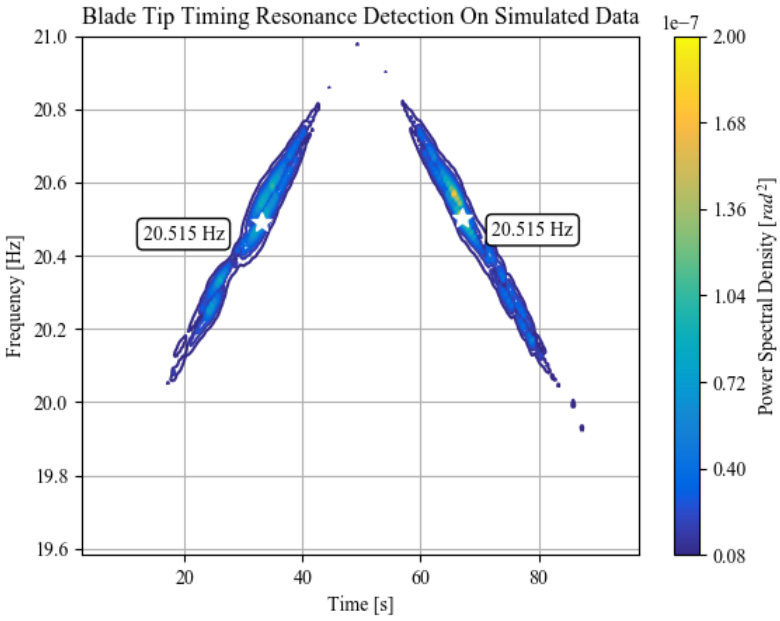

Figure 5.13: Contour plot of the proposed resonance detection method on the simulated BTT data.

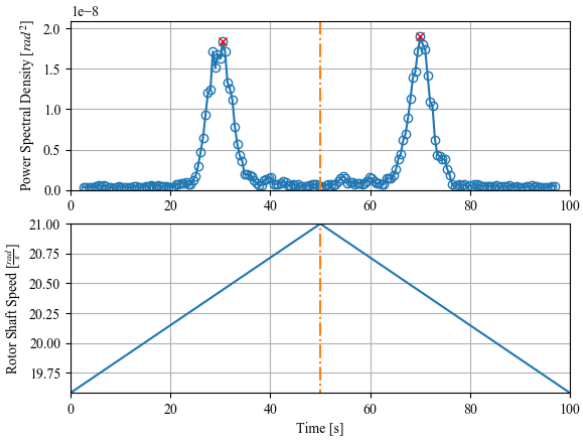

Figure 5.14: Frequency response function of the simulated BTT data.

The proposed method in Section 5.1 determines the critical speed of the rotor by interrogating selected frequencies. In this dissertation, the interrogated frequency range is equal to the range of the shaft speed. The method also works by interrogating a frequency range that contains the "actual" natural frequency of the blade. This is shown in Figure 5.15 where the selected frequency range is 10 times the shaft speed. Thus a 10th engine order of the shaft speed is expected to cause resonance of the blade tip. Figure 5.15 shows the power spectral density for the simulated BTT data and the measured experiment data. Notice the two methods show different results. The area indicated by the red arrow is not present in Figure 5.15 (a) and is not associated with an integer multiple of the shaft speed. That is, the blade tip in the experiment also vibrates non-synchronously. The analytical model in Figure 5.15 (a) only predicts synchronous vibration. However, knowing that synchronous resonance occurs at integer multiples of the shaft speed allows one to determine the natural frequency as the white stars in Figure 5.15 regardless of the presence of non-synchronous vibration of the blade tip.

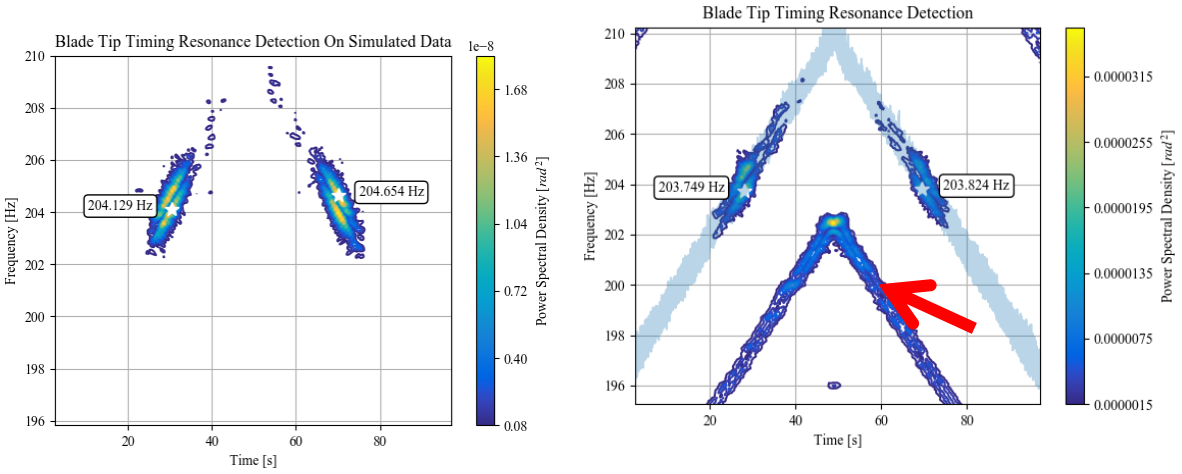

(a) (b)

Figure 5.15: Contour plots of the proposed resonance detection method with an interrogating frequency range containing the natural frequency of the simulated BTT data (a) and the experiment data (b).

5.3. BTT method compared to modal impact hammer results

Lastly, the natural frequency is determined from BTT for all the damaged blades in the experiment. The method is compared to measured natural frequencies of the blade from the modal impact hammer test. Figure 5.16 shows how the measurements compare with one another. The red line shows an exact correlation where both measurements of the natural frequency are equal. Notice that the method works quite well in estimating the natural frequency since almost all the points are on the red line. This graph therefore shows that the resonance detection algorithm works for the prescribed shaft speed.

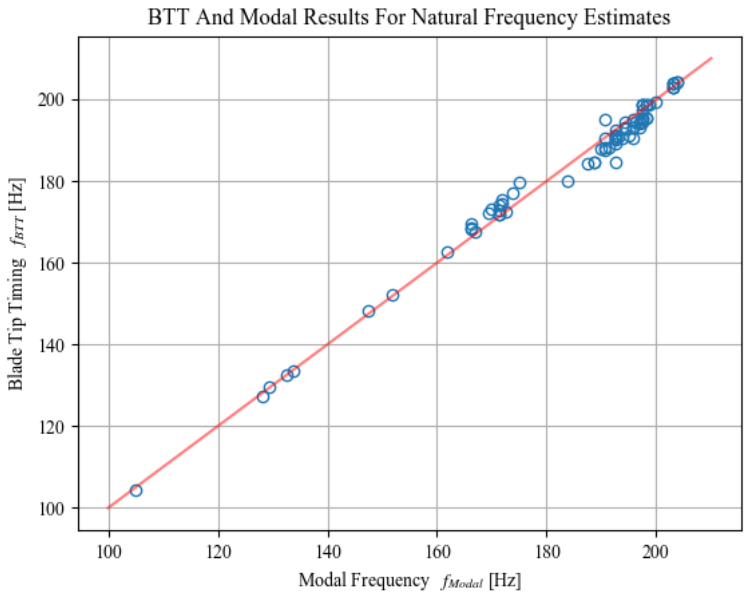

Figure 5.16: Comparison of the natural frequency measured from BTT with the natural frequency measured from a modal impact hammer test

In summary, this chapter shows that the blade natural frequency is found from BTT data. First, the signal is converted to time of arrival pulses by using a trigger criterion. These pulses are then compared to angular velocity of the shaft to find the displacement of the blade tip relative to the shaft using equation (4.5) and (4.6). Next, the critical speed is determined from the response of the blade. A least square spectral analysis (LSSA) method is derived for determining the critical speed at which the blade tip experiences resonance. The method interrogates possible critical speeds and a frequency response function is generated for the blade, as shown in Figure 5.3. The natural frequency of the blade is then finally found using equation (5.8) to relate the critical shaft speed to the natural frequency in a stationary reference frame.

6. Diagnostics: Measure damage from natural frequency

The objective of this chapter is to present a diagnostics model that fits into the remaining useful life prediction framework. This diagnostics model uses the natural frequency estimate obtained from BTT to approximate the length of a fatigue crack in a rotor blade. Assumptions are made on the geometry and location of the crack. The crack size and shape are determined from both (i) fatigue crack growth simulations such as those presented by Rege and Lemu (2017) and (ii) measurements of the size of the beach marks from the fracture surface of a blade that already undergone fatigue failure.

In this dissertation an ANSYS SMART (Separating Morphing and Remeshing Technology) crack growth simulation is used to determine the shape of the fatigue crack based on Paris' Law for fatigue crack growth rate. Thereafter a modal analysis is performed on the blade with the different crack sizes to determine the first natural frequency as a function of surface crack length. An inverse model is then constructed to map the natural frequencies to the surface crack lengths. In early implementations of a diagnostics method for determining damage in rotor blades, there is no record of how the crack length relates to the first natural frequency. Thus, in situations like these, a physics-based model must be used to perform diagnosis. Uncertainty is usually large with these models, since there are limited observations of the actual system to validate the physics model. On the other hand, as more diagnostic exercises are performed on the structure, more data becomes available and data-driven models start to generalise the relationship between frequency and crack length. Note that the data of the diagnostics model is only recorded when the crack length is measured in the blade, such as during an NDT inspection.

This chapter proposes a hybrid diagnostics framework that augments the physics-based simulation results with data. The reason for this is (i) to have a model to start with when no measured data is available, and (ii) to incrementally update the physics-based model by introducing data as it becomes available. Therefore, this model can be implemented in early stage diagnostics when data is available albeit limited.

The structure of this chapter is as follows:

1. First, the experimental results are presented for the measurement of the natural frequency from both the modal hammer tests and the BTT tests. These measurements are plotted against the measured surface crack length from the NDT liquid dye penetrant test.
2. A semi-elliptical surface crack is used to approximate the shape of the crack. This shape is determined from finite element fatigue fracture simulations and measurements of microscope images of the fatigue fracture surface.
3. A finite element modal analysis is performed for a blade with varying surface crack lengths. The results are then compared to the collected experimental data.

4. Finally, a hybrid method is proposed for including the finite element results with the data driven results to diagnose a crack length in the rotor blade, based on the measurement of the natural frequency from BTT.

6.1. Fatigue crack growth test results

Ten turbine rotor blades are subjected to fatigue tests on the slip table configuration shown in Figure 3.5. The crack length and natural frequency are periodically measured. Figure 6.1 shows the surface crack length measurement results during the run to failure fatigue lifecycle of the blades. Note that no prior seeding procedures were implemented to initiate the crack in the centre of the blade. Instead the crack is initiated purely from exciting the base of the blade at its natural frequency.

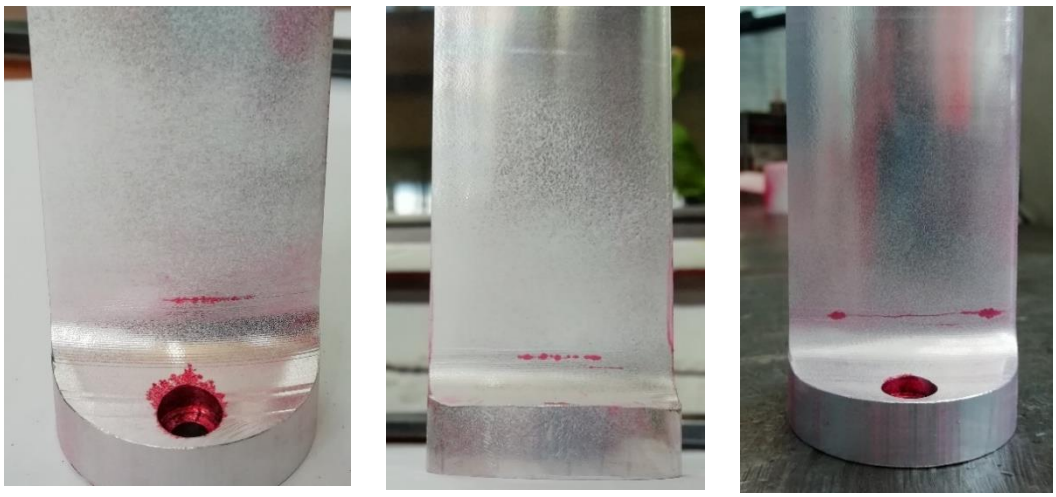

(a) (b) (c)

Figure 6.1: NDT liquid dye penetrant results of crack sizes in rotor blades from (a) early stage, (b) intermediate stage and (c) late stage fatigue.

The first mode natural frequency of the blade is now interpreted as a function of the crack length. Figure 6.2 presents the experimental results from the modal hammer test and the BTT natural frequency estimates. Observe that as the crack grows in the blade the natural frequency decreases in both the modal hammer tests and the BTT measurements. These results align with the observations made in the numerical studies conducted by Chaudhari and Patil (2016) and Elshamy, Crosby and Elhadary (2018) for cracked rectangular cross-sectional cantilever beams. The natural frequency also does not seem to change significantly for small cracks.

Notice that there are fewer BTT measurement data points than modal test data points, especially after reaching a 30 mm crack length. During the experiments it was noticed that a surface crack length longer than 30 mm would have significantly different natural frequencies before and after spinning the blade to perform the BTT measurement due to further crack growth during rotation. This was seen in both the modal hammer test results and the BTT results. Figure 6.3 show the BTT results of the same rotor blade before and after the 30 mm surface crack length. This figure shows that the resonance frequencies

(indicated with a red dashed line) changes during the BTT test. This observation was not made for the same blade while the crack was shorter than 30 mm. BTT tests were therefore neglected for large surface cracks. This also ensures that the blade does not break while performing a BTT test.

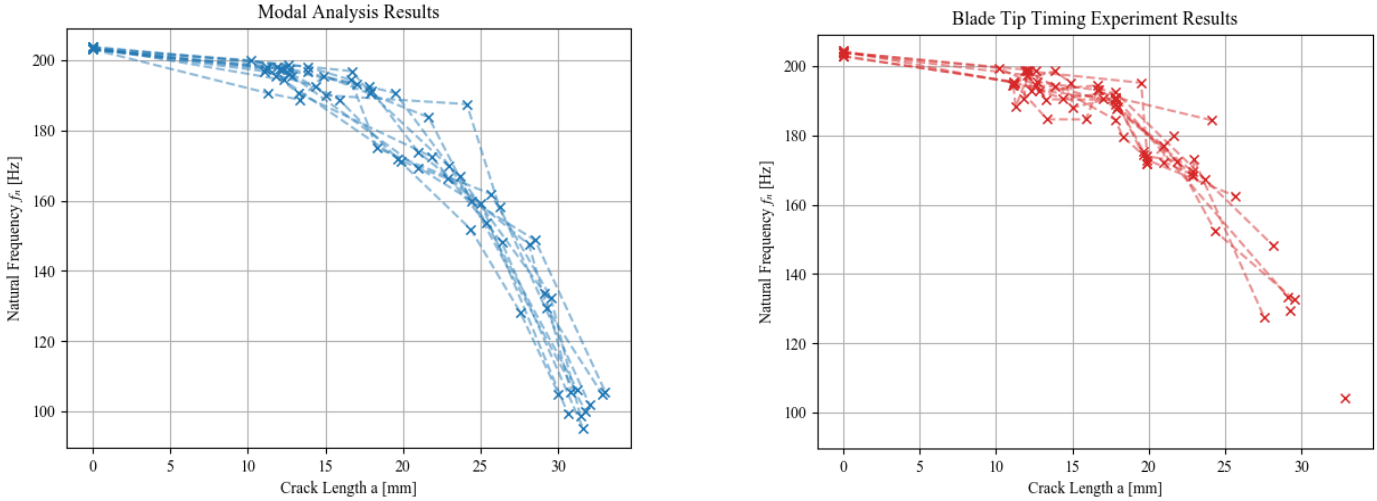

(a) (b)

Figure 6.2: First mode natural frequency of the rotor blade measured from modal impact hammer test (left) and the new BTT method (right).

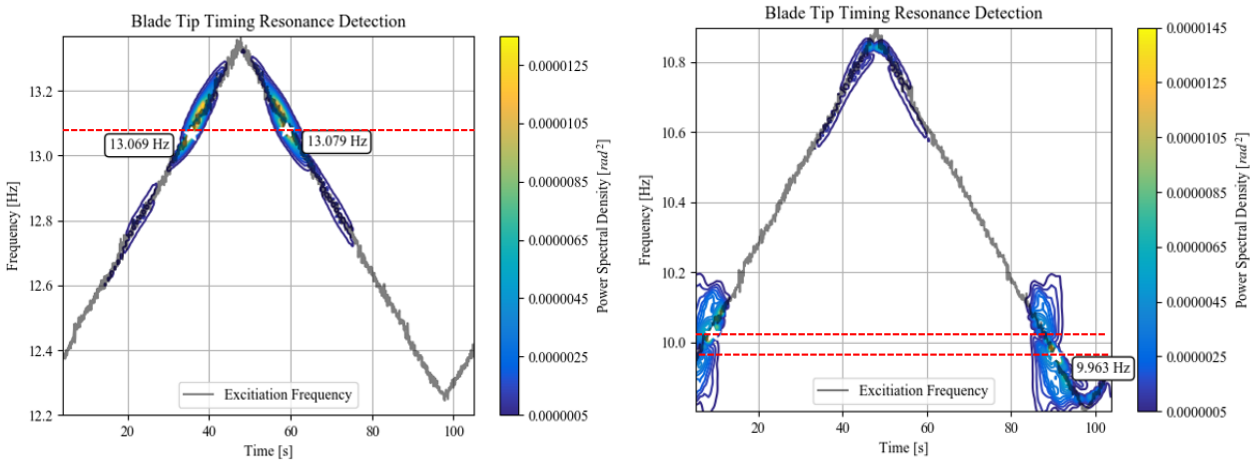

(a) (b)

Figure 6.3: BTT results for a 29 mm surface crack (a) and results for a 33 mm surface crack (b) of the same rotor blade

6.2. Fatigue crack shape and size in a rotor blade

To construct a physics model that relates the natural frequency to crack length it is important to know the shape and depth of the crack. This dissertation assumes a semi-elliptical crack shape only defined by the surface crack length ($2c$) and crack depth (a). Two methods are used to approximate the shape (i) measurements from the fracture surface and (ii) fatigue crack growth simulations using FEM.

6.2.1. Optical microscope images of fracture surface

The fatigue fracture surface of a rotor blade is illustrated in Figure 6.4. The fracture surface is obtained from an optical microscope image of one of the blades used in this experiment. The fracture surface shows fatigue failure with beach marks (shown in red). The depth of the crack is determined by approximating the beach marks as an ellipse centred about the point shown in red. The crack depths (a) and surface crack lengths ($2c$) are measured from the beach marks and are recorded in Figure 6.7.

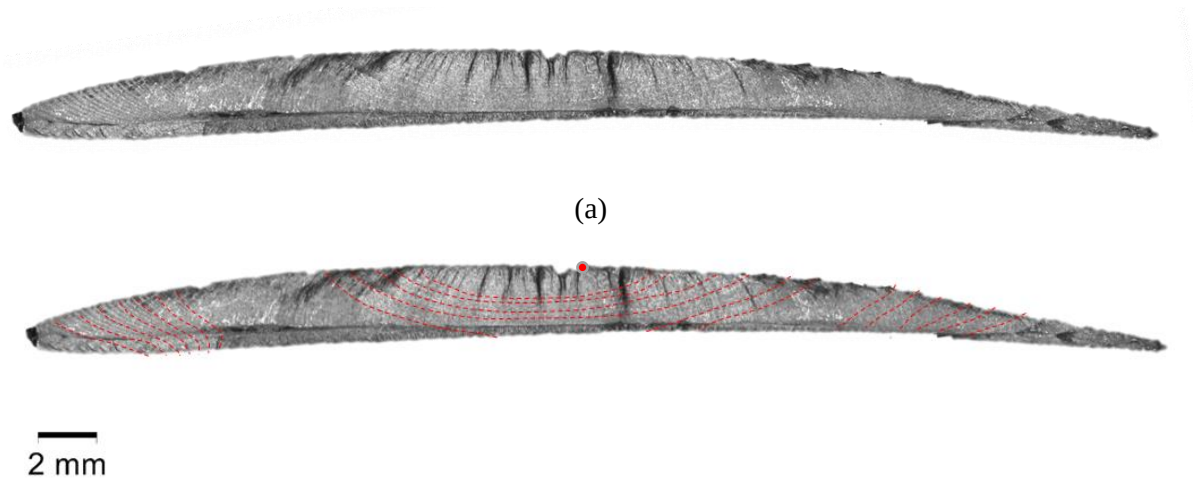

(a)

(b)

Figure 6.4: Optical microscope photos of fracture surface of a rotor blade subject to run to failure fatigue test (a), with marked fatigue beach marks (b).

6.2.2. Finite element method crack growth simulation

The crack shown in Figure 6.1 is also simulated using the finite element method. An ANSYS SMART crack growth simulation was performed on the rotor blade. The simulation requires an initial crack size and propagates the crack by calculating the stress intensity factor along the crack front. The crack front is then propagated according to Paris' Law after a specified number of loading cycles. Thereafter, the blade is remeshed with the new crack length. The initial crack is positioned where the maximum bending stress occurs due to the blade tip being displaced $5mm$ relative to the base of the blade (shown in Figure 6.5).

This simulation requires an initial crack size. A semi-elliptical surface crack length of $2mm$ ($c = 1mm$) and depth of $0.5\ mm$ ($a = 0.5mm$) was selected to start the simulation. This size was selected because it is the smallest possible crack size that avoids ANSYS from defeaturing the small crack during meshing. A fully reversed load is applied to the blade with a $5mm$ blade tip displacement[5]. The

[5] This is the maximum amplitude of the tip displacement used during fatigue testing on the slip table as mentioned in Section 3.2.3

simulation is performed for 40 subsets and a total of 1000 cycles per subset. Figure 6.6 (a) to (c) shows the adaptation of the mesh as the crack grows during the simulation.

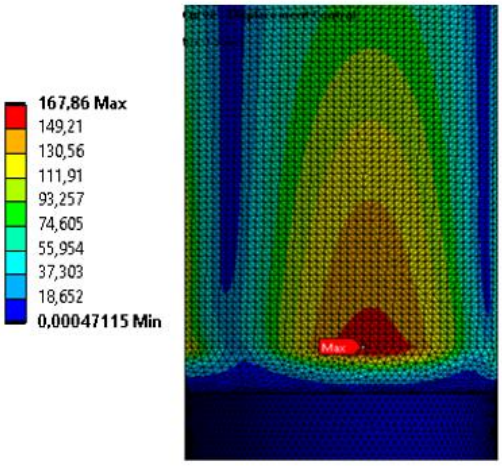

Figure 6.5: Equivalent von-Mises stress of the rotor blade due to 5mm tip displacement and location of maximum stress.

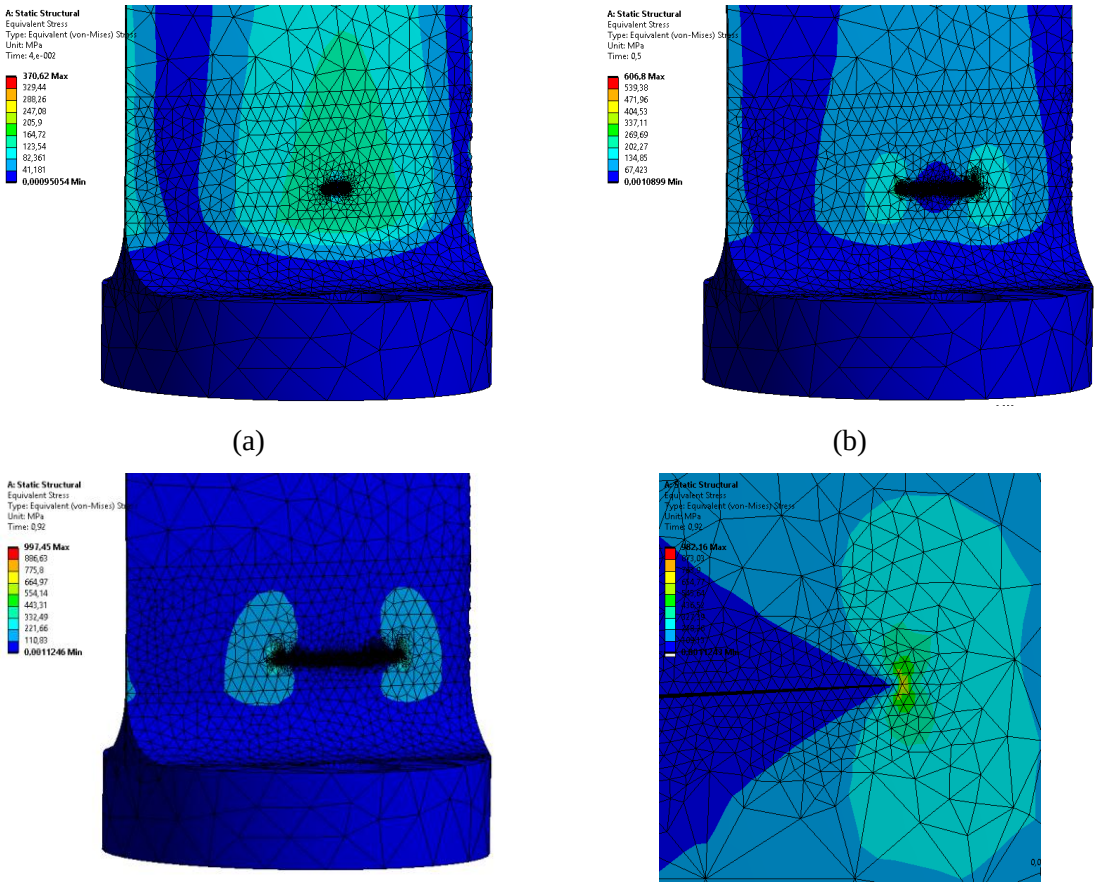

(a) (b)

(c) (d)

Figure 6.6: ANSYS SMART crack growth simulation mesh of (a) the initial crack, (b) a 12mm crack and (c) a 20 mm crack. The equivalent von-Mises stress of the blade at the crack front of Figure 6.6 (d)

The results obtained from these simulations are the crack lengths in the tangential direction (i.e. the depth of the cracks) and the length of the cracks at the surface of the blade. This simulation is repeated until the crack front reaches the other side of the blade. These results have been recorded and are shown in Figure 6.7. Figure 6.6 (d) shows the equivalent von-Mises stress close to the crack front. Notice that the stress diverges at the tip of the crack due to the discontinuous nature of the crack.

6.2.3. Relationship between crack length and crack depth

The results from both the simulation and the optical microscope images are shown in Figure 6.7. A least squares regression model is fit through the data and is shown in equation (6.1).

$$a = 0.0189 + 0.8098 \ln(2c) \tag{6.1}$$

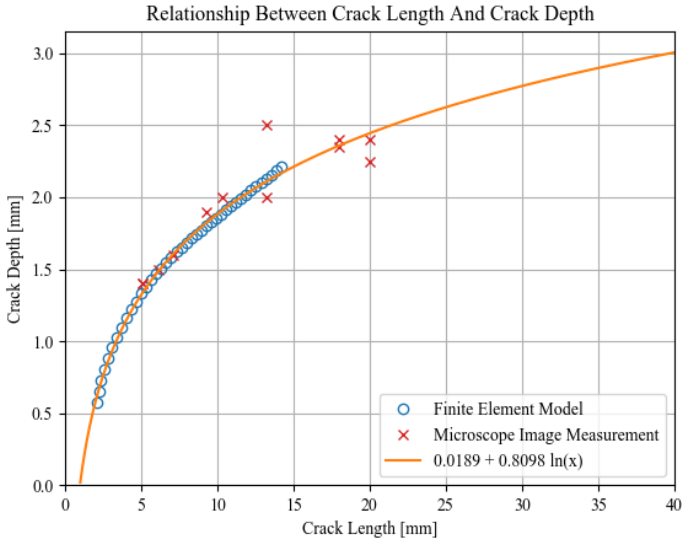

Figure 6.7: Surface crack length and crack depth of a semi-elliptical surface crack approximation from FEM simulation and optical microscope images.

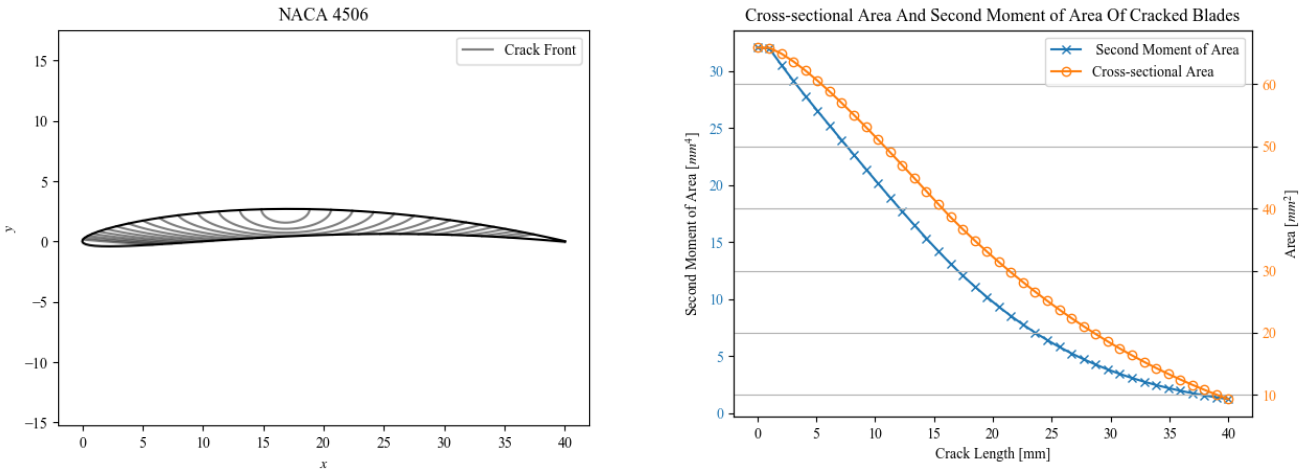

(a) (b)

Figure 6.8: The assumed crack size in the blade (a) from equation (6.1). The cross-sectional area and second moment of area of the blade as a function of crack size (b)

The resulting crack shapes as a function of crack length are shown by the contours in Figure 6.8 (a), the associated cross-sectional area and second moment of area is also calculated as a function of crack length.

6.3. Finite element model for first natural frequencies of cracked rotor blades

Now that the crack depth can be described as a function of crack length the natural frequency of the blade can be determined using FEM. The relationship between crack depth and crack length is necessary for modelling the size of a semi-elliptical surface crack in the blade. The crack is introduced to the blade by splitting the blade at the location of the crack and only sharing the topology between the two parts of the blade that are not part of the crack. This is shown in Figure 6.9 where the pink edges show the shared topology between the bottom and top part of the blade. The reason for this type of model is to introduce the crack to the blade without removing any material from the blade. The modal analysis is performed for different lengths of the crack and the first natural frequency is plotted in Figure 6.10. Figure 6.9 (b) shows the mode shape of a blade without a crack and Figure 6.9 (c) shows the mode shape of the blade with a 33 mm crack. Notice that the mode shape of the blade with a crack is straighter when compared to the blade without a crack.

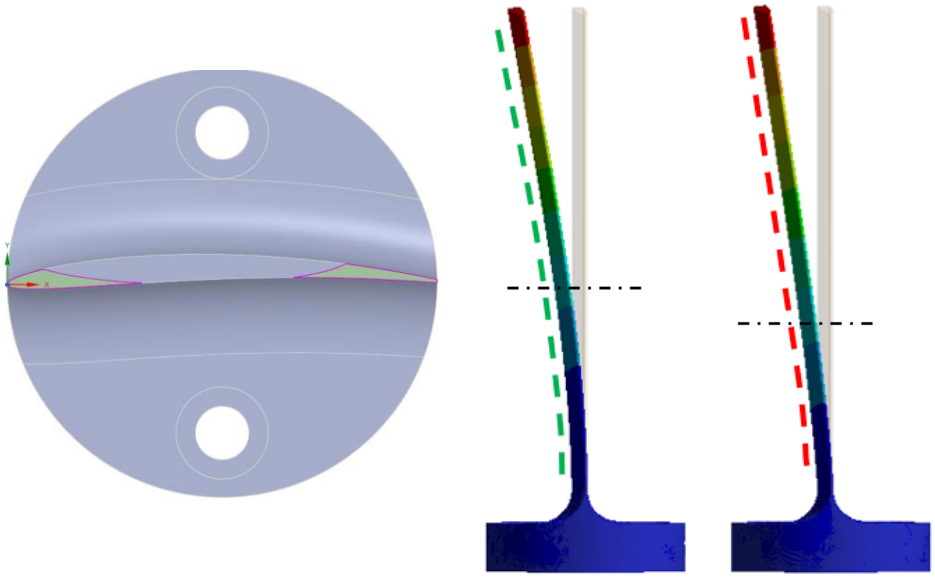

(a) (b) (c)

Figure 6.9: ANSYS shared topology of the top and bottom part of the blade (a) and the associated mode shape for no crack (b) and the largest crack (c).

Figure 6.10 shows the FEM modal analysis results for the blade as a function of crack length. From Figure 6.10 it is seen that the model approximates the data well for small cracks. The deviation in the finite element results seem to indicate an offset in the crack length. The author speculates the reason for this offset is due to plasticity at the crack tip that is not accounted for during the FEM modal analysis.

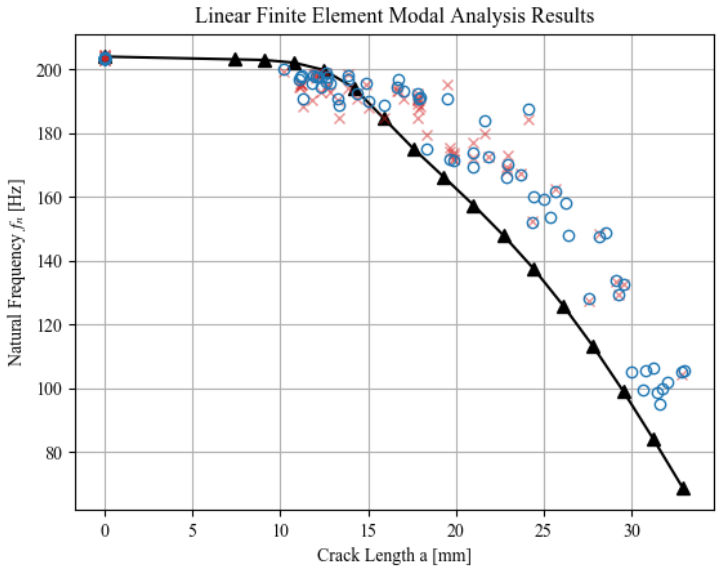

Figure 6.10: Finite element modal analysis results compared to the data collected from the experiments.

6.4. Hybrid method for diagnosing faults from FEM simulations and Data

The goal of this section is to determine the probability density function of the crack length (c) given the natural frequency measured from BTT (f_{BTT}). This probability density function is preferably conditioned on all prior experimental data collected ($\mathcal{D}$) and physics-based models ($\mathcal{M}_{physics}$) chosen to diagnose the rotor blade. That is, obtaining the probability density function in equation (6.2) is the ultimate objective in fault diagnosis using stochastic methods. The data collected is divided into two parts namely (i) the training labels (**y**) and (ii) the training features (**X**). In the case of turbomachine rotor blade diagnostics, the training labels consist of both measured crack lengths (from NDT tests) and the crack lengths specified in the FEM modal analysis. The training features consist of the BTT-measured natural frequencies and the results of the FEM modal analysis.

$$p\left(c\middle|f_{BTT},\mathcal{M}_{physics},\mathcal{D}\right)=p(c|f_{BTT},\mathbf{y},\mathbf{X}) \tag{6.2}$$

In the standard diagnostics approach, most engineers select a model (such as a polynomial) to fit both the experimental data and the finite element simulation results (denoted $\mathcal{M}_{physics}$). The model parameters (denoted **w**), also referred to as the weights of the selected model, is usually solved from a linear least squares regression. However, these least squares regression models maximise the likelihood of obtaining the training data for the selected model (Bishop, 2006). Thus, increasing the complexity of the selected model ($\mathcal{M}_{selected}$) will maximise the likelihood of the data and the model will overfit the data. Thus, the least squares regression models may fail to generalise the diagnosis of a crack with a

few experimental/true measurements of the natural frequency. In early stage diagnosis (when limited data is available) the model will practically always overfit the experimental data. Equation (6.3) shows the maximum likelihood solution to the model parameters ($\mathbf{w}_{\mathrm{ML}}$). Under the assumption that the labels ($\mathbf{y}$) have white Gaussian noise and the selected model is linear in terms of the model parameter, equation (6.4) is the maximum likelihood solution to equation (6.3). The symbol $\boldsymbol{\phi}$ refers to the design matrix and consists of the all the training features substituted into the selected model.

$$\mathbf{w}_{\mathrm{ML}} = \underset{w.r.t\ \mathbf{w}}{\operatorname{argmax}}\, p\left(\mathcal{D}, \mathcal{M}_{physics} \middle| \mathcal{M}_{selected}\right) \tag{6.3}$$

$$\mathbf{w}_{\mathrm{ML}} = \left(\boldsymbol{\phi}^{\mathrm{T}}\boldsymbol{\phi}\right)^{-1}\left(\boldsymbol{\phi}^{\mathrm{T}}\mathbf{y}\right) \tag{6.4}$$

One of the limitations of the maximum likelihood solution is that the model parameters needs to be solved for every new data point. This dissertation, therefore, suggests the use of a Gaussian process regression (GPR) model for diagnostics. One of the advantages of GPR models is that no single model is selected to represent the data. Instead, the GPR model is governed by the choice of a kernel function. A lot of literature shows the use of GPR for generalised models in diagnostics and prognostics (Saha *et al.*, 2010; Corrado *et al.*, 2018). Seeger (2004) provides an in-depth derivation and practical use of GPR models. In summary, these models perform inference to obtain the probability distribution in equation (6.2). Further details on the use of GPR can be found in Seeger (2004). This dissertation uses the built-in packages of Python Scikit-learn to perform GPR.

Consider a blade that has no prior inspection data and only a finite element simulation of the damage in the blade is used to construct the model. The physics-based model is the only information available. However, as data becomes available a hybrid model augments the physics model with the data. Each data point in the diagnostics model consists of measuring the length of a crack and the natural frequency of the blade during stationary conditions. Thus, each data point requires an NDT technique to measure the crack length and a modal impact hammer test or BTT-test to measure the natural frequency of the blade. Collecting data is therefore a longstanding process. This dissertation, therefore, proposes a two GPR models namely (i) a physics-based model and (ii) a hybrid model.

The resulting models and the 95% confidence intervals are shown in Figure 6.11. The figure depicts a model that is trained only on (a) the FEM results (also referred to as the physics-based model) and a model that is trained on (b) both the experiment data and the FEM simulation results. The associated kernel functions and their optimised hyperparameters are reported in equations (6.5) and (6.6) for the physics-based and hybrid approach respectively. The difference between the two models is the inclusion of all the data gathered during the experiments.

$$\kappa_{physics}(x^i, x^j) = ([DotProduct(\sigma_0 = 17.3) + WhiteKernel(\sigma = 0.00412)] \times RBF(l = 5140))^2 + 0.289^2 \quad (6.5)$$

$$\kappa_{hybrid}(x^i, x^j) = ([DotProduct(\sigma_0 = 0.774) + WhiteKernel(\sigma = 0.0884)] \times RBF(l = 432))^2 + 203^2 \quad (6.6)$$

It is noticed that both models encapsulate the FEM results well, however the uncertainty of the physics-based model is less than for the hybrid model. It is, however, emphasised that less uncertainty does not necessarily lead to a better model. The better model is one that predicts the crack length best given all the gathered evidence i.e. the model that is a solution to equation (6.2). Notice that the physics-based model does guarantee that the natural frequency and the crack length of a blade will fit in the 95% confidence interval of the physics-based GPR model.

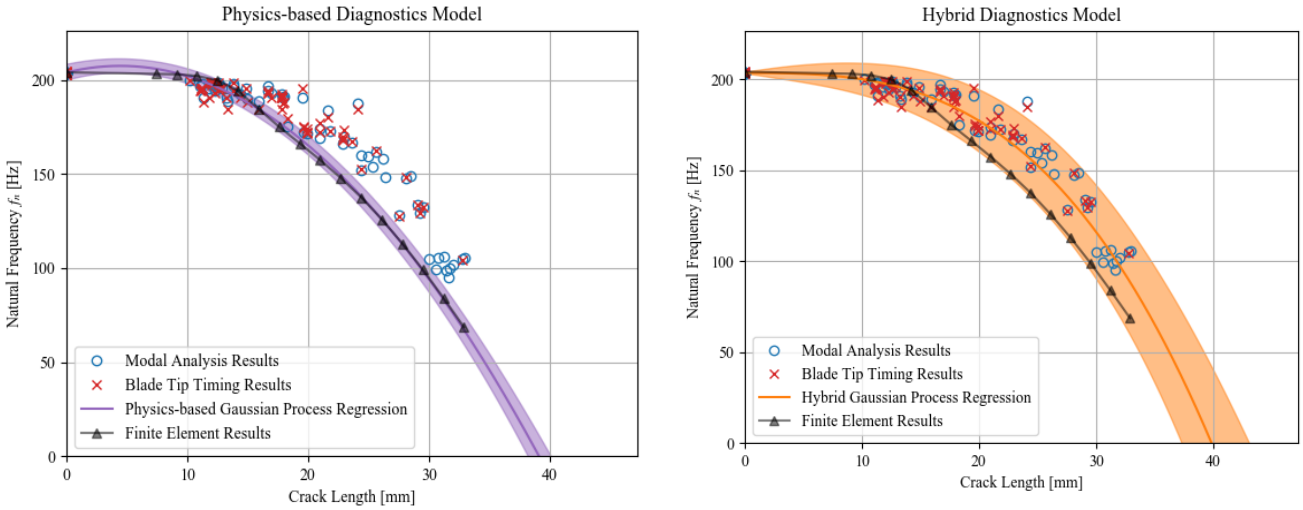

(a) (b)

Figure 6.11: Scikit-learn Gaussian process regression model of only the FEM results (a) and a hybrid between the data and finite element results (b)

Once a lot of data is collected data-driven techniques are applicable and may provide better predictions of the crack length given the natural frequency of the blade. Since GPR constructs models by solving the distribution in equation (6.2) both the data-driven and the physics-based models are applicable. However, since the hybrid model contains evidence collected from FEM simulations and data collected from a limited number of blades. The hybrid method model is therefore considered further in this dissertation, since it contains the most evidence of how natural frequency relates to crack length.

The diagnostics model in Figure 6.11 is constructed such that the model performs estimates of the natural frequency given the crack length. This is because a better GPR model is obtained when the fitting the data to the inverse model. Figure 6.12 orientates the model such that the crack length can be estimated from the natural frequency.

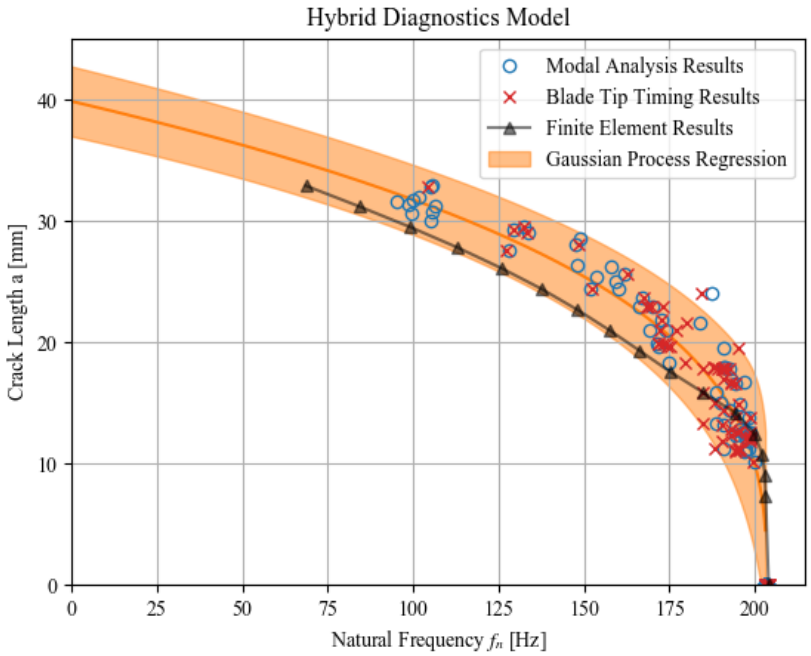

Figure 6.12: Hybrid diagnostics model with natural frequency as independent variable and crack length set to the dependent variable.

7. Prognostics: Estimating RUL

Finally, all the derived models and methods are combined in this chapter to provide a methodology to estimate the RUL. Consider the diagnostics model derived in Chapter 6. This model provides probability distributions of the crack given the measured natural frequency form BTT. Note that once an estimate of the crack size is known the remaining number of fatigue cycles to failure can be determined from Paris' law. Thus, the remaining number of fatigue cycles until failure is calculated using equation (7.1). The Paris' law coefficients, geometric factor, stress range, maximum allowable crack length and the current estimate of the crack length is denoted by C, m, $F(a_k)$, ΔS, a_f and a_k respectively.

$$\Delta N_f = C\left(F(a_k)\Delta S\sqrt{\pi}\right)^m \left(a_f^{\frac{2-\mathrm{m}}{2}} - a_k^{\frac{2-\mathrm{m}}{2}}\right)\left(\frac{2-\mathrm{m}}{2}\right) \tag{7.1}$$

Note, however, that there are the large uncertainties in the crack length obtained from the diagnostics model, the RUL estimation from equation (7.1) becomes very uncertain. This chapter, therefore, suggests the use of a state space model to improve the estimates of current crack length, which will decrease uncertainty in the RUL estimation. Simply put, the model predicts the crack length at the next BTT inspection of the blade. After a diagnosis is made of the blade, the prediction of the crack length is updated using Bayesian inference. The state space model proposed here also includes modelling the Paris' law coefficients as part of the state parameters. Thus, the crack length is treated as uncertain as well as the crack growth rate. This chapter is structured as follows:

1. First, the data collected from the fatigue tests are presented and crack lengths are compared to the number of loading cycles.
2. The next section describes the stresses on the blade during operation and the stress intensity factor at the crack tip as a function of crack length. The Raju-Newman stress intensity factor approximation is then compared to the simulated measurements from the FEM fatigue crack growth simulation.
3. The failure criteria are then discussed for the blade used in this experiment
4. The sequential inference state space model is then provided for the crack and an unscented Kalman filter (UKF) is then suggested to solve the filtering problem. The UKF is a Bayesian inference method that solves posterior distributions of the state given a prediction and an update model. The UKF assumes the state space parameters are sampled from a multivariate Gaussian distribution. The UKF results of one of the blades are discussed and the improvement of the overall RUL prediction is shown for this model. The rest of the results from the UKF is provided in Appendix B.

5. A method is then discussed for improving the approximation of the geometric factor in equation (7.1). This method is implemented in the original UKF state transition equations and the RUL prediction.
6. Finally, the applicability of this method for real time prognosis is discussed and possible limitations of the method are shown.

7.1. Fatigue crack growth experimental results

The fatigue crack growth results obtained from the NDT tests and the electrodynamic shaker are shown in Figure 7.1. The figure shows the measurements from NDT for all 10 blades that where tested. Notice that the figure has a large uncertainty range in the number of cycles as the crack length increases. That is, the crack growth curves become more spread out as the crack grows. This is due to the loading amplitude that changes during the experiment. This is controlled the blade displacement amplitude due to the excitation frequency of the slip table as mentioned in Section 3.2.3.

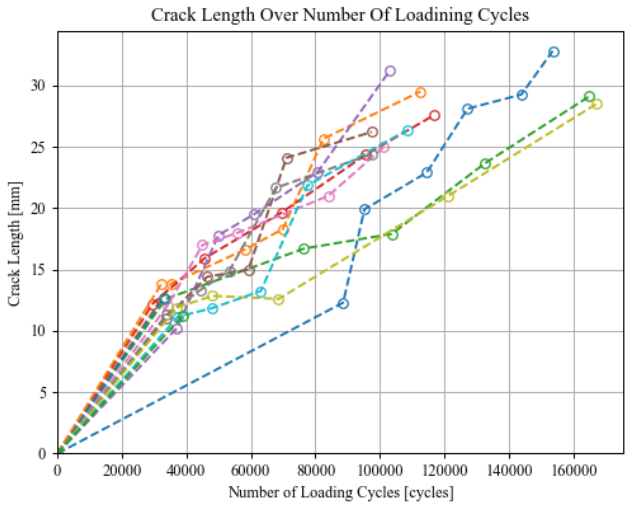

Figure 7.1: Fatigue crack length (measured in NDT tests) compared to the number of loading cycles on the electrodynamic shaker.

Figure 7.2 shows both the expected value from the diagnostics estimate of the crack length and the NDT measurements. The lower graph in the figure is the stress amplitude during the fatigue test. Notice that this stress amplitude is not constant. The reason for this is that the stress is calculated from the displacement of the tip of the blade. However, the displacement of the blade tip varies during the experiment due to the frequency response of the blade changing during degradation. By integrating the velocity response measured by the laser vibrometer it is possible to find the average displacement amplitude. The average stress is then calculated from the average displacement of the blade tip in a finite element solution.

Due to the excitation at the base of the blade, a fully reversed stress is applied during each cycle. Thus, the stress ratio $R = -1$. Corbani *et al.* (2014) investigated the effect of compressive stresses on the

crack growth rate and found no significant increase in the size of the crack front due to compressive stresses. On the other hand, Silva (2005) and Zhang *et al.* (2010) found that residual stresses due to compressive loads cause faster crack growth. However, Zhang *et al.* (2010) suggest an adaptation on Paris' law for negative stress ratios in equation (7.1). The equation only shows that the maximum tensile stress intensity factor is used and the parameter β is only a function of the stress ratio. Therefore, the stress amplitude will only consist of the tensile component on the crack growth rate calculated from equation (7.2) and the compressive stress is neglected.

$$\frac{da}{dN} = C\big((1+\beta)K_{max}\big)^m \tag{7.1}$$

$$\Delta S = S_{max} - S_{min} = S_{max} \tag{7.2}$$

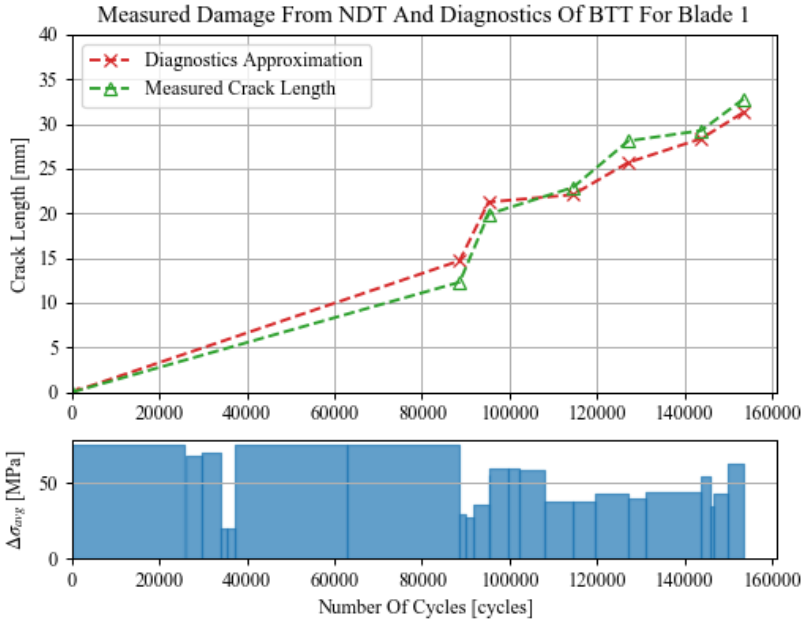

Figure 7.2: NDT crack length measurement and BTT crack length estimation over the number of loading cycles. Additional graph shows the stress amplitude during the fatigue failure test.

7.2. Stresses and future operating conditions

This section describes the computation of the stress intensity factor from two sources. The first approach is to determine the stress intensity factor at the surface from the FEM fatigue fracture simulation in Section 6.2.2. The second approach entails an approximation that assumes a semi-elliptical surface crack in a rectangular cross-section cantilever beam. The size and shape of the crack is already determined in Section 6.2.3. The complex geometry of the blade is approximated by calculating an equivalent thickness of the blade given the with and cross-sectional area. This assumption was used by Witek (2011, 2015) and Brits (2016). Both the finite element method and the approximation method is compared in this section.

7.2.1. Stress intensity factor

The stress intensity factor is calculated for each node on the crack front during the finite element simulation. Figure 7.3 shows solutions to the stress intensity factor as the crack length changes. Each figure shows the crack front and the stress intensity factor solution is shown as a line graph underneath each crack. There are six stress intensity factor contour lines per crack length. Convergence of the solution to the stress intensity factor is verified due to the convergence of the contour lines.

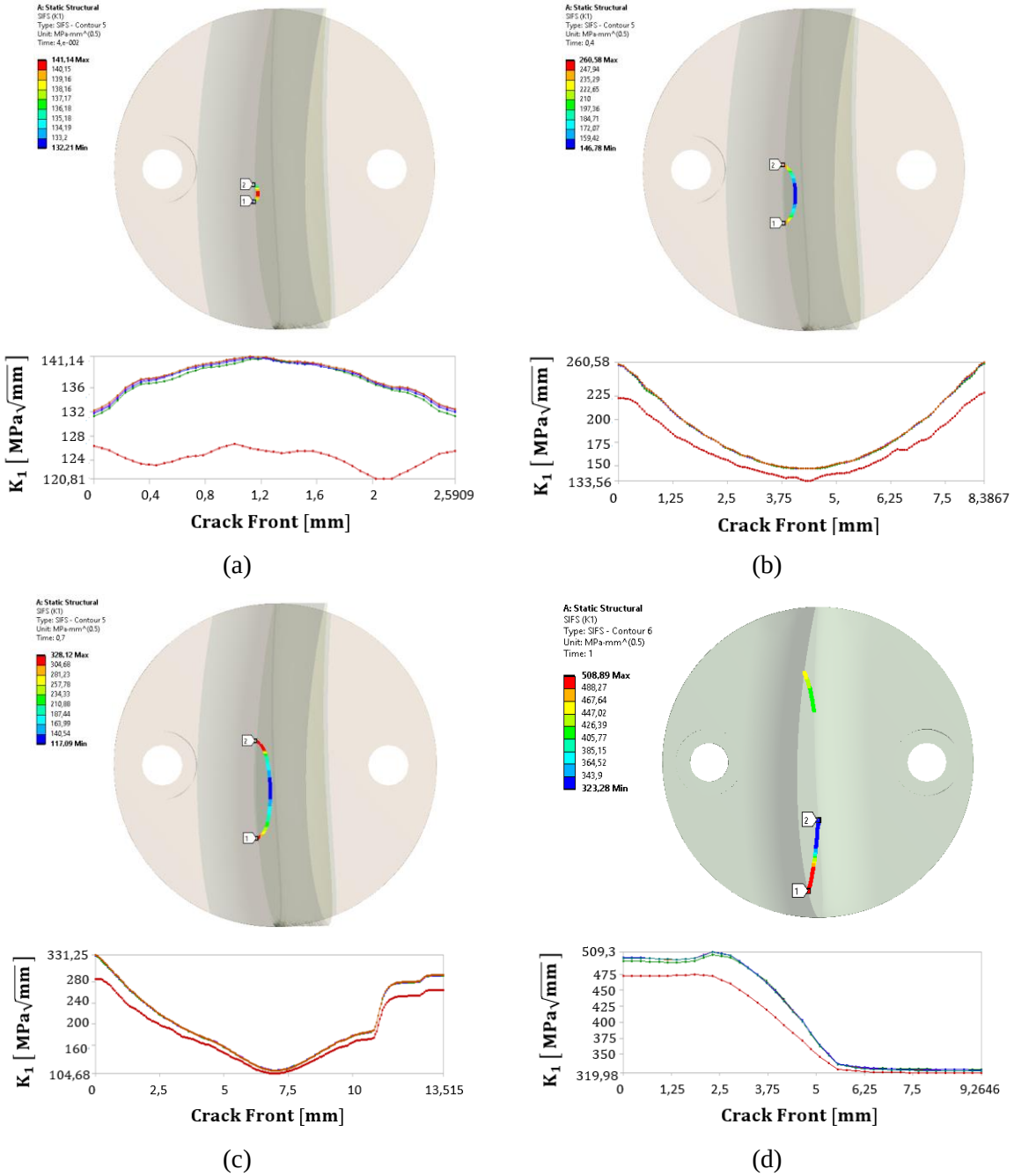

Figure 7.3: Finite element fatigue crack growth simulation stress intensity factor contour results for (a) the initial crack, (b) a small crack, (c) an intermediate crack and (d) a large crack.

The geometric factor at the crack surface is shown as green dots in Figure 7.4. Notice that there are no stress intensity factor values for crack lengths larger than $32\ mm$. This is because the finite element mesh requires very small element sizes to accurately solve the stress intensity factor. Figure 7.4 also shows the evaluation of an equivalent geometric factor, calculated from the Raju-Newman equations in Appendix A. The width of the rectangular section is assumed equal to $2b = 40mm$ and the equivalent thickness is calculated using equation (7.3) from the cross-sectional area $A = 67\ mm^2$. The Raju-Newman equations are only valid for cracks that do not exceed the thickness. Therefore, the graph also shows the part of the Raju-Newman equation that is not valid for cantilever beam approximations.

$$t_{eq} = \frac{A}{2b} \tag{7.3}$$

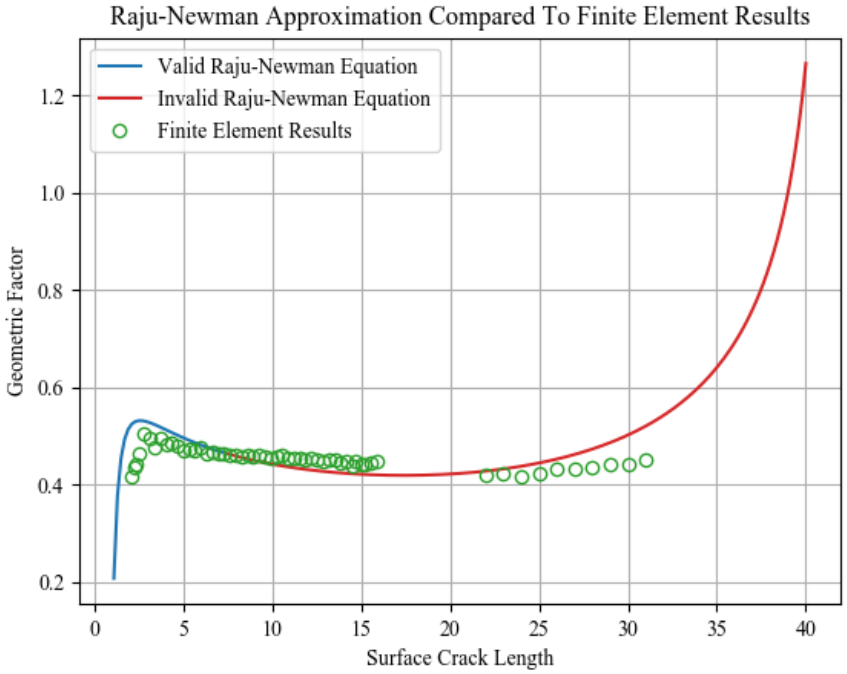

Figure 7.4: Stress intensity factor calculated from Raju-Newman approximation and the finite element simulation of the fatigue crack growth.

The Raju-Newman equations provide a continuous analytical solution to the geometric factor that is close enough to the finite element solutions (within a 10-20% error margin). These equations are therefore used to calculate the stress intensity factor range from the average applied stress.

7.2.2. Failure of the blade under assumed operating stress

Now that the stress intensity factor can be calculated it is important to estimate when failure occurs in the blade. The next figure shows the behaviour of the blade under static loads. The figure shows the applied stress on the y-axis and the crack length on the x-axis. Failure is caused by either yielding or brittle fracture. Yielding happens when the applied stress is larger than the material yield stress, shown by the orange line. Brittle failure, on the other hand, occurs when the stress intensity factor exceeds

fracture toughness ($K_{1c} = 30MPa\sqrt{m}$) of the material. Since the stress intensity function is a function of the crack length, the curve shown in blue is the maximum allowable stress that safeguards against brittle failure. The red dashed line indicates the maximum operating stress and where the red dashed line and the blue line meet is the critical crack length. Brittle fracture will only occur at a crack length larger than $38\,mm$. Thus, the region shown in green is the 'safe' region where failure will not occur due to static loading.

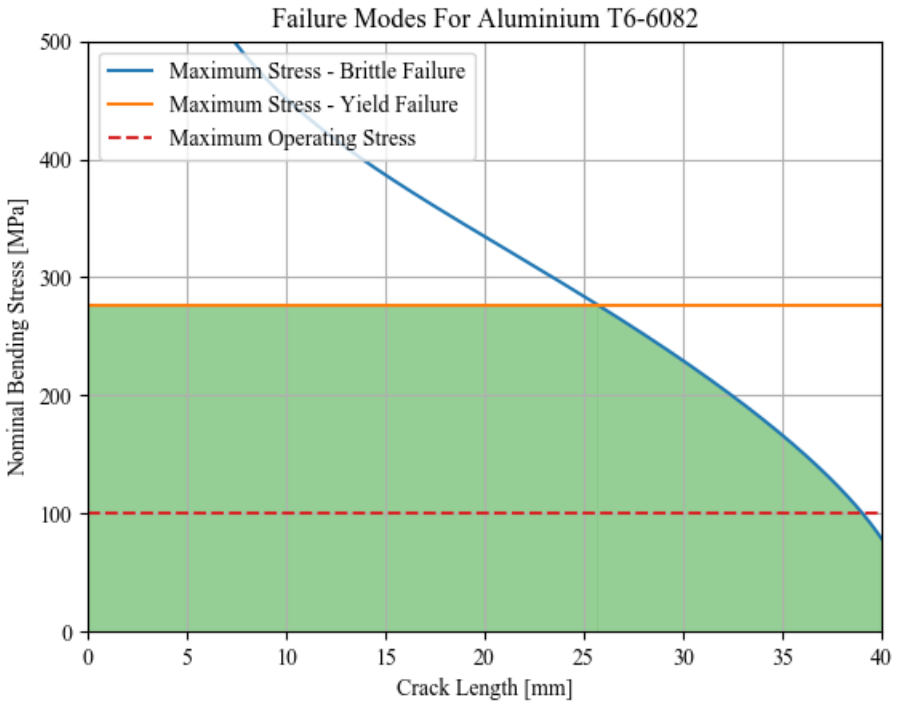

Figure 7.5: Behaviour of Aluminium T6-6082 blade subject to stationary bending loads in the presence of a crack, adapted from Dowling (2013)

In the case of variable stresses, the crack length increases until it reaches the critical crack length. Note from the Figure 7.5 that operating stresses less than $80\ MPa$ have critical crack lengths almost equal to the width of the blade. In these cases, the blade will not experience brittle failure; instead, steady crack growth will occur until the crack is as wide as the blade. Therefore, a maximum allowable crack length is required for the blade. This allowable crack length should be part of the design specification for the blade and the blade should not be used if the crack exceeds the specification.

7.3. Sequential inference model for improved damage estimates

The current damage state of the blade is progressively measured by performing diagnostics on the results obtained from BTT. These measurements are noisy and the blade's crack length is therefore modelled as a probability distribution. This section proposes the state parameters and the equations necessary to perform sequential inference on the probability distribution of the current damage state.

This dissertation proposes the use of the Paris' law coefficients as part of the damage state. Including the uncertainty of Paris' law's coefficients allows for better prediction of future crack lengths, since the probability density function of the current state is not only conditioned on the damage alone but the rate at which damage occurs. The state vector (denoted $\mathbf{x}_k$) is shown in equation (7.3). The Paris' law coefficients and crack length are represented by C_k, m_k and a_k

$$\mathbf{x}_k = \begin{Bmatrix} C_k \\ m_k \\ a_k \end{Bmatrix} \tag{7.3}$$

After several loading cycles the state vector changes according to equation (7.4). The vector function (denoted **f**) is referred to as the transition function.

$$\mathbf{x}_{k+1} = \mathbf{f}(\mathbf{x}_k) = \begin{Bmatrix} C_{k+1} = C_k \\ m_{k+1} = m_k \\ a_{k+1} = f(a_k, C_k, m_k) \end{Bmatrix} \tag{7.4}$$

The equation shows that the Paris' law coefficients do not change after several loading cycles, however the crack becomes longer according to the Paris' law. Equation (7.5) is integrated in equation (7.6) to provide the final transition of the current crack length to the next crack length after the loading cycles have occurred. The result of this integration can be seen in equation (7.7). The parameters ΔS and ΔN are the stress range and number of cycles that elapsed between the transition from $\mathbf{x}_k$ to $\mathbf{x}_{k+1}$.

$$\frac{da}{dN} = C(\Delta K)^m \tag{7.5}$$

$$\int \left(\frac{dN}{da}\right) da = \int \left(\frac{a^{-\frac{m}{2}}}{C\left(F(a)\Delta S\sqrt{\pi}\right)^m} \right) da \tag{7.6}$$

$$a_{k+1} = f(a_k, C_k, m_k) = \left(\Delta N \left(\frac{2}{2-m_k}\right) C_k \left(F(a_k)\Delta S\sqrt{\pi}\right)^{m_k} + a_k^{\frac{2-m_k}{2}} \right)^{\frac{2}{2-m_k}} \tag{7.7}$$

As mentioned earlier the current damage in the blade is continuously monitored though inspections of the blade using BTT measurements. Therefore, it is assumed that state variable a_k is observable. In terms of a sequential inference approach, the measurement function is defined in equation (7.8)

$$\boldsymbol{z}_k = \{a_k\} \tag{7.8}$$

These equations all form part of a hidden Markov chain model. Fracture mechanics theory is used to derive the transition equations; therefore, these equations are physics-based. Equation (7.8) is the measurement function and is calculated from data obtained during diagnostics. Both Kalman filters and particle filters allow for the combination of both the data and the physics-based models to perform inference on the state parameter assuming a hidden Markov chain model.

Equations (7.3), (7.4), (7.7) and (7.8) are implemented in an unscented Kalman filter. The prior probability distribution is defined by the mean vector and covariance matrix in equation (7.9) and (7.10) respectively. The sigma points presented in the work of Julier and Jeffrey (1997) are selected to model the multivariate Gaussian distribution defined by the current state.

$$\boldsymbol{\mu_0} = \begin{Bmatrix} 8.512 \times 10^{-11} \\ 2.7 \\ 10 \end{Bmatrix} \tag{7.9}$$

$$\boldsymbol{\Sigma_0} = \begin{bmatrix} (7 \times 10^{-13})^2 & 0 & 0 \\ 0 & (0.005)^2 & 0 \\ 0 & 0 & (1)^2 \end{bmatrix} \tag{7.10}$$

Figure 7.6 shows the posterior distribution of the UKF given the diagnostics estimates for blade 1. The green dashed line shows measured crack length from the NDT tests and is considered as the "real" crack length of the blade. The red dashed line is the mean of the diagnostics model after the natural frequency of the blade is measured from BTT. The red Gaussian distributions indicate the uncertainty of the diagnostics model. The blue distributions are the UKF posterior distribution after inference is performed on all previous crack length estimations of the diagnostics of the blade.

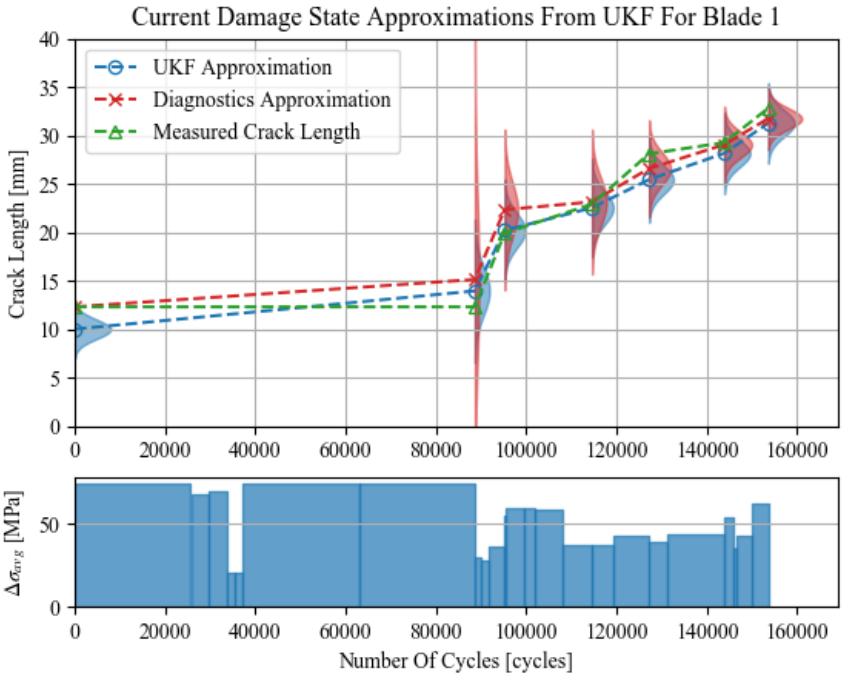

Figure 7.6: Damage state estimation of a single blade with the measured crack length (green), the BTT diagnostics (red) and the UKF results (blue). The stress amplitude during the loading cycles is shown by the lower blue bar graph determined from FEM simulations of the blade's displacement amplitude measured during the fatigue tests.

Notice that the uncertainty of the posterior of the crack length becomes less the more diagnostic estimates are used in the UKF. This is shown in the next figure where the entire Gaussian probability density function is shown for the surface crack length after each update and predict step in the UKF.

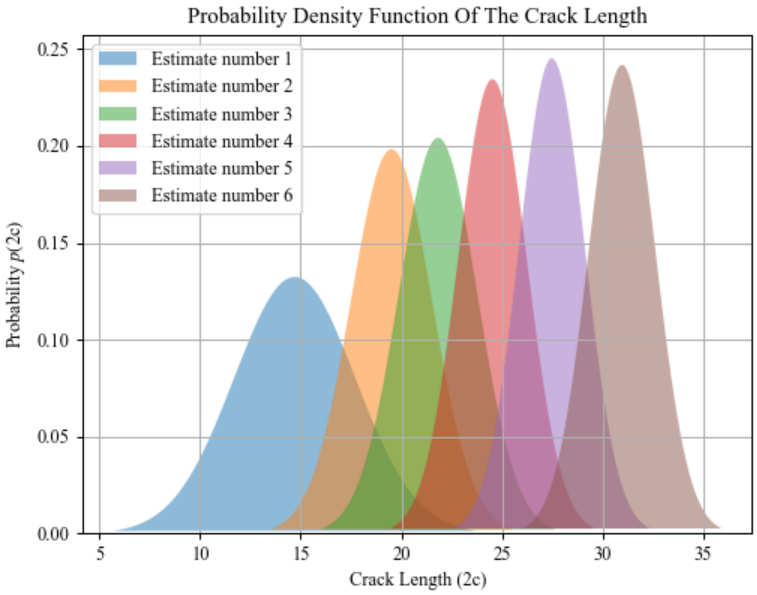

Figure 7.7: The posterior distribution of the current crack length per diagnosis of the blade from BTT.

Figure 7.8 and Figure 7.9 show the probability distributions of the Paris law coefficient and exponent respectively. These distributions indicate that the standard deviation of the parameters increase with each addition of diagnostics information for both coefficients. However, considering the mean value of the Paris Law coefficients shown in Figure 7.10 for the ten blades presented in Section 6.1 it is evident that the parameters change with each diagnostic estimate.

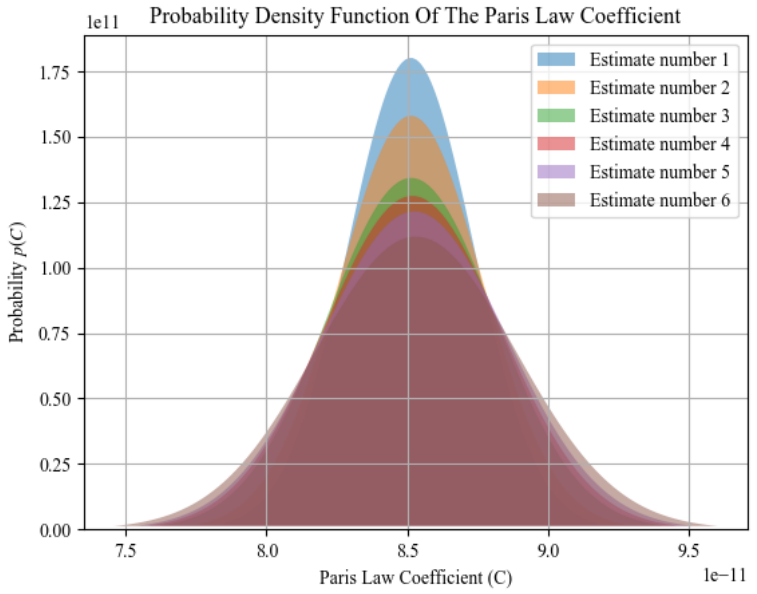

Figure 7.8: The posterior distribution of Paris law coefficient per diagnosis of the blade from BTT.

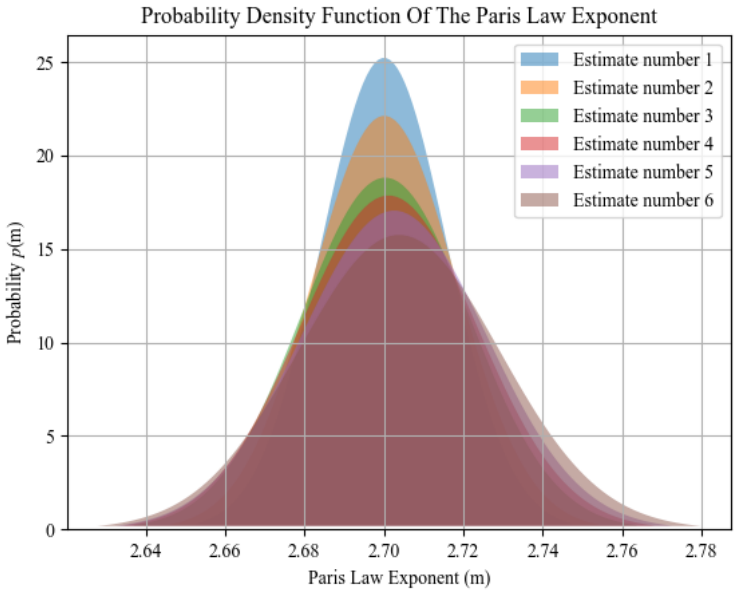

Figure 7.9: The posterior distribution of Paris law exponent per diagnosis of the blade from BTT.

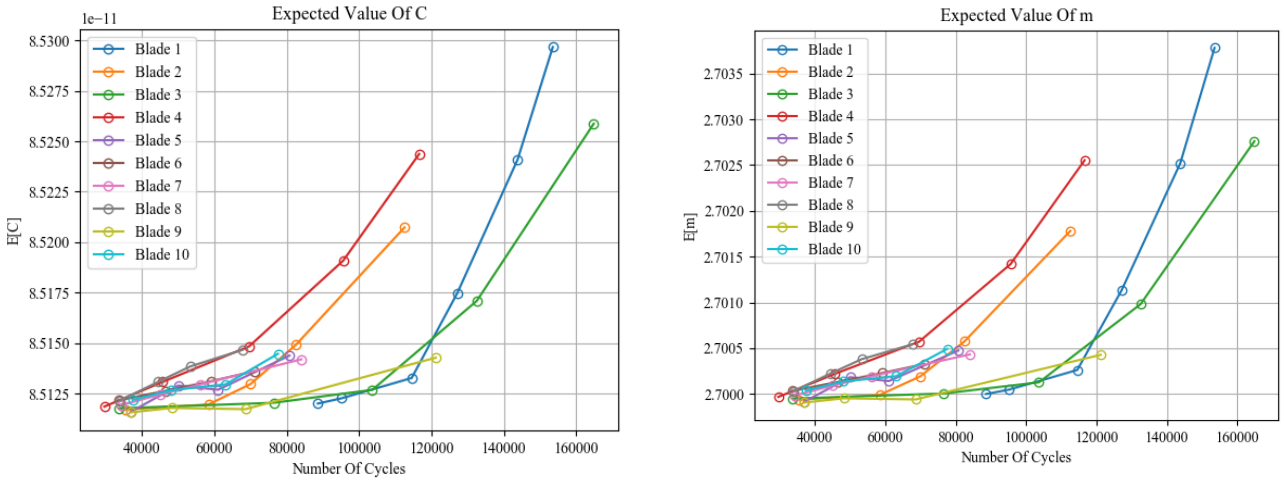

(a) (b)

Figure 7.10: The mean value of the posterior distributions for the Paris Law coefficient (a) and exponent (b) from the UKF for all the blades.

7.4. RUL prediction methodology

Now that a method has been derived to better estimate the current damage state of the blade, it is necessary to predict the remaining number of loading cycles the blade can sustain before reaching the critical crack length or the maximum allowable crack length, denoted a_f. Rearranging equation (7.7) the remaining number of cycles to failure are calculated using equation (7.11) in a deterministic sense.

$$\Delta N_f = C\left(F(a_k)\Delta S\sqrt{\pi}\right)^m \left(a_f^{\frac{2-\mathrm{m}}{2}} - a_k^{\frac{2-\mathrm{m}}{2}}\right)\left(\frac{2-\mathrm{m}}{2}\right) \tag{7.11}$$

The result of the UKF describes a joint probability distribution on the parameters C, m and a. Thus, a deterministic answer for the RUL can be calculated from the mean value of the distribution as shown in equation (7.12). The expected value of multivariate Gaussian distributions is equal to the mean vector of the UKF.

$$\mathbb{E}[\Delta N_f] = \mathbb{E}[\mathrm{C}_k]\left(F(\mathbb{E}[a_\mathrm{k}])\Delta S\sqrt{\pi}\right)^{\mathbb{E}[m_k]}\left(a_f^{\frac{2-\mathbb{E}[m_k]}{2}} - \mathbb{E}[a_\mathrm{k}]^{\frac{2-\mathbb{E}[m_k]}{2}}\right)\left(\frac{2-\mathbb{E}[m_k]}{2}\right) \quad (7.12)$$

7.4.1. Monte Carlo method for RUL estimation

The result in equation (7.12) is only a deterministic estimate of the remaining number of cycles before the crack becomes too long. This estimate is of limited use because the uncertainty of the estimate is not known. An alternative approach to the deterministic estimate is to compute the RUL using a Monte Carlo method. The method approximates the joint probability distribution over C,m and a as a specified number of points. These points are all sampled from the final posterior probability distribution obtained from the UKF as shown in equation (7.13). An estimate of the RUL is then determined from each sample point using equation (7.11). The final RUL probability distribution is then represented by the points, from which a histogram or Kernel Density Estimation (KDE) plot can be created.

$$\boldsymbol{p_{k,i}} = \begin{Bmatrix} C_{k,i} \\ m_{k,i} \\ a_{k,i} \end{Bmatrix} \sim \boldsymbol{\mathcal{N}}(\mathbf{x}_k, \boldsymbol{\Sigma}_k) \quad (7.13)$$

$$\Delta \mathrm{N}_{f,i} = C_{k,i}\left(F(a_{k,i})\Delta S\sqrt{\pi}\right)^{m_{k,i}}\left(a_f^{\frac{2-m_{\mathrm{k,i}}}{2}} - a_{k,i}^{\frac{2-m_{\mathrm{k,i}}}{2}}\right)\left(\frac{2-m_{k,i}}{2}\right) \quad (7.14)$$

The RUL can be determined any time after an estimation is made on the crack length of the blade. Figure 7.11 shows the crack propagation from the posterior distributions of the UKF until the crack reaches the critical crack length equal to $40\ mm$. The top and bottom curves are aligned with the number of loading cycles. These approximations were made by assuming the future operating stress will be $50\ MPa$ continuously until failure. The figure shows how the original uncertainty in UKF is very large at first and with each inference step of the UKF the standard deviation of the RUL decreases. A significant improvement is shown from the estimations of the brown curves compared to blue curves.

The critical crack length also does not need to be the width of the blade. Simply substituting a different threshold value for a_f the estimation will of the number cycles until this threshold is calculated. This is shown in Figure 7.12 where the maximum crack length is set equal to $31\ mm$. This is equal to the last crack length measured during the experiment for blade number one. Considering how the blue histogram compares to the purple histogram in Figure 7.12, it is evident that the method improves the estimations of the crack length and the crack growth rate. To maintain continuity of argument in this dissertation the RUL estimates of the rest of the blades are reported in Appendix B.

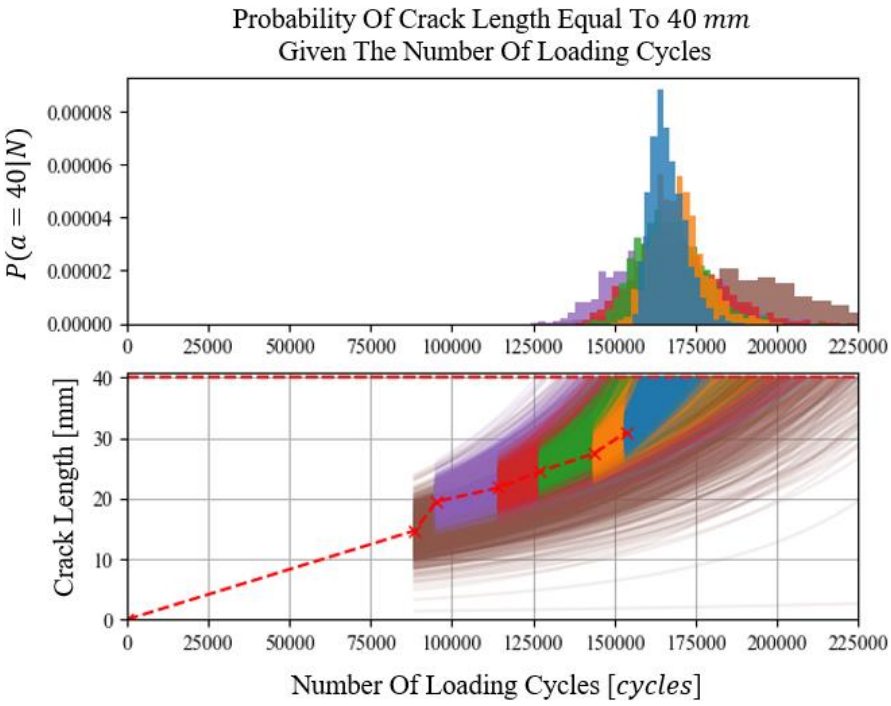

Figure 7.11: Remaining useful life estimation of a blade assuming a constant stress amplitude of 50 MPa. Probabilities of failure at the number of cycles are shown at the top and the Monte Carlo predictions from samples of the UKF are shown below.

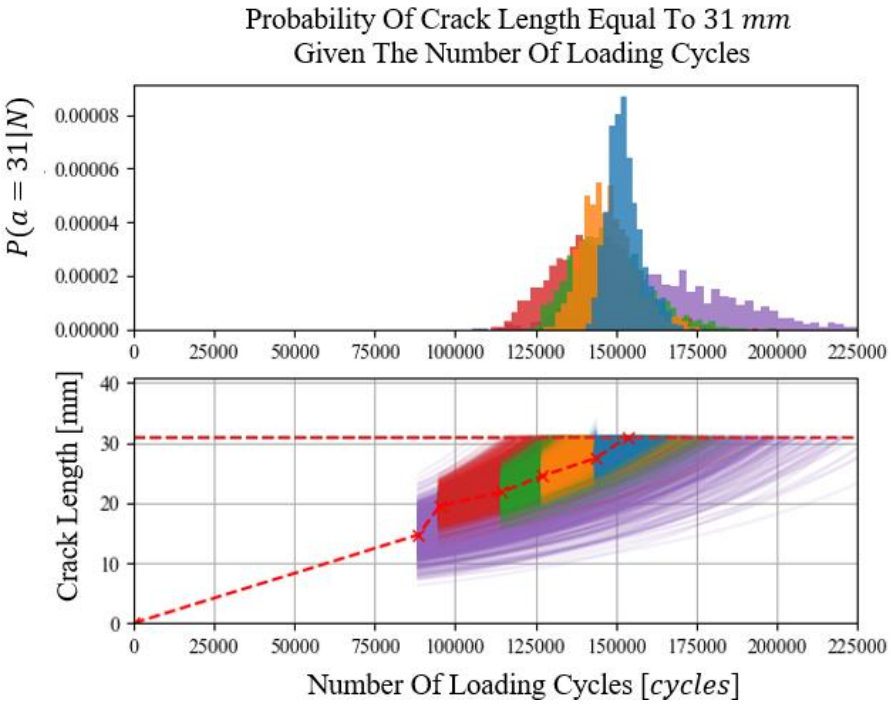

Figure 7.12: Remaining useful life estimation of a blade assuming a constant stress amplitude of 50 MPa. The probability that the crack length equals the maximum specified crack length of 31 mm given the number of cycles is shown in the top graph.

Figure 7.12 shows that the mean value of the RUL probability density function closely approximates the last measured crack length of the rotor blade. The uncertainty of the estimate reduces each time the crack is inspected. It is hypothesised that the uncertainty of the RUL will continually reduce for each inspection of the blade using BTT. The intervals between inspections should initially be as short as possible to decrease the overall uncertainty of the Paris law coefficients and consequently reduce the uncertainty of the RUL. This experiment uses large inspection intervals since the blade is fatigued on the shaker table and tested in the rotor. In industrial applications the fatigue of the rotor blade primarily occurs due to the operating conditions of the turbomachine.

Figure 7.13 shows approximations of the histograms in Figure 7.11 as Gaussian distributions. The figure compares the RUL estimates with the number of cycles until failure. The method should ideally converge to a straight line with a gradient equal to the dashed lines in Figure 7.13. This is because the remaining number of cycles should be used as the fatigue cycles are applied to the blade. The figure shows that the remaining useful life is still updating and the current estimation in the Paris law coefficients have not reached a converged value. Also note from Figure 7.6 the stress amplitude varies during the loading cycles.

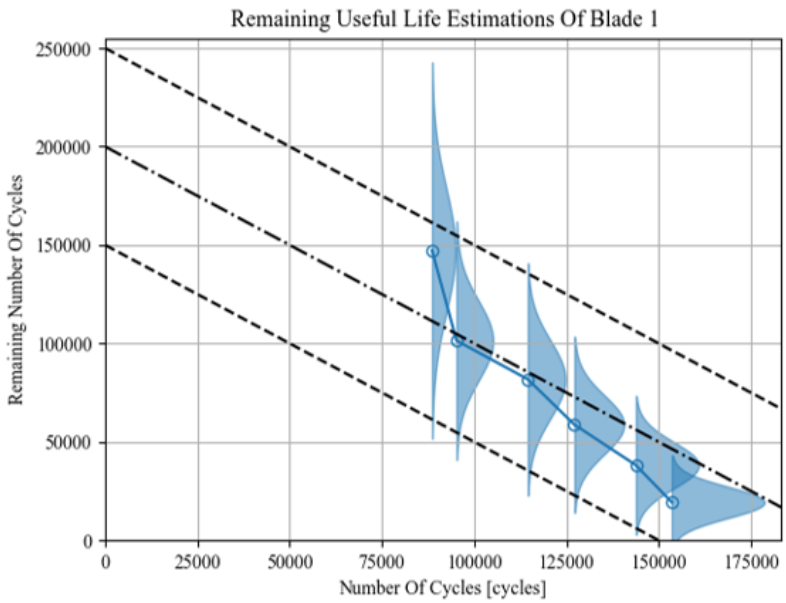

Figure 7.13: Remaining number of cycles estimation as the number of cycles occur.

The same figure is generated and overlayered in Figure 7.14 for all the blades. Figure 7.14 (a) shows the RUL posterior distribution as a function of the number of loading cycles. Note that the stress amplitude changes during the number of cycles due to the shaker table that controls the displacement of the blade during testing. Thus, the loading conditions are different during the number of cycles. Figure 7.14 (b) shows the RUL estimates as the crack length changes for the blade. From this figure it is noticed that the uncertainty in the RUL primarily reduces due to the increase in crack length. Thus, the model only becomes certain of failure when it is close to failure. This makes sense and it is a good

sanity check. The uncertainty of failure is strongly dependent on the length and Paris law coefficients due to equation (7.11). The mean RUL estimation for all the blades are shown to be a function of the crack length. However, the uncertainty reduces as the crack length increases. The reduced uncertainty is primarily due to the crack growth rate becoming unstable and brittle failure is imminent. Thus, the predicted RUL is low for large cracks and the uncertainty of failure decreases. Future work will look at the effect of modelling Paris law coefficients as part of the state space parameters and the overall prediction accuracy.

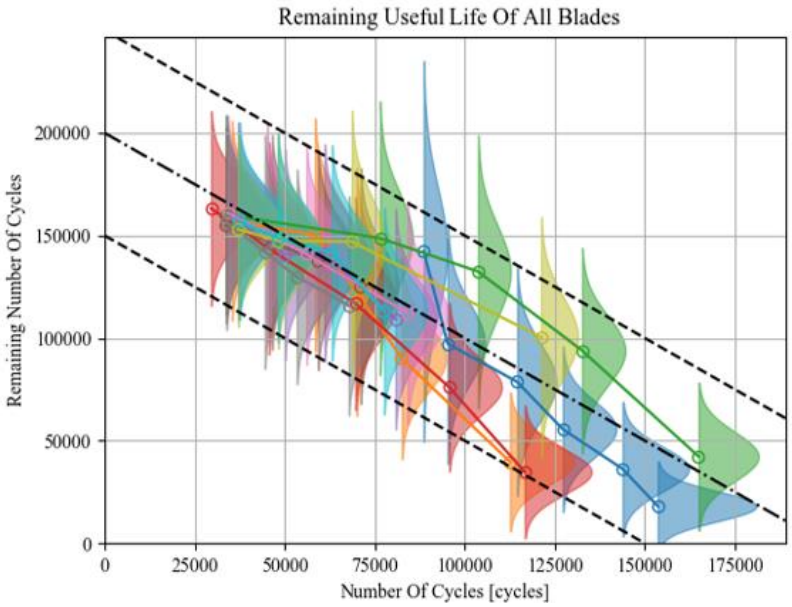

(a)

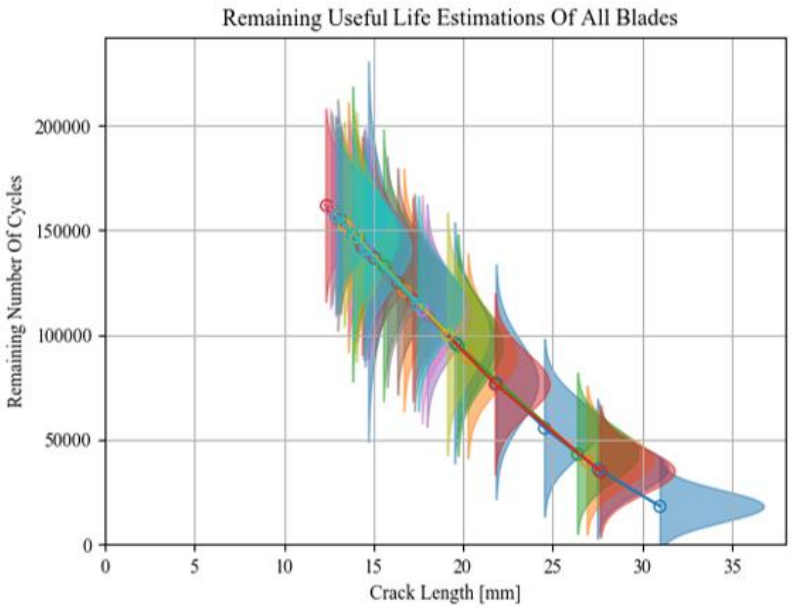

(b)

Figure 7.14: RUL estimation until the crack equals $40mm$ with a $50\ MPa$ average stress is obtained in for all experiments compared to the number of cycles (a) and the estimated current crack length (b).

7.5. Improved integration of Paris' Law for state estimation and RUL estimation

Consider the geometric factor in equation (7.5). During the integration of equation (7.4) this factor is assumed constant for each step in the UKF. This assumption is only valid when the geometric factor does not change significantly during a loading cycle. Figure 7.4 showed that the geometric factor changes for different crack lengths. An improved model to estimate of the crack propagation should solve the crack length intermediately by transitioning the crack length only for a small number of cycles (denoted Δn). The new crack length is then transitioned continuously for this small number of cycles until the summation of all the Δn transitions is equal to the specified ΔN. Equation (7.15) shows the intermediate transition function. Equation (7.12) shows that the final transition is a composite function of each small transition.

$$f(C_k, m_k, a_k, \Delta n) = \left(\Delta n \left(\frac{2}{2-m_k}\right) C_k \left(F(a_k)\Delta S\sqrt{\pi}\right)^{m_k} + a_k^{\frac{2-m_k}{2}}\right)^{\frac{2}{2-m_k}} \tag{7.15}$$

$$a_{k+1} = f(C_k, m_k, f(C_k, m_k, f(\dots), \Delta n), \Delta n) \tag{7.16}$$

This method ensures an accurate approximation to the transition function. The more intermediate the crack lengths are available, the closer the approximations become to the analytical integral of equation (7.6). This method was implemented in the UKF state estimation shown in Figure 7.6 and Appendix B.

The geometric factor also does not remain constant in equation (7.7) when estimating the remaining number of cycles to failure. A similar incremental method is applied to this equation however small increments are made on the crack length. The number of cycles is then determined from a summation of all the cycles required to propagate the crack from its current state to the specified final state.

$$\Delta n_i = g(C, m, a_i, a_{i-1}) = C\left(F(a_i)\Delta S\sqrt{\pi}\right)^m \left(a_i^{\frac{2-m}{2}} - a_{i-1}^{\frac{2-m}{2}}\right)\left(\frac{2-m}{2}\right) \tag{7.17}$$

$$\Delta N_f = \sum_{i=k+1}^{f} \Delta n_i \tag{7.18}$$

7.6. Comparison of hybrid prognostics models

The derived prognostics model is compared to existing techniques. This section compares the model to three types of existing models namely (i) a deterministic model based only on physics-based methods and observations from BTT, (ii) a hybrid prognostics model with a physics-based diagnostics model and (iii) a hybrid prognostic model based only on the crack length (that is a model that excludes the Paris law coefficients from the hidden state variable).

7.6.1. Deterministic estimation from physics-based models

The RUL of the one the blades is determined using a deterministic technique from integrating Paris' law. The result is shown in Figure 7.15. The bottom graph shows the crack length estimated from BTT (blue) at the number of loading cycles referenced to the start of the experiment. The true crack length measurements are shown in green. At each of the diagnostics stages (that is at each estimation of the crack length shown in blue) the number of cycles is predicted until the crack reaches a length of $31\ mm$. The mean of the Paris law coefficients is used to calculate the remaining number of cycles from the crack length estimated at each stage. The top graph shows the number of cycles that is required from the start of the experiment for the crack length to equal $31\ mm$. It is assumed that the blade exceeds its specification limit when the number of cycles exceeds the indicated amount (vertical coloured bar).

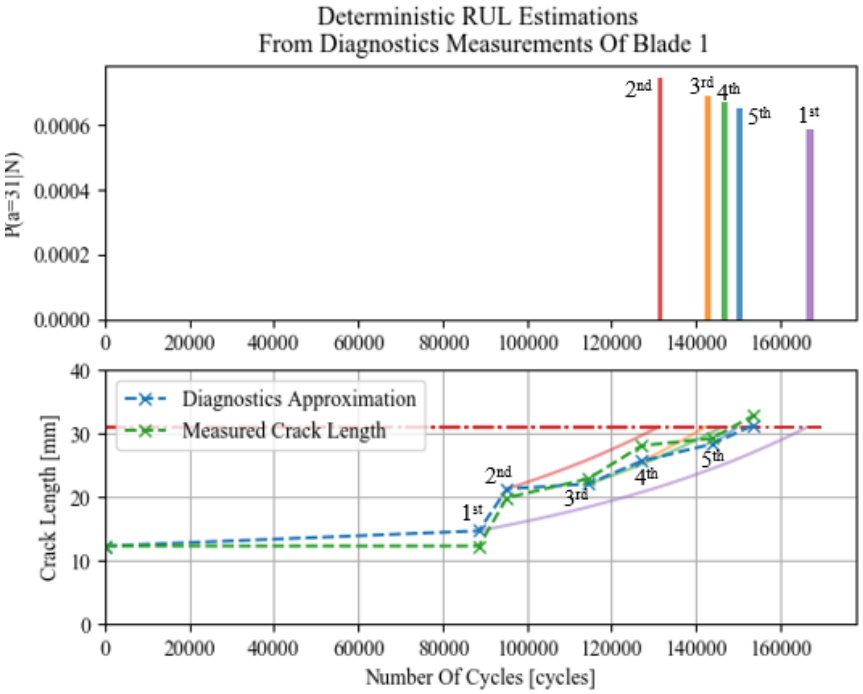

Figure 7.15: Deterministic estimations of the number of loading cycles to failure determined from the mean of the crack length obtained from the diagnostics model.

Notice that each number of cycles estimation (from the deterministic model) is different for each diagnosis of the blade. That is, at each of the numbered points on the lower graph has a different RUL

estimation shown in the top graph. Therefore, the result in Figure 7.15 does not provide enough information for decision making since the estimations are inconsistent. There are also no uncertainty bounds resulting from the method which makes it difficult for engineers to determine the associated risk of keeping the blade in operation. The advantage of the proposed method in section 7.4 is that the result is a probability density function with uncertainty bounds that become smaller with each estimation as shown in Figure 7.12.

7.6.2. Regular physics-based diagnostics

Figure 7.16 demonstrates the method for crack length estimations made from the purely physics-based diagnostics method. The figure shows each crack length estimation with Gaussian probability density functions shown in red. The uncertainty in the probability distribution is very narrow since only FEM is used to diagnose the crack length. The UKF results from the observed diagnostics is show in blue. Comparing Figure 7.16 to Figure 7.6, it is evident that the physics-based diagnostics method (i.e. Figure 7.16) fails to estimate the measured crack length (green points) as accurate as the hybrid method.

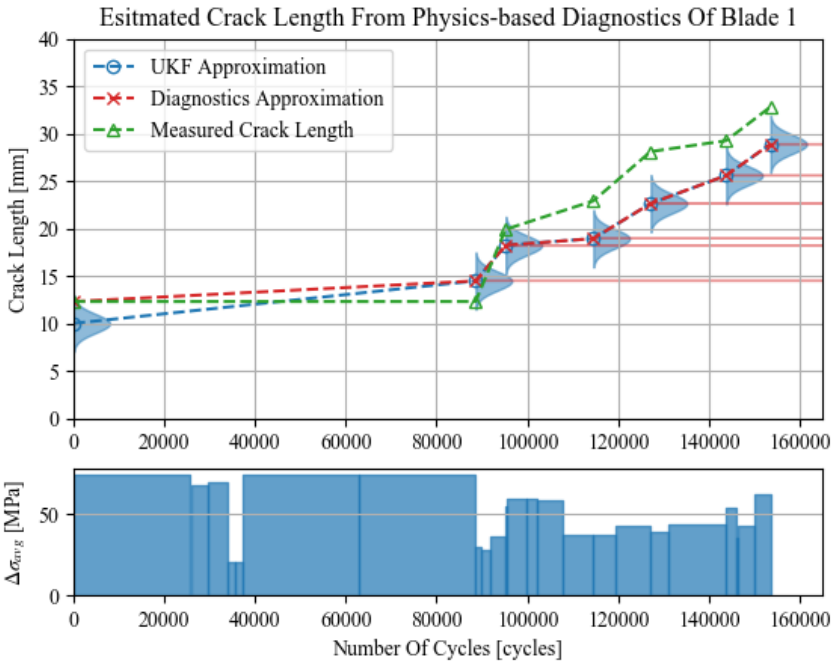

Figure 7.16: Damage state estimation of a single blade with the measured crack length (green), the BTT physics-based diagnostics (red) and the UKF results (blue). The stress amplitude during the loading cycles is shown by the lower blue bar graph.

Figure 7.17 shows how the Paris law parameters changes with each diagnosis. The final estimations of the remaining number of cycles is shown in Figure 7.18. These results are comparable to the results in Figure 7.12 since the same algorithm is used to predict the RUL from the current damage estimate. The only difference between the two models is that the model in Figure 7.12 uses a hybrid diagnostics method whereas Figure 7.18 uses a model constructed only on FEM results.

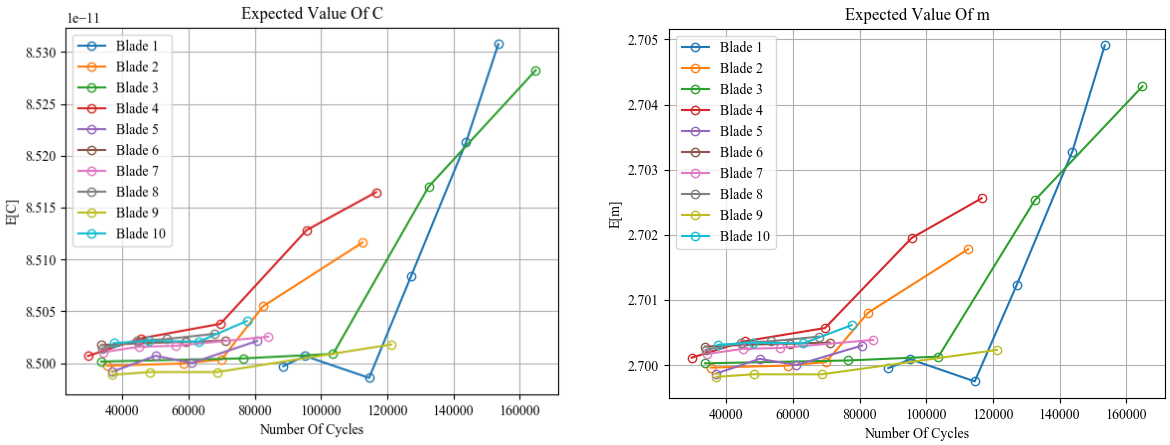

(a) (b)

Figure 7.17: The mean value of the posterior distributions for the Paris Law coefficient (a) and exponent (b) from the UKF of the physics-based diagnostics for all the blades.

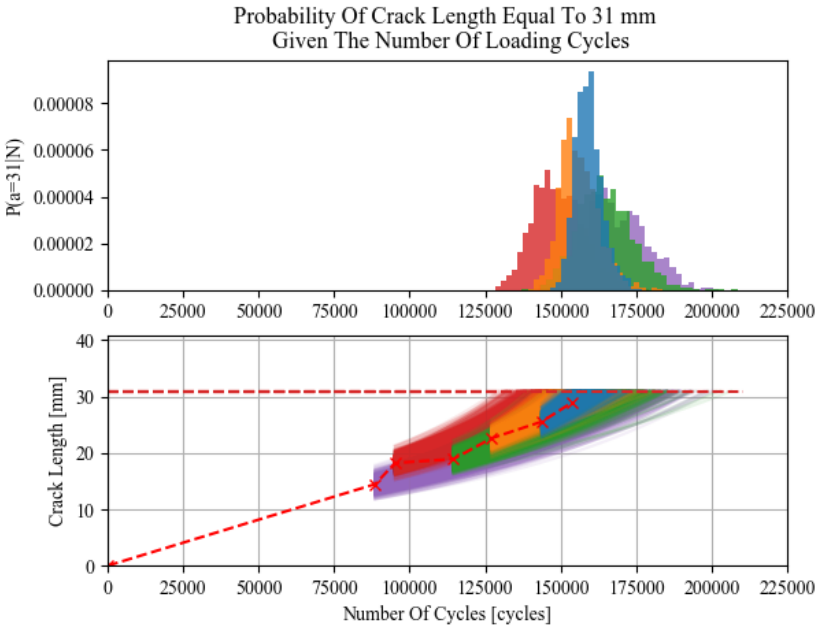

Figure 7.18: Remaining useful life estimation of a blade using a physics-based diagnostics method. Assuming a constant stress amplitude of 50 MPa. The probability that the crack length equals the maximum specified crack length of 31 mm given the number of cycles is shown in the top graph.

7.6.3. UKF estimation of only crack length as hidden state

The final model to consider is a UKF that treats the crack length only as the hidden state parameter. The Paris law parameters are assumed constant in this model. The estimations of the crack length are made from the hybrid diagnostics model and the result is shown in Figure 7.19. The results show that the UKF does not approximate both the diagnostics and the measured crack lengths as effectively as the model in Figure 7.6. This is because the Paris law parameters are fixed. Thus, errors are made in the prediction step of the UKF. The update step in the UKF accounts for the difference between the

diagnostics approximations and these predictions. The RUL estimations for this model is shown in Figure 7.20. The model has comparable results to the model in Figure 7.12 and is commonly used by most crack length prediction prognostics methods.

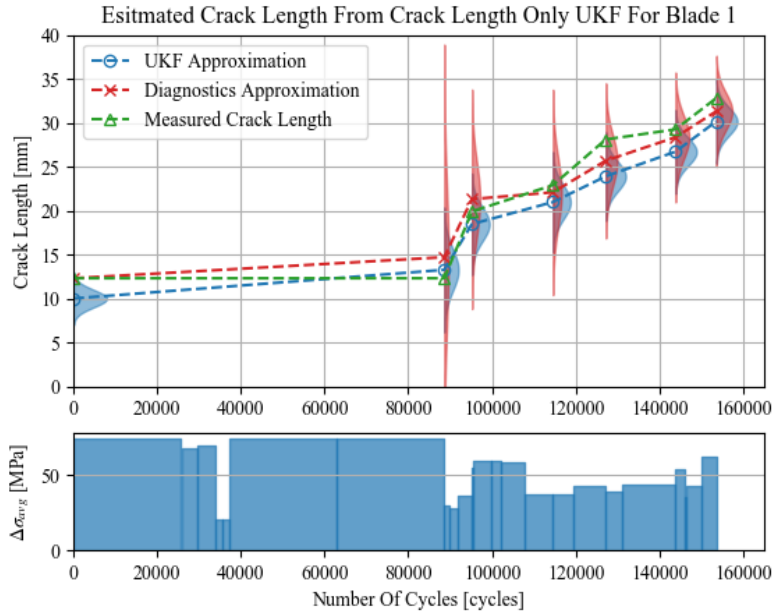

Figure 7.19: Damage state estimation of a single blade with the measured crack length (green), the BTT diagnostics (red) and the crack length based UKF results (blue). The stress amplitude during the loading cycles is shown by the lower blue bar graph.

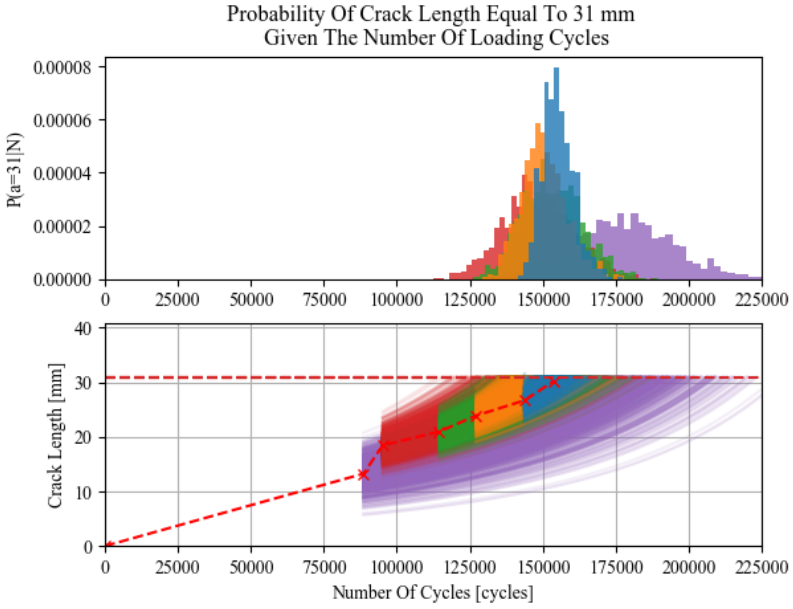

Figure 7.20: Remaining useful life estimation of a blade assuming a constant stress amplitude of 50 MPa. The probability that the crack length equals the maximum specified crack length of 31 mm given the number of cycles is shown in the top graph.

7.7. Limitations and applicability for real-time prognostics of rotor blades

This final section discusses some of the limitations this method has for real time applications on rotor blades.

First and foremost, the UKF works by approximating Gaussian probability density functions which are continuous over an entire real domain of the state vector. The UKF will for certain priors predict crack lengths larger than the length of the blade when using equation (7.7). This is problematic since the stress intensity factor is not defined for cracks that are longer than the blade itself. These problems primarily occur if the prior probability distributions are not selected correctly. It is necessary to investigate the choice of proper priors in equation (7.13), however this is not part of the scope of this dissertation. Instead, the methodology was provided for estimating RUL from BTT data. Future work should consider the effect of prior mean vector and covariance matrices.

Secondly, the estimation of the RUL is a probability of failure curve. The expected value or mean of this probability density function is not a good estimate of when the component will fail since there is a 50% chance that the blade will fail before the cycles are completed. Rather, it is recommended that the probability of failure is selected based on risk assessment.

Lastly, these estimations in RUL all have Gaussian shapes due to the way the UKF models the inference problem. Other non-Gaussian probability density functions could have been investigated to see if the RUL estimate remains Gaussian. However, Coppe *et al.* (2010, 2012) used a particle filter-based approach to approximate the RUL of the various plates. These predictions showed that the RUL remained near Gaussian.

8. Conclusion

This dissertation presents four key contributions to the field of prognostics and health management.

The *first* contribution is a novel method for analysing BTT signals to determine the response of the tip of the blade. The method is derived from dynamics principles and makes no assumptions about the acceleration of the rotor shaft. The method also allows the user to determine the relative angular displacement of the blade tip by treating each proximity probe individually (instead of collectively). Therefore, knowledge about the radial location of each proximity probe is not necessary to determine the blade response.

The *second* contribution is the derivation of a technique that determines the critical speed of a rotor blade from a newly derived least squares spectral analysis method. The method detects the critical speeds of the rotor from the measured response of the blade. The significance of this work is that it allows the user to perform spectral analysis on data that is unequally sampled in time. The newly derived method finds its origin with the Lomb-Scargle periodogram. VanderPlas (2018) showed that since the Lomb-Scargle periodogram is a least-squares fit between unequally sampled data, there might not exist a Nyquist frequency limit for this technique. Regardless, this method is only tested for a single transient run-up run-down load case for the rotor. The method is successful in approximating the critical speeds and using a Campbell diagram to obtain the natural frequency of blade in real-time. The resulting measured natural frequencies are within a $5\ Hz$ error margin from the natural frequencies measured with modal impact hammer tests. The approximation method accounts for centrifugal stiffening in the blade due to centrifugal acceleration force experienced by the blade.

The *third* contribution is a hybrid model that estimates the uncertainty of the crack length in a rotor blade from the measured BTT results. The GPR model uses both results from a FEM modal analysis and the experimental data to perform inference on the current crack length given the measured natural frequency from BTT tests. FEM fatigue fracture simulations and optical microscope images of the fracture surface confirm the shape of a typical fatigue crack that initiates at the location of maximum bending stress in the blade. In early stage diagnostics, when limited data is available for determining damage of the blade, a physics model is the only available model for estimating crack length from natural frequency. However, as data becomes available hybrid techniques allow for in inclusion data collected from NDT tests. The GPR method also fits in the proposed prognostics framework of this dissertation.

The *final* contribution of this dissertation is the use of the diagnostic estimates to improve fatigue crack growth models. The method proposed here estimates the remaining useful life by setting up a state space model for improving the uncertainty in the Paris Law coefficients and ultimately the estimation of the RUL.

In conclusion this dissertation is summarised in Figure 8.1 and Figure 8.2. First the procedure starts with a BTT signal. The signal is then processed to obtain the natural frequency of the blade. The current crack length in the blade is determined from a pre-constructed diagnostics model that provides uncertainty estimates of the damage in the blade based on the current natural frequency of the blade. The condition of the blade is continually monitored, and a state space model improves the current estimate of the crack length by performing Bayesian inference given all the prior diagnostics information. The final probability density function of the RUL estimate is obtained by propagating the crack length until it reaches the maximum allowable crack length. The success of the proposed methodology is demonstrated, and it is proven that the RUL can be estimated from a BTT condition monitoring signal.

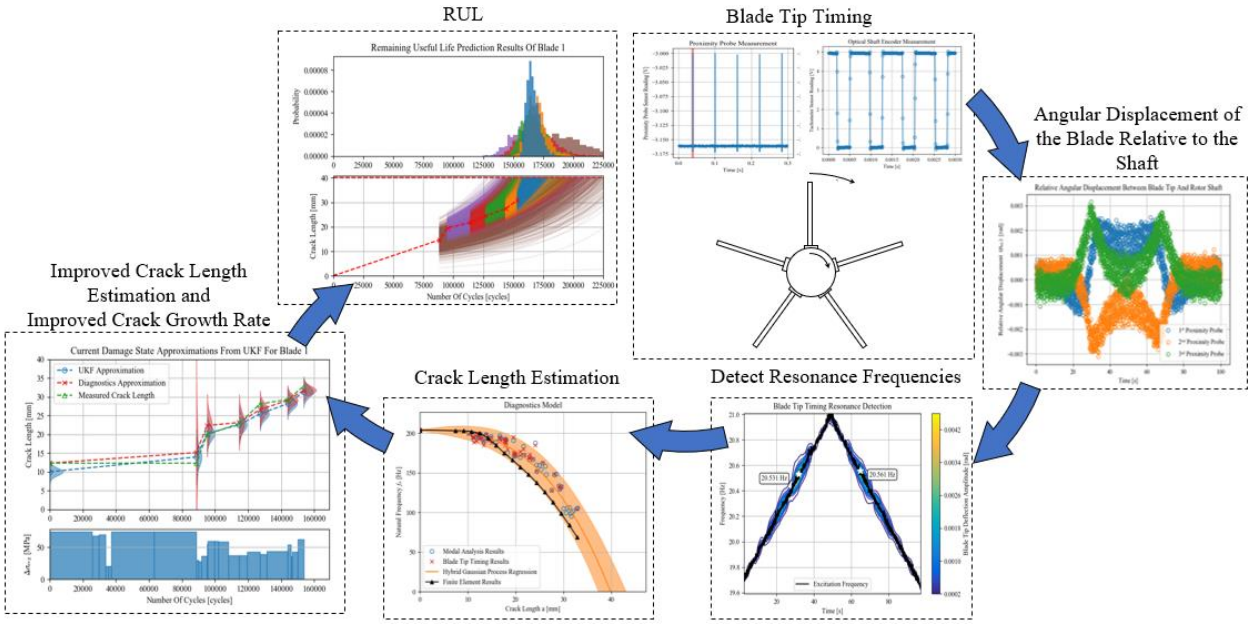

Figure 8.1: Prognostics framework for determining the RUL of a rotor blade in real time using BTT as a condition monitoring method.

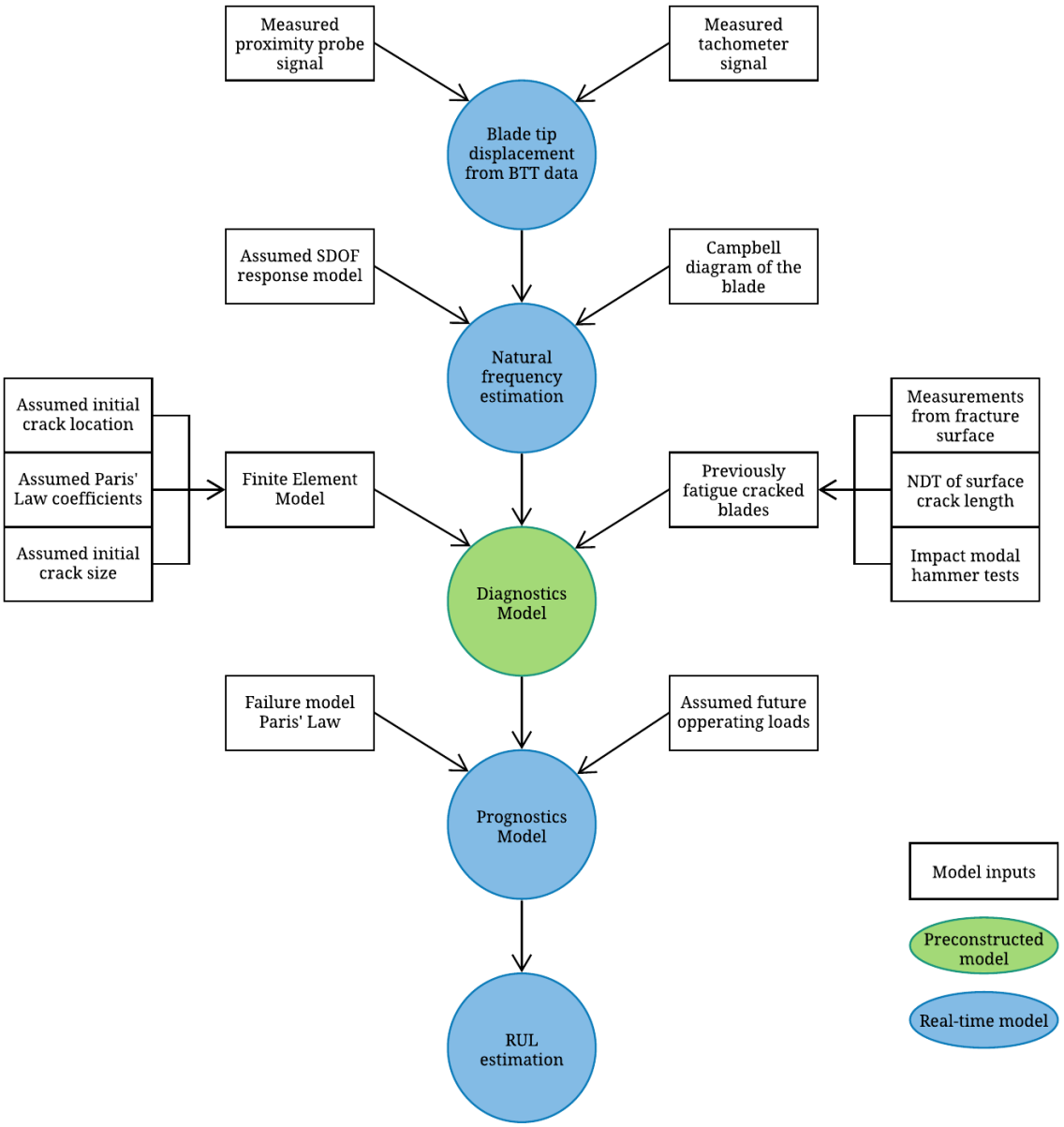

Figure 8.2: Real-time diagnostics and prognostics framework and its required information to construct the models.

9. Future work

This dissertation proposes a complete real-time hybrid prognosis of a turbine rotor blade. The intention of this work is to estimate remaining useful life of these rotor blades from newly derived methods and methods found in literature. Naturally, not all diagnostics and prognostics methods have been considered and future work could see the inclusion of many different methods. This section outlines some of the future work that can be pursued from this work. These topics pertain to the practical application and the generalisation of the proposed techniques.

1. The newly derived BTT signal processing method is shown to work for a run-up run-down transient load case. This is a specific type of transient load case. Other types of transient loads may cause the measurement of the blade tip displacement or estimations of the natural frequency to be inaccurate.
    - A confirmation of the true relative blade tip displacement compared to the signal processing measurements is therefore necessary. That is, the measurements from BTT (calculated from the method proposed in Section 4.2) need to be compared to other measurements such as strain gauge measurements to ensure that the technique determines the true relative displacement of the blade.
2. The new least squares spectral analysis method also only confirms the measurement of the natural frequency of the blade in an experiment with a single blade and a single air nozzle. Admittedly, this is not representative of the true loads in a turbine rotor.
    - Therefore, future work should look at the effect of multiple blades and multiple air nozzles on the accuracy of the technique. These other types of conditions should ideally emulate the loads of a real turbomachine rotor blade setup.
3. The diagnostics of the blade makes assumptions of the location and shape of a single crack in the blade. This assumption is restrictive in the sense that a blade may contain cracks at other locations and may have multiple cracks. Most of the current research shows methods for detecting multiple cracks and crack sizes (Corrado *et al.*, 2018).
    - The application of techniques for detecting and measuring multiple cracks could improve the overall estimation of the RUL using the proposed methodology with multiple crack lengths as the state parameters.
4. The hybrid diagnostics model suggested in Section 6.4 is compared to the physics-based model. The selection of a hybrid method is purely based on the model that uses all sources of available information.
    - The limitation of the hybrid method is that the model is constructed from FEM simulations and measured data that is hard to come by. The method requires measurements of the crack length in the blade (typically obtained from NDT tests) and

natural frequency measurements. This data can be obtained beforehand by performing experiments such as the experiments proposed in this dissertation or by intermittently stopping the operation of the turbomachine to perform NDT tests.

5. The state space model proposed in the prognostics section is not completely validated and it is difficult to prove whether this model is better than only tracking the crack length in the blade.
    - Methods for tracking the crack length as the hidden state variable are shown to improve the overall estimation of the RUL of the component. However, adding the Paris law coefficients to the hidden state vector does not show significant improvement for the limited number of diagnostics estimates performed in the experiment. Future endeavours will look at proving the improvement of including these parameters in the state space model. Various methods have been proposed for evaluating the performance of a prognostics algorithm (Saxena *et al.*, 2008; Kai Goebel *et al.*, 2011; Ramasso *et al.*, 2016). These metrics could be used validate the suggested approach.
6. The proposed state space model only considers linear elastic fracture mechanics. The effect of plasticity and crack initiation is overseen in this dissertation.
    - Future work should also look at the models that include the NASGRO equation for nonzero stress ratios.
7. The effect of multiple degradation models such a wear and creep are not considered in this dissertation, however the inclusion of these method will likely have the same type of transition and measurement functions.
8. Other real time condition monitoring techniques have not been considered. However, due to the hybrid nature of the suggested prognostics methodology, these techniques should be easy to implement. Future work should confirm the use of multiple condition indicators to estimate the remaining number of cycles.

References

An, D., Kim, N. H. and Choi, J. H. (2015) 'Practical options for selecting data-driven or physics-based prognostics algorithms with reviews', *Reliability Engineering and System Safety*. Elsevier, 133, pp. 223–236.

Anger, C., Schrader, R. and Klingauf, U. (2012) 'Unscented Kalman Filter with Gaussian Process Degradation Model for Bearing Fault Prognosis', *European Conference of the Prognostics and Health Management Society*, pp. 1–12.

Baraldi, P., Cadini, F., Mangili, F. and Zio, E. (2013) 'Prognostics under different available information', *Chemical Engineering Transactions*, 33, pp. 163–168.

Baraldi, P., Mangili, F. and Zio, E. (2012) 'A Kalman filter-based ensemble approach with application to turbine creep prognostics', *IEEE Transactions on Reliability*. IEEE, 61(4), pp. 966–977.

Bishop, C. M. (2006) *Pattern recognition and machine learning*. Springer.

Brits, J. C. P. (2016) *An Experimental and Stochastic Approach to Estimate the Fatigue Crack Life of a Turbomachinery Blade using Finite Element Modelling Master of Mechanical Engineering*. University of Pretoria.

Candy, J. V. (2006) *Bayesian signal processing : Classical, Modern, and Particle filtering methods*.

Carden, E. P. and Fanning, P. (2004) 'Vibration Based Condition Monitoring: A Review', 3(4), pp. 355–377.

Chaudhari, J. R. and Patil, C. R. (2016) 'Study of Static and Modal Analysis of Un-Crack and Crack Cantilever Beam using FEA', *International Journal of Engineering Research and Technology (IJERT)*, 5(4), pp. 534–542.

Chen, J., Yuan, S., Qiu, L., Wang, H. and Yang, W. (2018) 'On-line prognosis of fatigue crack propagation based on Gaussian weight-mixture proposal particle filter', *Ultrasonics*, 82, pp. 134–144.

Coppe, A., Haftka, R. T., Kim, N. H. and Yuan, F. G. (2010) 'Uncertainty reduction of damage growth properties using structural health monitoring', *Journal of Aircraft*, 47(6), pp. 2030–2038.

Coppe, A., Pais, M. J., Haftka, R. T. and Kim, N. H. (2012) 'Using a simple crack growth model in predicting remaining useful life', *Journal of Aircraft*, 49(6), pp. 1965–1973.

Corbani, S., Martha, L. F., de Castro, J. T., Carter, B. and Ingraffea, A. (2014) 'Crack Front Shapes and Stress Intensity Factors in Plates under a Pure Bending Loading that Induces Partial Closure of the Crack Faces', *Procedia Materials Science*, 3(December), pp. 1279–1284.

Corbetta, M., Saxena, A., Giglio, M. and Goebel, K. (2017) 'An investigation of strain energy release rate models for real-time prognosis of fiber-reinforced laminates', *Composite Structures*, 165, pp. 99–114.

Corbetta, M., Sbarufatti, C., Giglio, M., Saxena, A. and Goebel, K. (2018) 'A Bayesian framework for fatigue life prediction of composite laminates under co-existing matrix cracks and delamination', *Composite Structures*. Elsevier, 187, pp. 58–70.

Corrado, N., Durrande, N., Gherlone, M., Hensman, J., Mattone, M. and Surace, C. (2018) 'Single and multiple crack localization in beam-like structures using a Gaussian process regression approach', *JVC/Journal of Vibration and Control*, 24(18), pp. 4160–4175.

Correia, J. A. F. O., De Jesus, A. M. P., Alves, A. S. F., Lesiuk, G., Tavares, P. J. S. and Moreira, P. M. G. P. (2016) 'Fatigue crack growth behaviour of the 6082-T6 aluminium using CT specimens with distinct notches', *Procedia Structural Integrity*. Elsevier B.V., 2, pp. 3272–3279.

Cubillo, A., Perinpanayagam, S. and Esperon-Miguez, M. (2016) 'A review of physics-based models in prognostics: Application to gears and bearings of rotating machinery', *Advances in Mechanical Engineering*, 8(8), pp. 1–21.

Diamond, D. H. (2016) *A Probabilistic Approach to Blade Tip Timing Data Processing*.

Diamond, D. H., Heyns, P. S. and Oberholster, A. J. (2019) 'Improved Blade Tip Timing measurements during transient conditions using a State Space Model', *Mechanical Systems and Signal Processing*. Elsevier LTD, 122, pp. 555–579.

Dowling, N. E. (2013) *Mechanical Behavior of Materials*, *Mechanical Behavior of Materials*. Pearson.

Elshamy, M., Crosby, W. A. and Elhadary, M. (2018) 'Crack detection of cantilever beam by natural frequency tracking using experimental and finite element analysis', *Alexandria Engineering Journal*. Faculty of Engineering, Alexandria University, 57(4), pp. 3755–3766.

Forbes, G. L. and Randall, R. B. (2013) 'Estimation of turbine blade natural frequencies from casing pressure and vibration measurements', *Mechanical Systems and Signal Processing*. Elsevier, 36(2), pp. 549–561.

Gallego-Garrido, J., Dimitriadis, G., Carrington, I. B. and Wright, J. R. (2007) 'A class of methods for the analysis of blade tip timing data from bladed assemblies undergoing simultaneous resonances - Part II: Experimental validation', *International Journal of Rotating Machinery*, 2007.

Goebel, K. and Saxena, A. (2008) 'Damage Propagation Modeling for Aircraft Engine Run-to-Failure Simulation'.

Gubran, A. (2015) *Vibration Diagnosis of Blades of Rotating Machines*. PhD thesis, University of

Manchester.

Hayes, A. (2019) *Posterior Probability Definition, Investopedia*. Available at: https://www.investopedia.com/terms/p/posterior-probability.asp (Accessed: 1 November 2019).

Hertzberg, R. W., Vinci, R. P. and Hertzberg, J. L. (2012) *Deformation and fracture mechanics of engineering materials*. John Wiley & Sons, Inc.

Hu, Z., Lin, J., Chen, Z. S., Yang, Y. M. and Li, X. J. (2015) 'A non-uniformly under-sampled blade tip-timing signal reconstruction method for blade vibration monitoring', *Sensors (Switzerland)*, 15(2), pp. 2419–2437.

Javed, K., Gouriveau, R., Zemouri, R. and Zerhouni, N. (2012) 'Features selection procedure for prognostics: An approach based on predictability', *IFAC Proceedings Volumes (IFAC-PapersOnline)*, 45(20 PART 1), pp. 25–30.

Jouin, M., Gouriveau, R., Hissel, D., Péra, M. C. and Zerhouni, N. (2016) 'Particle filter-based prognostics: Review, discussion and perspectives', *Mechanical Systems and Signal Processing*, 72, pp. 2–31.

Julier, S. J. and Jeffrey, U. K. (1997) 'A New Extension of the Kalman Filter to Nonlinear Systems', *AeroSense'97. International Society for Optics and Photonics*, pp. 182–193.

Kai Goebel, K., Abhinav Saxena, A., Sankalita Saha, S., Bhaskar Saha, B. and Jose Celaya, J. (2011) 'Prognostic Performance Metrics', pp. 147–178.

Kaloop, M. R. and Hu, J. W. (2015) 'Stayed-Cable Bridge Damage Detection and Localization Based on Accelerometer Health Monitoring Measurements', *Shock and Vibration*, 2015.

Kenton, W. (2018) *Prior Probability, Investopedia*. Available at: https://www.investopedia.com/terms/p/prior_probability.asp (Accessed: 1 November 2019).

Khalkar, V. (2018) 'Paradigm for natural frequency of an un-cracked simply supported beam and its application to single-edged and multi-edged cracked beam', *Vibrations in Physical Systems*, 29(6), pp. 1714–1729.

Le, T. T., Chatelain, F. and Bérenguer, C. (2015) 'Hidden Markov models for diagnostics and prognostics of systems under multiple deterioration modes', *Safety and Reliability: Methodology and Applications - Proceedings of the European Safety and Reliability Conference, ESREL 2014*, pp. 1197–1204.

Lei, Y., Li, Naipeng, Guo, L., Li, Ningbo, Yan, T. and Lin, J. (2018) 'Machinery health prognostics: A systematic review from data acquisition to RUL prediction', *Mechanical Systems and Signal Processing*. Elsevier Ltd, 104, pp. 799–834.

Li, X., Ding, Q. and Sun, J. Q. (2018) 'Remaining useful life estimation in prognostics using deep convolution neural networks', *Reliability Engineering and System Safety*. Elsevier Ltd, 172, pp. 1–11.

Liao, L. and Köttig, F. (2014) 'Review of hybrid prognostics approaches for remaining useful life prediction of engineered systems, and an application to battery life prediction', *IEEE Transactions on Reliability*, 63(1), pp. 191–207.

Meherwan, P. B. (2012) 'Rotor Dynamics', in *Gas Turbine Engineering Handbook (Fourth Edition)*.

Mishra, M. (2016) *Model-based Prognostics for Prediction of Remaining Useful Life*.

Mishra, M. (2018) *Prognostics and Health Management of Engineering Systems for Operation and Maintenance Optimisation*.

Mohamed, M., Bonello, P. and Russhard, P. (2019) 'A novel method for the determination of the change in blade tip timing probe sensing position due to steady movements', *Mechanical Systems and Signal Processing*. Elsevier Ltd, 126, pp. 686–710.

Mrowka-Nowotnik, G., Sieniawski, J. and Nowotnik, A. (2006) 'Tensile properties and fracture toughness of heat treated 6082 alloy', *Journal of Achievements in Materials and Manufacturing Engineering (JAMME)*, 17(1–2), pp. 105–108.

Newman, J. C. and Raju, I. S. (1981) 'An empirical stress-intensity factor equation for the surface crack', *Engineering Fracture Mechanics*, 15(1–2), pp. 185–192.

Orchard, M. E. and Vachtsevanos, G. J. (2007) 'A Particle Filtering-based Framework for Real-time Fault Diagnosis and Failure Prognosis in a Turbine Engine', in *Mediterranean Conference on Control and Automation*.

Raju, J. C. and Newman, I. S. (1984) 'Stress Intensity factor Equations for Cracks in Three-Dimensional bodies Subjected to Tension and Bending Loads', *NASA Technical meomorandum*, (May).

Ramasso, E., Saxena, A., Ramasso, E., Saxena, A., Benchmarking, P. and Meth-, A. P. (2016) 'Performance Benchmarking and Analysis of Prognostic Methods for CMAPSS Datasets . To cite this version : HAL Id : hal-01324587 Performance Benchmarking and Analysis of Prognostic Methods for CMAPSS Datasets'.

Rege, K. and Lemu, H. G. (2017) 'A review of fatigue crack propagation modelling techniques using FEM and XFEM', *IOP Conference Series: Materials Science and Engineering*, 276(1).

Rigosi, G. (2015) *Blade Tip Timing Technique : Theoretical Principles and Simulation of an Experimental Test*. PhD thesis, University of Illinois.

Roemer, M. J. and Kacprzynski, G. J. (2000) 'Advanced diagnostic and prognostic technologies for gas

turbine engine risk assessment', *Proceedings of the ASME Turbo Expo*, 4.

Saha, S., Saha, B., Saxena, A. and Goebel, K. (2010) 'Distributed prognostic health management with Gaussian process regression', *IEEE Aerospace Conference Proceedings*. IEEE, pp. 1–8.

Saidi, L., Ben Ali, J., Benbouzid, M. and Bechhofer, E. (2018) 'An integrated wind turbine failures prognostic approach implementing Kalman smoother with confidence bounds', *Applied Acoustics*, 138(April), pp. 199–208.

Saxena, A., Celaya, J., Balaban, E., Goebel, K., Saha, B., Saha, S. and Schwabacher, M. (2008) 'Metrics for evaluating performance of prognostic techniques', *2008 International Conference on Prognostics and Health Management, PHM 2008*.

Saxena, A. (2010) 'Prognostics Tutorial PHM2010 Conference Slides', in *Annual Conference of the PHM Society (PHM2010)*. Portland, OR.

Sbarufatti, C., Corbetta, M., Manes, A. and Giglio, M. (2002) 'Finite Element based Bayesian Particle Filtering for the estimation of crack damage evolution on metallic panels', *European Conference of Prognostics and Health Management Society PHM.*, pp. 1–10.

Seeger, M. (2004) 'Gaussian processes for machine learning.', *International journal of neural systems*, 14(2), pp. 69–106.

Silva, F. S. (2005) 'The importance of compressive stresses on fatigue crack propagation rate', *International Journal of Fatigue*, 27(10–12), pp. 1441–1452.

Singh, H. (2018) *The Unscented Kalman Filter: Anything EKF can do I can do it better!*, *Towards Data Science*. Available at: https://towardsdatascience.com/the-unscented-kalman-filter-anything-ekf-can-do-i-can-do-it-better-ce7c773cf88d (Accessed: 21 October 2019).

Du Toit, R. G., Diamond, D. H. and Heyns, P. S. (2019) 'A stochastic hybrid blade tip timing approach for the identification and classification of turbomachine blade damage', *Mechanical Systems and Signal Processing*, 121, pp. 389–411.

Uhl, T. (2004) 'The use and challenge of modal analysis in diagnostics', *Diagnostyka*, 30, pp. 151–160.

VanderPlas, J. T. (2018) 'Understanding the Lomb–Scargle Periodogram', *The Astrophysical Journal Supplement Series*. IOP Publishing, 236(1), p. 16.

Wang, W., Hu, W. and Armstrong, N. (2017) 'Fatigue crack prognosis using Bayesian probabilistic modelling', *Mechanical Engineering Journal*, 4(5), pp. 16-00702-16–00702.

Wang, Y., Gogu, C., Binaud, N., Bes, C. and Fu, J. (2019) 'A model-based prognostics method for fatigue crack growth in fuselage panels', *Chinese Journal of Aeronautics*. Chinese Society of

Aeronautics and Astronautics, 32(2), pp. 396–408.

Will, K. (2019) *Overfitting Definition, Investopedia*. Available at: https://en.oxforddictionaries.com/definition/overfitting (Accessed: 29 October 2019).

Witek, L. (2011) 'Crack propagation analysis of mechanically damaged compressor blades subjected to high cycle fatigue', *Engineering Failure Analysis*. Elsevier Ltd, 18(4), pp. 1223–1232.

Witek, L. (2015) 'Simulation of crack growth in the compressor blade subjected to resonant vibration using hybrid method', *Engineering Failure Analysis*. Elsevier Ltd, 49, pp. 57–66.

Worden, K. and Dulieu-Barton, J. M. (2004) 'An Overview of Intelligent Fault Detection in Systems and Structures', *Structural Health Monitoring*, 3(1), pp. 85–98.

Ye, D., Duan, F., Jiang, J., Cheng, Z., Niu, G., Shan, P. and Zhang, J. (2019) 'Synchronous vibration measurements for shrouded blades based on fiber optical sensors with lenses in a steam turbine', *Sensors (Switzerland)*, 19(11).

Zhang, J., He, X. D., Sha, Y. and Du, S. Y. (2010) 'The compressive stress effect on fatigue crack growth under tension-compression loading', *International Journal of Fatigue*. Elsevier Ltd, 32(2), pp. 361–367.

Zhang, J., Duan, F., Niu, G., Jiang, J. and Li, J. (2017) 'A blade tip timing method based on a microwave sensor', *Sensors (Switzerland)*, 17(5), pp. 1–11.

Zhang, J., Duan, F. and Jiang, J. (2017) 'Analysis of a Signal Preprocessing Method for Blade Tip-Timing without the Once-per Revolution Sensor', in *International Conference on Electrical, Automation and Mechanical Engineering (EAME)*, pp. 94–98.

Zhang, W., Li, C., Peng, G., Chen, Y. and Zhang, Z. (2018) 'A deep convolutional neural network with new training methods for bearing fault diagnosis under noisy environment and different working load', *Mechanical Systems and Signal Processing*, 100, pp. 439–453.

Appendix A: Raju-Newman Stress Intensity Factor

The following section only provides the Raju and Newman (1984) equations for determining the stress intensity factor of a surface crack in a rectangular cross-sectional beam subject to tension and bending. The parameters to note is the crack depth (a), the surface crack length ($2c$), the bending stress (S_b), the normal tensile stress (S_t), the thickness (t) and the width of the beam ($2b$)

$$K_1 = (S_t + HS_b)\sqrt{\frac{\pi a}{Q}}F \tag{A.1}$$

The rest of the parameters in equation (A.1) are calculated from equations (A.2) to (A.15)

$$Q = 1 + 1.464\left(\frac{a}{c}\right)^{1.65} \tag{A.2}$$

$$F = \left[M_1 + M_2\left(\frac{a}{t}\right)^2 + M_3\left(\frac{a}{t}\right)^4\right] f_\phi g f_w \tag{A.3}$$

$$M_1 = 1.13 - 0.009\left(\frac{a}{c}\right) \tag{A.4}$$

$$M_2 = -0.54 + \frac{0.89}{0.2 + (a/c)} \tag{A.5}$$

$$M_3 = 0.5 - \frac{1}{0.65 + \left(\frac{a}{c}\right)} + 14\left(1 - \frac{a}{c}\right)^{24} \tag{A.6}$$

$$g = 1 + \left[0.1 + 0.35\left(\frac{a}{t}\right)^2\right](1 - \sin\phi)^2 \tag{A.7}$$

$$f_\phi = \left[\left(\frac{a}{c}\right)^2 \cos^2\phi + \sin^2\phi\right]^{\frac{1}{4}} \tag{A.8}$$

$$f_w = \left[\sec\left(\frac{\pi c}{2b}\sqrt{\frac{a}{t}}\right)\right]^{\frac{1}{2}} \tag{A.9}$$

$$H = H_1 + (H_2 - H_1)\sin^p\phi \tag{A.10}$$

$$p = 0.2 + \frac{a}{c} + 0.6\frac{a}{t} \tag{A.11}$$

$$H_1 = 1 - 0.34\frac{c}{t} - 0.11\frac{a}{c}\left(\frac{a}{t}\right) \tag{A.12}$$

$$H_2 = 1 + G_1\left(\frac{a}{t}\right) + G_2\left(\frac{a}{t}\right)^2 \tag{A.13}$$

$$G_1 = -1.22 - 0.12\frac{a}{c} \tag{A.14}$$

$$G_2 = 0.55 - 1.05\left(\frac{a}{c}\right)^{0.75} + 0.47\left(\frac{a}{c}\right)^{1.5} \tag{A.15}$$

Appendix B: Crack growth estimation graphs

This section reports all the fatigue failure data collected from the experiments. The UKF state space model is applied to the data and the uncertainty of the crack length is shown in blue. The red Gaussian distributions show the uncertainty of the crack length when measuring the natural frequency of the blade from BTT. The green line is the true measured crack length measured from the NDT liquid dye penetrant test. The average assumed stress range is plotted below for the number of cycles during the fatigue test. The stress amplitude is determined from the relative blade tip displacement response due to the acceleration of the slip table

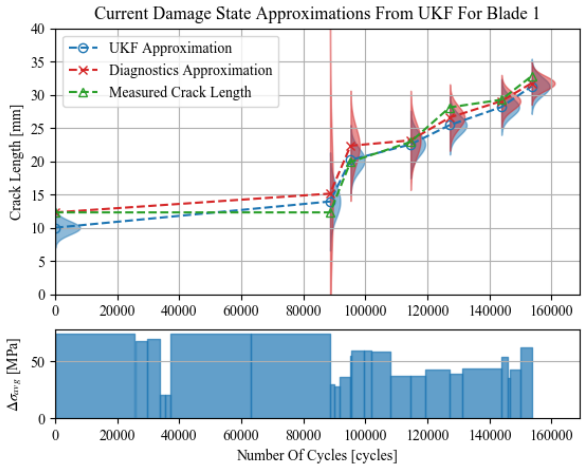

(a)

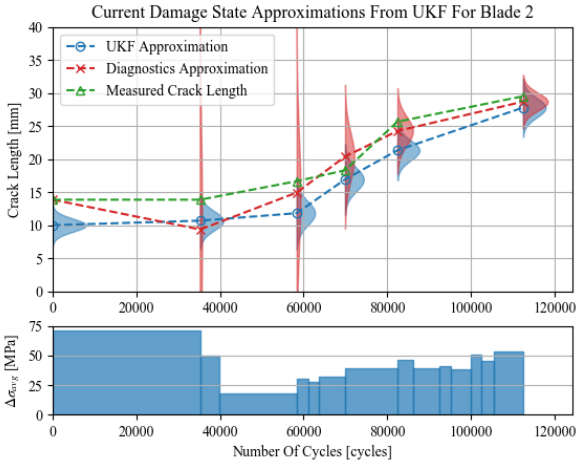

(b)

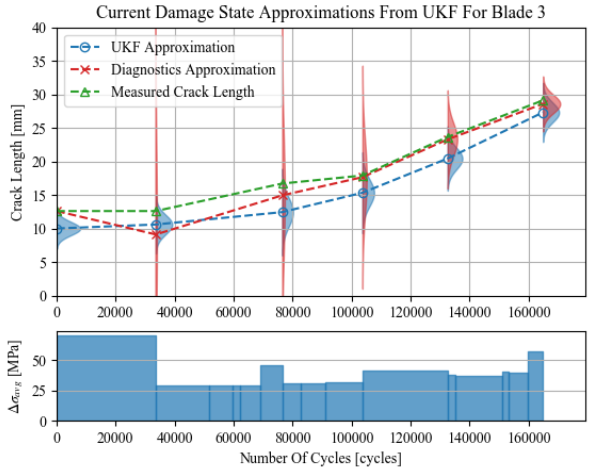

(c)

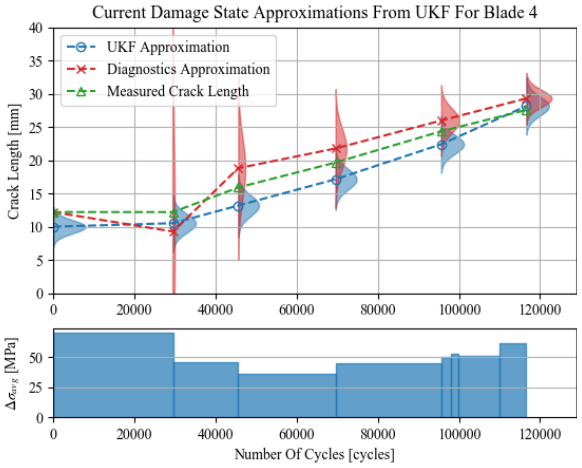

(d)

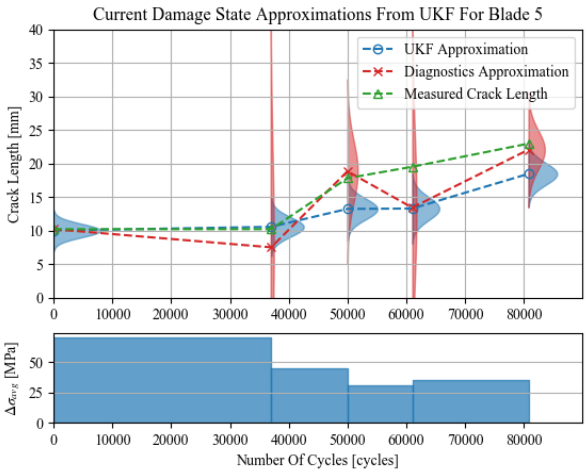

(e)

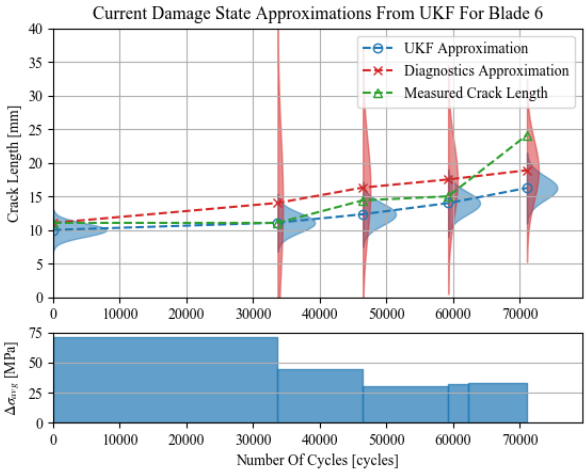

(f)

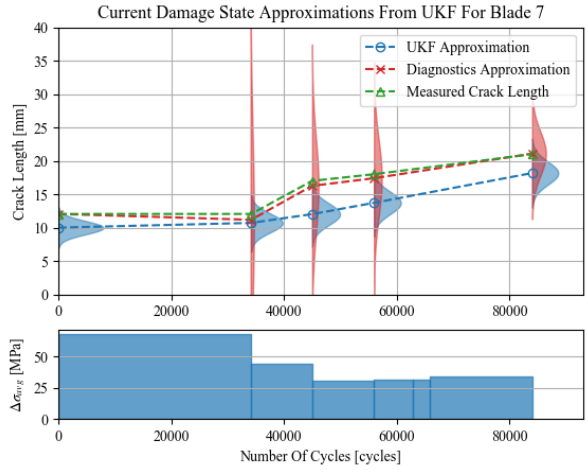

(g)

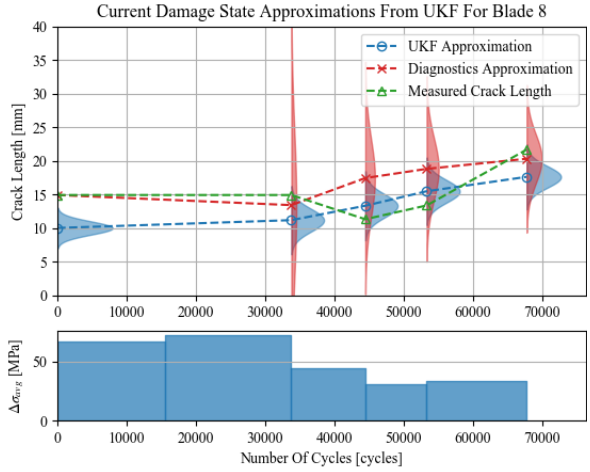

(h)

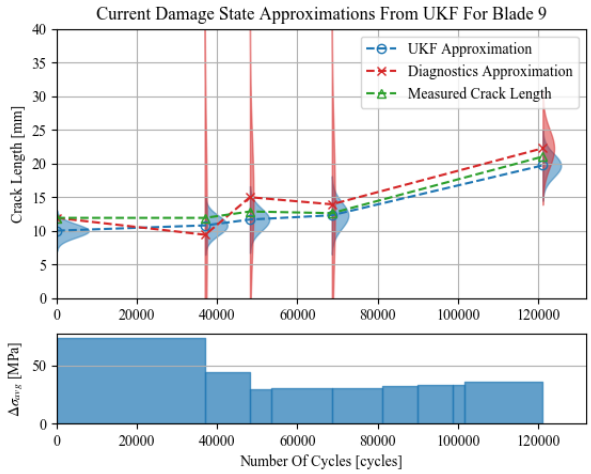

(i)

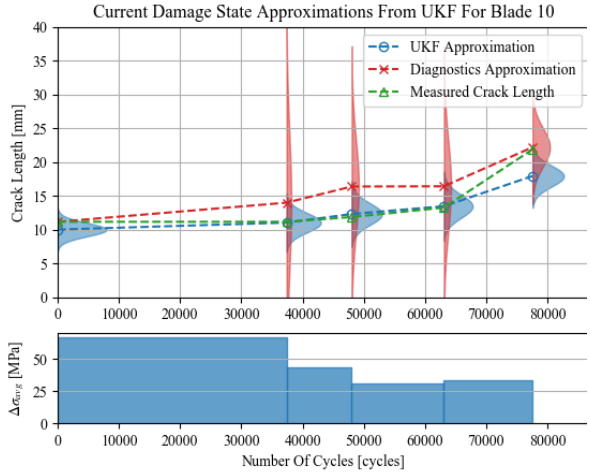

(j)

Figure B.1: All experimental results with UKF approximations of the current crack length (blue) and the diagnostics of the

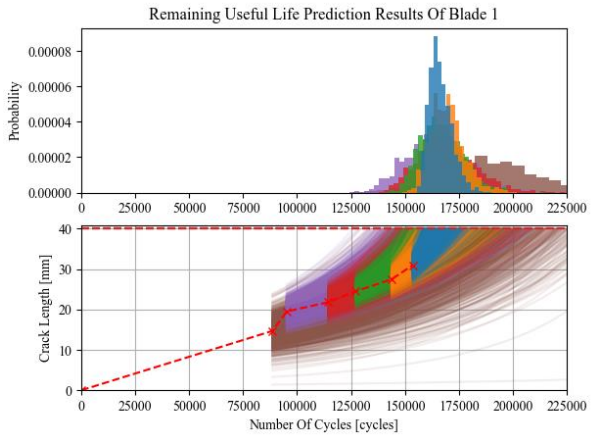

(a)

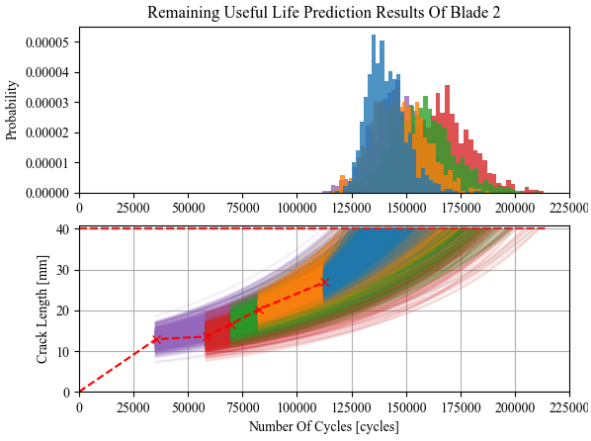

(b)

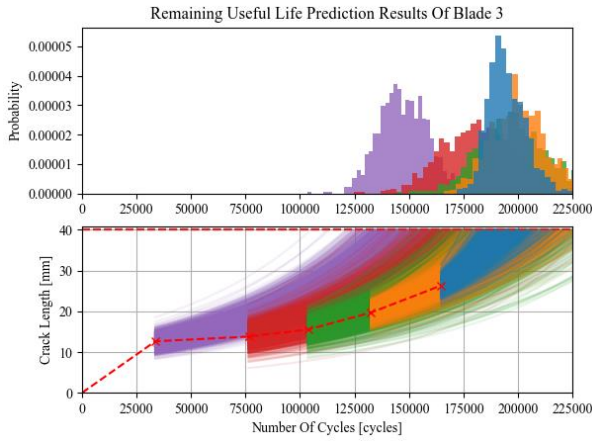

(c)

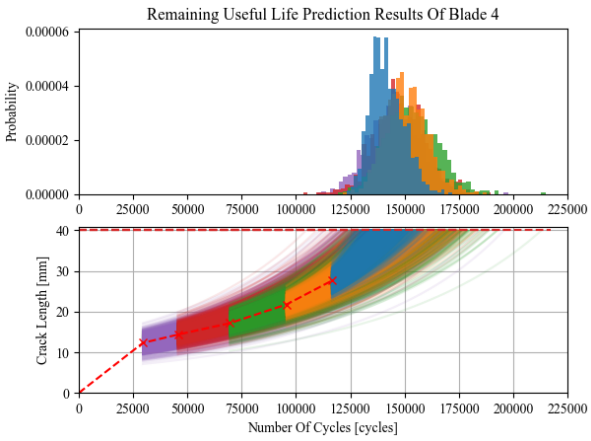

(d)

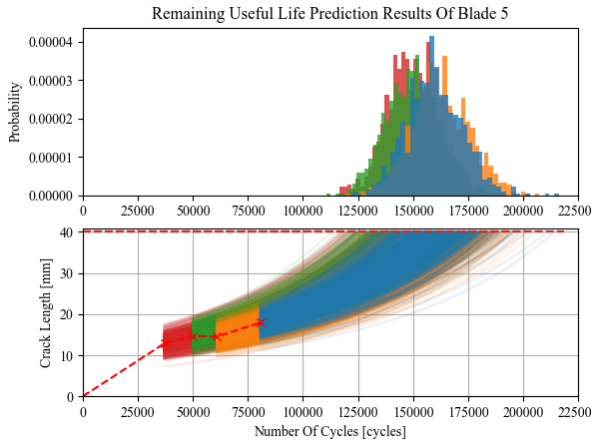

(e)

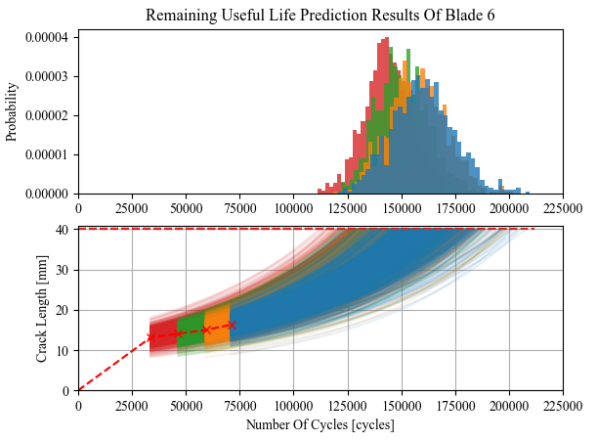

(f)

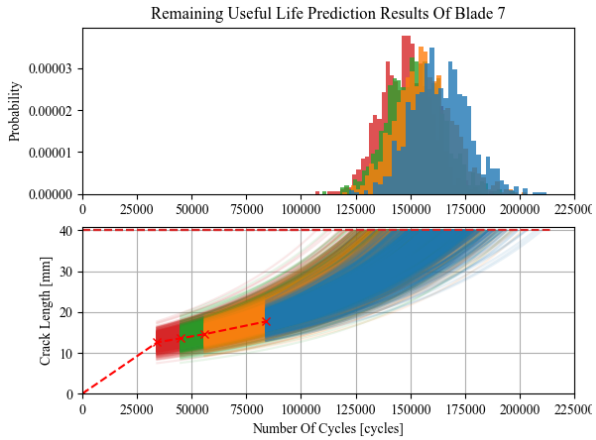

(g)

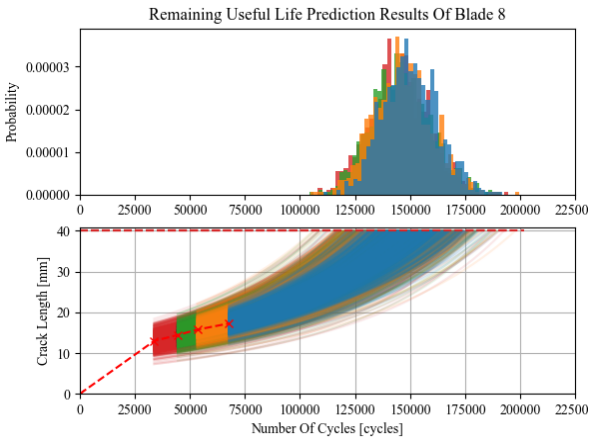

(h)

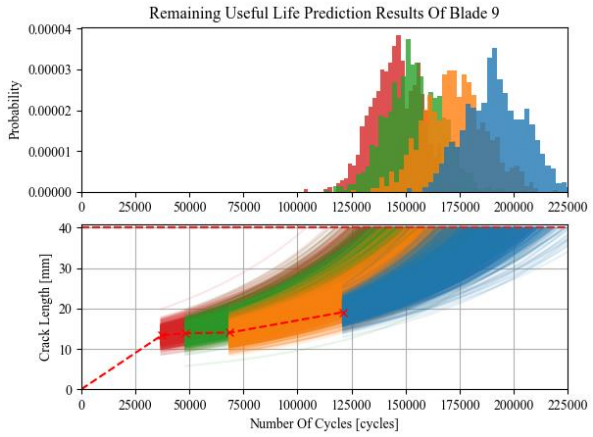

(i)

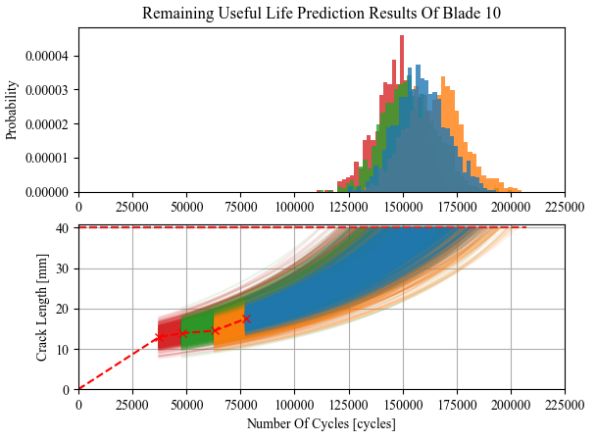

(j)

Figure B.2: All remaining useful life estimates of the BTT signal for ten blades